

Development of ceramic colloid using pulsed laser ablation in liquid for application in thermal management coatings for grinding operations

By:

Saeid Heidarinassab, BSc. MSc

Under the supervision of:

Prof Dermot Brabazon

Co-supervised by:

Dr Inam.Ul Ahad

A thesis submitted to Dublin City University for consideration for the degree of:

Doctor of Philosophy (PhD)

School of Mechanical and Manufacturing Engineering

Dublin City University

June 2026

Declaration

I hereby certify that this material, which I now submit for assessment on the programme of study leading to the award of Doctor of Philosophy is entirely my own work, and that I have exercised reasonable care to ensure that the work is original and have conformed to the regulations on the use and declaration of Generative AI, and does not to the best of my knowledge breach any law of copyright, and has not been taken from the work of others save and to the extent that such work has been cited and acknowledged within the text of my work. I hereby certify that no Generative Artificial Intelligence (Gen AI) tools have been used in the creation of the thesis.

Signed:  ID No.: 22270205 Date: 11/06/2026

Dedication

I dedicate this thesis to my beloved family, Alireza and Sara, whose unwavering love, support, and encouragement have been a constant source of strength throughout this journey. Their belief in me has carried me through every challenge and achievement along the way.

I would also like to express my deepest gratitude to my dear sister, Sahar, whose continuous encouragement and confidence in my abilities have played a significant role in keeping me motivated and focused on my goals.

Finally, and most importantly, I dedicate this work to my beloved Negar. Her love, patience, and steadfast support have been invaluable throughout the most demanding moments of this journey. Her presence, encouragement, and unwavering faith in me provided the strength and positivity I needed to persevere through difficult times. This achievement would not have been possible without her by my side.

List of Publications

First author:

Fabrication of Silicon Carbide Nanoparticles Using Pulsed Laser Ablation in Liquid and Viscosity Optimisation via Solvent Tuning. **https://doi.org/10.3390/ma17184527**

Investigation of Ablation Efficiency and Properties of Silicon Carbide Nanoparticles Synthesised Using Pulsed Laser Ablation in Liquid. 10.1016/j.optlaseng.2024.108341

Thermal Conductivity Enhancement of Epoxy Abrasive Composites Using Hybrid SiC–Al_2O_3 Fillers via Experimental, Analytical, and FEA Approaches. https://doi.org/10.1016/j.jmrt.2026.07.262

Co-author:

A review of physical, chemical and biological synthesis methods of bimetallic nanoparticles and applications in sensing, water treatment, biomedicine, catalysis and hydrogen storage. https://doi.org/10.1016/j.cis.2023.103010

Screen-printed electrodes on paper using copper nano- and micro-particles. https://doi.org/10.1016/j.jmrt.2024.03.016

A review of carbon and aluminium nanofluids and elastocaloric materials for heating and cooling applications. https://doi.org/10.1016/j.ijft.2025.101163

Electronic structure and charge transport mechanisms at ZnO/$CoPcF_x$ interfaces: synergistic effects of ZnO defects and phthalocyanine fluorination. 10.1016/j.apsusc.2026.167344

List of Presentations

Poster presentation: investigation of Silicon Carbide materials used in high temperature applications, University of Sheffield, UK, July 2023

Oral Presentation: Thermal Conductivity enhancement of abrasive material using nano SiC particles, AMPT2023, September 2023, Kuala Lumpur, Malaysia

Poster Presentation: The application of Nanoparticles at high temperature Industries, UCD, Dublin, Ireland, October 2023

Poster Presentation: Abrasive Discs product performance enhancement through Nanoparticle technology, I-Form Gathering, Athlone, Ireland, December 2023

Oral Presentation; Investigation of ablation efficiency and properties of silicon carbide nanoparticles synthesised using PLAL, University of Manchester, UK, July 2024.

Oral Presentation; Advances in materials and processing technologies, AMPT2024, Istanbul, Turkey, September 2024

Poster Presentation; Fabrication of silicon carbide nanoparticles using PLAL and viscosity optimisation using solvent tuning, I-Form Gathering, Athlone, Ireland, December 2024

Oral Presentation: Thermal Conductivity measurement of ceramic fillers incorporated into epoxy matrices using SiC and Al2O3 particles, Dublin City University, Dublin, Ireland, July 2025

Contents

1 Chapter 1: Introduction 3

1.1 Aims and Objectives 5

1.1.1 Aims 5

1.1.2 Objectives 6

2 Chapter 2: Literature Survey 6

2.1 Abrasives 8

2.2 Silicon Carbide Reinforced Material 8

2.3 Synthesis methods of SiC NPs 11

2.3.1 High Energy Ball-Milling 12

2.3.2 Mechanical Alloying 14

2.3.3 Chemical Etching 14

2.3.4 Combustion Synthesis 15

2.3.5 Carbothermic reduction 16

2.3.6 Sol-gel 17

2.3.7 Pulsed Laser Ablation in Liquid 19

2.3.8 Chemical Vapor Synthesis 21

2.4 Properties of SiC NPs 22
2.4.1 Surface Properties 22
2.4.2 Thermal Properties 24
2.4.3 Electrical Properties 25
2.4.4 Biocompatibility Properties 26
2.5 Application 27
2.5.1 Composites 27
2.6 Summary 28
2.7 Aluminium Oxide Nanoparticles Reinforced Material 30
2.8 Synthesis Methods of Al_2O_3 Nanoparticles 34
2.8.1 High-Energy Ball Milling 37
2.8.2 Pulsed Laser Ablation in Liquid (PLAL) 38
2.8.3 Sol-Gel Method 40
2.9 Summary 42
3 Chapter 3: Fabrication of Silicon Carbide Nanoparticles Using Pulsed Laser Ablation in Liquid and Viscosity Optimization via Solvent Tuning 45
Keywords 46
3.1 Introduction 47

3.2 Experimental 49

3.2.1 NPs Synthesis 49

3.2.2 NPs Characterisation 50

3.3 Results and Discussion 51

3.3.1 Visual inspection and Ultraviolet-visible spectroscopy 51

3.3.2 Dynamic Light Scattering (DLS) 54

3.3.3 Field emission scanning electron microscopy (FESEM) and scanning transmission electron microscopy (STEM) 61

3.3.4 Viscosity Optimization 62

3.4 Conclusion 64

4 Chapter 4:Ablation efficiency and properties of SiC NPs synthesised via PLAL 66

4.1 Introduction 68

4.2 Experimental and Design of Experiment 70

4.2.1 NPs synthesis 71

4.2.2 NPs characterisation 73

4.2.3 Statistical analysis 74

4.3 Results and Discussion 75

4.3.1 Optimisation of the PLAL for high-yield SiC NPs fabrication 75

4.3.2 77

4.3.3 Effect of ablation time on the properties of resulting NPs 77

4.3.4 Effect of scanning speed on the resulting NPs 85

4.3.5 Effect of laser fluence on the properties of resulting NPs 93

4.4 Conclusion 101

5 Chapter 5: Thermal Conductivity Enhancement of Epoxy Abrasive Composites Using Hybrid SiC–Al_2O_3 Fillers: Experimental, Analytical, and FEA Approaches 103

5.1 Introduction 105

5.2 Materials and Methods 107

5.2.1 Materials 107

5.2.2 Preparation of Epoxy–Particle Composites Coated Substrate 107

5.3 Materials Characterisation 109

5.3.1 Thermal conductivity 109

5.3.2 SEM Imaging 110

5.3.3 Grinding disk test setup 110

5.4 Analytical model of the prepared grinding disk thermal conductivity 111

5.5 Finite Element Analysis (FEA) setup 117

5.5.1 Geometry and Boundary Conditions 117

5.5.2 Meshing Strategy and Simulation Cases 118

5.5.3 Material Properties 119

5.6 Results and discussion 121

5.6.1 Calculating the thermal conductivity using experimental data 122

5.6.2 Calculating the thermal conductivity using Analytical and FEA models 132

5.7 Conclusion 139

6 Chapter 6:Conclusion 143

7 Appendices 148

8 References 154

List of figures

Figure 2.1Phase diagram of silicon carbide[56] 9

Figure 2.2 Stacking sequences of double-layers of 3C-, 4H-, 6H- and 15R–SiC[29] 10

Figure 2.3 Schematic diagram of pulsed laser ablation in liquid to synthesize SiC NPs; b) TEM image of product SiC NPs via pulsed laser ablation in liquid method; c) Single β-SiC NPs for which an improvement of the compact planes imaging by Fast Fourier Transform treatment was performed [2]. 18

Figure 2.4 Applications for SiC NPs [3]. 23

Figure 2.5 Crystalline systems and network parameters of Al2O3[105] 28

Figure 3.1Photographs of a) DI water with SiC target before PLAL, b) after 5 min PLA; and set of samples produced at a constant PRR of 50 kHz, and scanning speed 1, 2, 3 m/s from left to right respectively for laser powers of c) 60%, d) 80%, and e) 100%. 41
Figure 3.2 UV-Vis for the samples prepared at constant laser power percentages of a) 60, b) 80, and c)100, for the various scanning speeds and PRR. 42
Figure 3.3 Dynamic Light Scattering results for the samples prepared at constant laser power percentages of a) 60, b) 80, and c)100, for the various scanning speeds and PRR. 44
Figure 3.4 The change in NPs sizes with a) changing scanning speed at a constant PRR of 10, b) PRR in a constant scanning speed of 2 m/s, and c) laser power percentage in a constant scanning speed and PRR of 2 m/s and 10 kHz..... 45
Figure 3.5 Dynamic Light Scattering patterns in the size range up to 450 nm for a set of samples laser power percentages of a) 60, b) 80, and c) 100. 46
Figure 3.6 The NPs concentration measurements as a function of various laser parameters a) scanning speeds, b) PRR, and c) laser power percentages. 47
Figure 3.7 FESEM images of produced SiC NPs - a & b & d) SE acceleration voltage 1 kV, e & c) SE acceleration voltage 15 kV, and f) bright field STEM acceleration voltage 10 kV..... 48
Figure 3.8 Dynamic viscosity measurements at 25 ◦C as function of volumetric concentration of a) Acetone, b) IPA and c) Glycerol. 50
Figure 4.1Response-surface graphs show the outcome of the ablation time, scanning speed, and laser fluence on the yield of SiC NPs in DI water. Response surface plot of SiC NP productivity as a function of a) scanning speed, b) laser fluence, c) ablation time and d) predicted vs actual graph 56

Figure 4.2 UV-Vis spectra for the samples S1, S2, and S3 in a constant laser fluence of 3.78 J/cm2, scanning speed of 0.1 m/s and ablation time of 5, 10, and 15 minutes respectively; the inset image shows the visual inspection of the corresponding samples 59
Figure 4.3 EDX keV response, SEM image of NP, and colour maps of the measured Si, O, and C concentrations for the sample S3 60
Figure 4.4 XRD patterns of the target material and produced NPs 61
Figure 4.5 Micrographs FESEM, BF-STEM and size distribution of a, b, and c of the sample S1. d, e, and f for the sample S2, and g, h, and k for the sample S3..... 61
Figure 4.6 Actual ablated mass [mg] for a constant laser fluence of 3.78 J/cm2, a scanning speed of 0.1 m/s, and ablation times of 5, 10, and 15 minutes 62
Figure 4.7 DLS results for the samples S1, S2, and S3 in a constant laser fluence of 3.78 J/cm2, scanning speed of 0.1 m/s and ablation times of 5, 10, and 15 minutes, respectively..... 62
Figure 4.8 Zeta potential measurement of the samples S1, S2, S3. 63
Figure 4.9 UV-Vis spectra for the samples S3, S6, and S9 in a constant laser fluence of 3.78 J/cm2, ablation time of 15 minutes and scanning speed of 0.1, 0.3, and 0.5 m/s respectively, inset image shows the visual inspection of the corresponding samples 65
Figure 4.10 DLS results for the samples S3, S6, and S9 in a constant laser fluence of 3.78 J/cm2, ablation time of 15 minutes, and scanning speed of 0.1, 0.3, and 0.5 m/s, respectively. 67
Figure 4.11 Micrographs FESEM, BF-STEM and size distribution of a, b, and c of the sample S3. d, e, and f for the sample S6, and g,h, and k for the sample S9. 67
Figure 4.12 Actual ablated mass [mg] in a constant laser fluence 3.78 J/cm2ablation time of 15 minutes, and scanning speed of 0.1, 0.3, and 0.5 m/s. 68
Figure 4.13 Zeta potential measurement of the samples S3, S6, and S9 68

Figure 4.14 UV-Vis spectra for the samples S6, S15, and S24 in a constant scanning speed of 0.3 m/s, ablation time of 15 minutes and laser fluences of 3.78, 6.5, and 7.5 J/cm2 respectively, inset image shows a picture of the corresponding samples..... 70
Figure 4.15 DLS results for the samples S6, S15, and S24 in a constant scanning speed of 0.3 m/s, ablation time of 15 minutes, and laser fluences of 3.78, 6.5, and 7.5 J/cm2 respectively..... 71
Figure 4.16 Micrographs FESEM, BF-STEM and size distribution of a, b, and c of the sample S6. d, e, and f for the sample S15, and g,h, and k for the sample S24. 71
Figure 4.17 Actual ablated mass [mg] in a constant ablation time of 15 minutes and scanning speed of 0.3 m/s and laser fluences of 3.78, 6.5, and 7.5 J/cm2..... 72
Figure 4.18 Zeta potential measurement of the samples S6, S15, and S24..... 73
Figure 4.19 Optical band gap estimation using the Tauc plot method..... 73
Figure 5.1 a) the meshing convergence of the model, b) schematic representation of the meshing sample, and c) schematic illustration of the three layers being modelled. 80
Figure 5.2 Thermal conductivity measurement of the SiC and Al_2O_3 5 wt% in various particle sizes. b) IR camera normalised temperature vs time for various sizes of Al_2O_3, c) IR camera normalised temperature vs time for various sizes of SiC, and d) material removal for SiC and Al2O3 in different particle sizes..... 88
Figure 5.3 . SEM images of 185µm Al_2O_3 particles at 45w% into epoxy resin a) wider surface, and b) high magnification of the pointed area 88
Figure 5.4 SEM images of 185µm SiC particles at 45w% into epoxy resin a) wider surface, and b) high magnification of the pointed area..... 89
Figure 5.5 Powder flowability test result for a) Aluminium oxide and b) silicon carbide in different particle sizes..... 89

Figure 5.6 Thermal conductivity as a function of particle loading for a) Al_2O_3 and b) SiC and IR-camera normalised temperature recording for c)Al_2O_3 4.5 Micron at different particle loadings, and d)SiC 4.5 Micron at different particle loadings 91
Figure 5.7 SEM images of different particle loading alongside the surface of the deposited coating of a, b) Al_2O_3 5%, Al_2O_3 45%, c, d)SiC 5%, SiC 45% and e, f) 100 nm SiC 5%, SiC 45%. 92
Figure 5.8 SEM images of the sample prepared by the mixing ratio of 9:1 for a) SiC:Al_2O_3 , b) higher magnification, and c) related thermal conductivity measurement for the various mixing ratios, and d) Normalised IR-camera temperature recording..... 93
Figure 5.9 a comparison between different approaches for thermal conductivity measurements with different particle loadings, where a) Aluminium oxide particle size 185, b) Silicon carbide particle size 185, c) Aluminium oxide particle size 4.5, and d) Silicon carbide particle size 4.5 µm 97

List of Tables

Table 2.1 Synthesis methods of SiC NPs..... 9
2.2 . Summary of synthesis techniques used for synthesising Al2O3 and their relative information..... 29
Table 3.1Design of experiments used for production of sample colloids..... 39
Table 3.2 Viscosity of the colloids using a 0.8 volumetric fraction of acetone, IPA and glycerol. 49
Table 4.1 Design of Experiment for all the samples and their assigned sample names 53
Table 4.2 ANOVA analysis for a quadratic fit of the data 56

Table 4.3 The NPs mean size at the three different laser ablation times 60

Table 4.4 DLS and STEM size measurements of the NPs for samples S3, S6, and S9. 66

Table 4.5 DLS and STEM size measurements of the NPs for samples S6, S15, and S24. 70

Table 5.1 Particle mean size and loading for SiC and Al_2O_3 particles used in the fabrication of tested samples 77

Table 5.2The mixing ratio of the SiC and Al_2O_3 particles used for fabrication of tested samples. 78

Table 5.3 Thickness of the layers used in the FEA analysis..... 80

Table 5.4 Analytical calculation of the thermal conductivity for different sample size, loading and ratio 94

Table 5.5 Thermal Conductivity measurement of the composite material using FEA..... 96

Table 5.6 Conclusion of the results in three different aspects including thermal conductivity, temperature response, and integrated conclusion. 98

Abstract

Silicon carbide (SiC) is a technologically important ceramic material prized for its high thermal conductivity, wide bandgap, chemical inertness, and excellent high-temperature stability, properties that make it attractive for applications ranging from printed electronics and biomedical imaging to thermally stable abrasive and composite systems. This thesis investigates the synthesis, characterisation, and functional application of SiC nanoparticles (NPs) and SiC-based composites, addressing gaps in the understanding of how processing parameters govern nanoparticle properties and how these particles can subsequently be exploited to enhance the thermal performance of macroscale composite materials.

The first phase of this work focused on the fabrication of SiC NPs via pulsed laser ablation in liquid (PLAL), a green, single-step, top-down synthesis route. A systematic investigation of laser fluence, scanning speed, pulse repetition rate, and ablation time was carried out to determine their influence on ablation efficiency and the resulting nanoparticle characteristics. Optimised processing conditions (15 min ablation time, 0.5 m/s scanning speed, 7.5 J/cm^2 fluence) yielded a maximum mass productivity of 1.196 mg·h^{-1}W^{-1}, with X-ray diffraction confirming the crystalline 3C-SiC phase and a direct correlation established between ablated mass and colloidal concentration, while increasing particle size was linked to a reduction in optical band gap. Building on this, the colloidal properties of the synthesised NPs were further tailored for inkjet-printing applications: nanoparticle size (89–155 nm), concentration, and morphology were shown to depend on laser power, scanning speed, and pulse repetition rate, while post-synthesis viscosity modulation using acetone, isopropyl alcohol, and glycerol enabled colloid viscosities compatible with commercial inkjet printheads (up to 10.95 mPa·s).

The second phase of the thesis translated these ceramic-particle insights to a macroscale engineering application, investigating the thermal conductivity of epoxy-matrix abrasive composites reinforced with SiC and aluminium oxide (Al_2O_3) particles. Using thermal conductivity measurements, infrared thermal imaging, SEM, analytical modelling, and finite element analysis, the effects of particle type, size, loading, and hybrid filler ratio on heat

transfer were systematically evaluated. Hybrid SiC–Al_2O_3 composites outperformed Al_2O_3-only systems, with SiC-rich hybrids (9:1 SiC:Al_2O_3) achieving a maximum thermal conductivity of ~2.78 W/mK, attributed to enhanced phonon transport, stronger covalent bonding, and improved particle dispersion relative to Al_2O_3. Larger particle sizes and higher filler loadings further improved conductivity, whereas nano-sized fillers exhibited reduced performance at high loadings due to agglomeration and interfacial thermal resistance. Improved thermal conductivity correlated with greater thermal stability and extended operational lifetime under grinding conditions, with analytical and FEA models capturing the dominant experimental trends.

Collectively, this thesis demonstrates a coherent pathway from laser-based nanoparticle synthesis and property optimisation to the practical deployment of ceramic fillers in thermally engineered composite materials, providing process-informed design principles for SiC-based nanomaterials and hybrid ceramic-reinforced composites for high-performance, thermally demanding industrial applications.

1 Chapter 1

Introduction

Pulsed laser ablation in liquid (PLAL) is a method of synthesising nanoparticles (NPs), which involves a laser irradiation of a target that is submerged in a liquid medium to produce NPs based on the material of the target[1]. There has been increasing interest in the implementation of PLAL in recent years to generate colloids for various applications. The PLAL process is operated within a relatively straightforward system which is kept at room temperature[2]. The technique has been used for synthesising different metallic NPs including magnesium[3], [4], carbon[5], gold[6], silver[7], silicon[8] and ceramic NPs including silicon carbide[9], titanium oxide[10], silver oxide[11]. PLAL has variety of advantages over other NPs production methods due to the low cost of equipment for atmospheric ablation, the simplicity of the method which does not require a special environment such as vacuum, and the ability to alter the properties and morphology of the NPs by changing the laser parameters and liquid media[12], [13]. Parameters in PLAL include laser fluence, pulse repetition rate (PRR), scanning speed, ablation time, and liquid media. These affect the physical or chemical properties of produced NPs. Moreover, Silicon carbide SiC is promising wide band gap semiconducting material which exhibits superior and attractive properties such as high breakdown field strength, high chemical stability, high thermal conductivity, outstanding resistance to oxidation and corrosion, and extreme hardness. SiC NPs have been used widely in various applications that require high temperature and high frequency such as light emitting diodes and UV detectors. In addition, SiC has excellent high-temperature properties such as oxidation resistance, high thermal conductivity, low thermal expansion coefficient, so that it can be used as raw material for advanced refractories, functional ceramics, and abrasives[14], [15]. There are several ways to produce the SiC NPs, where PLAL has significantly emerged in the past years due to its benefits rather than other methods. For instance, Castelleto and coworkers[16] fabricated 4H-SiC NPs using ultra-short pulsed laser ablation for biomedical imaging applications, whereas Yamada et al.[17] studied the resulting sizes, shapes and crystal structure of produced SiC NPs using PLAL. Few data have been reported on the laser ablation of SiC NPs, which requires further investigation to understand the correlation of the PLAL parameters and SiC NPs properties[18], [19], [20]. Applications of oxide NPs in thermal insulation materials can be limited by their low thermal reliabilities at high temperature, however SiC NPs are considered as thermal insulation materials due to the good corrosion resistance of SiC in

high temperatures, which can retain its initial morphology even at a temperature as high as 1800 °C, and also the superior high-temperature phase reliability up to 2000 °C without phase transformation. Hence, it can be used for heat isolation applications where the thermal conductivity properties are crucial for the life time of the tools including for discs or solutions for grinding or polishing applications. Normally, these discs have a backing material on which the abrasive particles are placed and bonded using an adhesive. These backing materials are commonly based on cottons or polymers where the grit size of the particles on the grinding discs are printed on them using an ink-jet printing process. However, it has not been reported before that the printed layer is used as a heat isolation layer. In this work SiC particles within a colloid were produced via PLAL and investigated as a potential thermal barrier for the backing material of grinding disks to provide improved lifetime and robustness, as well as for use as a grinding or polishing medium to enhance the efficacy of finish grinding operations. In this study, the influence of the PLAL parameters on the produced SiC NPs were also investigated

1.1 Aims and Objectives

1.1.1 Aims

The aim of this study was to establish a coherent, process-informed pathway from the laser-based synthesis of silicon carbide (SiC) nanoparticles to their functional application as thermally conductive fillers in ceramic-reinforced epoxy composites for abrasive disc backing materials. This required first developing a mechanistic understanding of how pulsed laser ablation in liquid (PLAL) processing parameters govern nanoparticle formation and properties, and then translating this understanding into the design of hybrid SiC–Al_2O_3 filled composites capable of improving the thermal management, stability, and operational lifetime of abrasive discs

1.1.2 Objectives

To achieve this aim, the thesis pursued the following specific objectives:

1. To systematically investigate the influence of PLAL processing parameters — laser fluence, scanning speed, pulse repetition rate, and ablation time — on the ablation efficiency, yield, size distribution, crystal structure, and optical properties of SiC nanoparticles, and to identify optimised processing conditions for maximising nanoparticle productivity.

2. To characterise the synthesised SiC nanoparticles and their colloids using XRD, EDX, FESEM/STEM, DLS, UV-Vis spectroscopy, and FTIR, and to tailor colloidal viscosity through post-synthesis solvent modulation (acetone, isopropyl alcohol, glycerol) to meet the rheological requirements of inkjet-printing applications.

3. To apply a statistical design-of-experiments approach to the PLAL process in batch mode, in order to improve process scalability and support consistent, reproducible nanoparticle production.

4. To evaluate the effect of particle type (SiC vs. Al_2O_3), particle size, filler loading, and hybrid SiC:Al_2O_3 ratio on the thermal conductivity of epoxy-matrix composites, using thermal conductivity measurement, infrared thermal imaging, and SEM-based microstructural analysis.

5. To develop and validate analytical (Maxwell-Eucken) and finite element analysis (FEA) models of composite thermal conductivity against experimental data, and to relate the resulting thermal performance improvements to the thermal stability and expected operational lifetime of abrasive discs under grinding conditions.

2 Chapter 2

Literature

Survey

2.1 Abrasives

Abrasive discs are frequently employed in metalworking workshops for cutting slabs and rods. These tools also are used for polishing, surface finishing, and grinding the materials[21].These tools are versatile, allowing for cutting, shaping, deburring, preparing welding blanks, and polishing surfaces. For professionals like machinists and technicians, the cost and lifespan of these discs are crucial factors in daily operations. The most influential variables affecting their performance are (a) the type and size of the abrasive and (b) the binder used in the disc. There are two main types of abrasive discs for manual machines: (a) those with a metal body that use diamond abrasives, typically for cutting masonry, marble, and ceramics, and
(b) those that use aluminium oxide (Al2O3) or silicon carbide (Si3N4) as abrasive materials, primarily for cutting metals[22]. Abrasive discs are commonly based on a grinder material and a backing material which are bonded together by a glue. This glue could be any polymeric material including Nylon 6, Nylon 66 or other materials. In addition, paper, cloth, plastic films, vulcanised fibre, foam or a combination of paper and cloth are used as backing for coated abrasives. The backing gives the abrasive very specific grip and adhesion, stretch, tear resistance, tensile strength, flexibility and stability properties. These materials are not thermally conductive and due to high heat dissipation in the backing material, there is high possibility of degradation and failure of the disc. On the other hand, , ceramic composite materials have been used widely for different applications, including biomedical[23], [24], aerospace[25], military[26], automotive[27], and high-temperature industries[28]. Utilising reinforced materials in the backing disc and enhancing the thermal conductivity of the backing material through the use of reinforced composites represent innovative approaches to mitigating failure and extending the lifespan of the disc. This strategy introduces a novel backing material solution.

2.2 Silicon Carbide Reinforced Material

Silicon carbide (SiC) is a IV–IV compound material with unique physical and chemical properties. The strong

chemical bonding between Si and C atoms gives this material very high hardness, chemical inertness, and high thermal conductivity. As a semiconductor, SiC exhibits a wide bandgap, high critical electric field strength, and high saturation drift velocity.

Both n- and p-type control across a wide doping range is relatively easy in SiC; this makes SiC exceptional among wide bandgap semiconductors. The ability of SiC to form silicon dioxide (SiO2) as a native oxide is an important advantage for device fabrication. Because of these properties, SiC is a promising semiconductor for high-power and high-temperature electronics; subsequent chapters will describe in detail the fundamentals of SiC technologies, its properties, growth, characterisation, device fabrication, and device characteristics. The physical and chemical stability of SiC, however, has made crystal growth of SiC extremely difficult, and severely hampered development of SiC semiconductor devices and their electronic applications. The existence of various SiC structures with different stacking sequences (otherwise known as polytypism) has also hampered growth of electronic-grade SiC crystals. Reinforced materials employed within a ceramic polymer matrix can be categorised based on various attributes. The incorporation of ceramic materials into the matrix is influenced by factors such as particle size, shape, and manufacturing method. For example, research indicates that the thermal conductivity of a ceramic polymer matrix, when reinforced with silicon carbide, tends to increase with larger particle sizes. Furthermore, the shape of the particles significantly impacts the thermal conductivity of the matrix; spherical particles have demonstrated superior thermal conductivity compared to non-spherical counterparts. Since its successful synthesis by Shuaib et al.[29], the investigation into silicon carbide (SiC) has continued unabated. As a ceramic material, SiC inherits the exceptional characteristics of structural ceramics, including corrosion resistance, wear resistance, high strength, and hardness[14]. Furthermore, SiC exhibits outstanding high-temperature properties such as oxidation resistance, high thermal conductivity, and a low thermal expansion coefficient, making it an ideal material for advanced refractories, functional ceramics, and abrasives. In recent years, with the growth of the electronics industry, SiC has gained increasing prominence due to its wide bandgap. With its impressive attributes such as high critical breakdown voltage and carrier saturation drift velocity, SiC emerges as a promising third-generation semiconductor material, particularly in high-frequency

semiconductor devices.SiC is a representative covalent compound. According to the C–Si phase diagram presented by Olesinski et al.[30] (Fig. 2.1), there is no solid solution between silicon (Si) and carbon (C), and the atomic ratio of Si to C in SiC is 1:1. Both Si and C atoms are tetravalent, with four valence electrons in their outermost shell. They undergo sp3 hybridisation, sharing an sp3 hybrid orbital to form a covalent tetrahedral structure. Each Si atom is surrounded by four adjacent C atoms, and conversely, each C atom is surrounded by four Si atoms. The bond energy between Si and C is notably high, approximately 4.6 eV[31], imparting exceptional properties to SiC, such as remarkable chemical stability, excellent heat resistance, high strength, low thermal expansion coefficient, and a wide band gap. From a crystallographic perspective, SiC exhibits a prototypical polymorphic structure[32]. Its crystal structure comprises a double-layered arrangement of densely packed Si and C atoms. The diatomic C–Si layer manifests various crystal types based on different stacking sequences within a given period[33], [34]. To date, approximately 250 crystal types of SiC have been identified, yet only a select few have undergone detailed investigation[35]. In 1947, Ramsdell systematically classified the various SiC types. Each SiC type was denoted as nX, where X represents a Bravais lattice, encompassing cubic (C), hexagonal (H), and rhombic (R) structures. The ”n” signifies the number of diatomic layers present in a single period within this lattice arrangement. Among the identified structures, cubic 3C, hexagonal 4H and 6H, as well asRhombohedral R configurations are the most prevalent in SiC. Notably, SiC possesses only one cubic type, referred to as β-SiC.

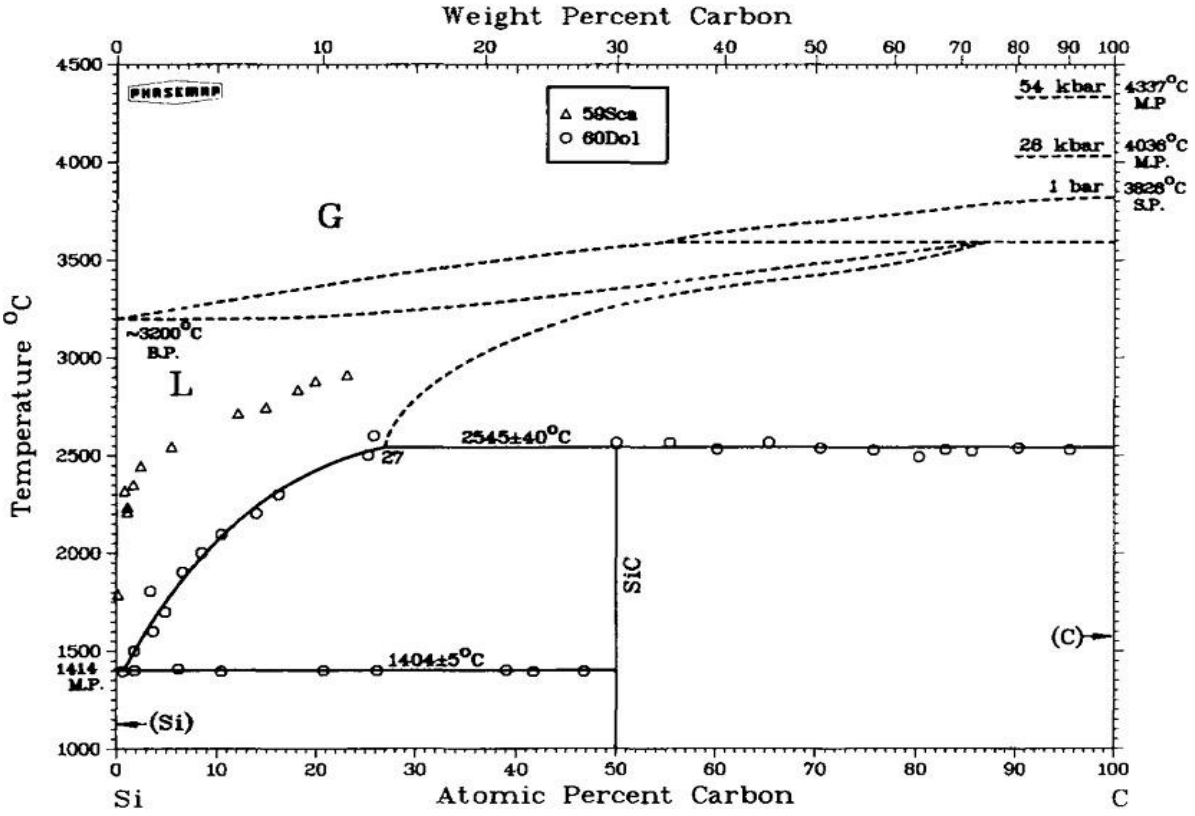


Figure 2.1Phase diagram of silicon carbide [56]

2.3 Synthesis methods of SiC NPs

In recent times, the synthesis of SiC NPs has garnered significant attention, leading to the proposal of various synthesis methods. These methods can be categorised into three primary types: solid phase processes, liquid phase processes, and vapor phase processes (as shown in Table 2.1). NPs produced through different synthesis techniques exhibit distinct characteristics. This section delves into the principles and the latest advancements associated with each synthesis method in detail.

Table 2.1 Synthesis methods of SiC NPs

Categories	**Synthesis Methods**	**Refs**
Solid phase process	High Energy Ball milling	[36], [37], [38]
Solid phase process	Chemical etching	[39], [40], [41]
Solid phase process	Combustion synthesis	[42], [43], [44]
Solid phase process	Carbothermic reduction	[45], [46]
Liquid phase process	Sol-gel	[47], [48], [49]
Vapor phase process	Pulsed laser ablation in liquid	[17], [50], [51], [52]
Vapor phase process	Chemical vapor synthesis	[53], [54], [55]

2.3.1 High Energy Ball-Milling

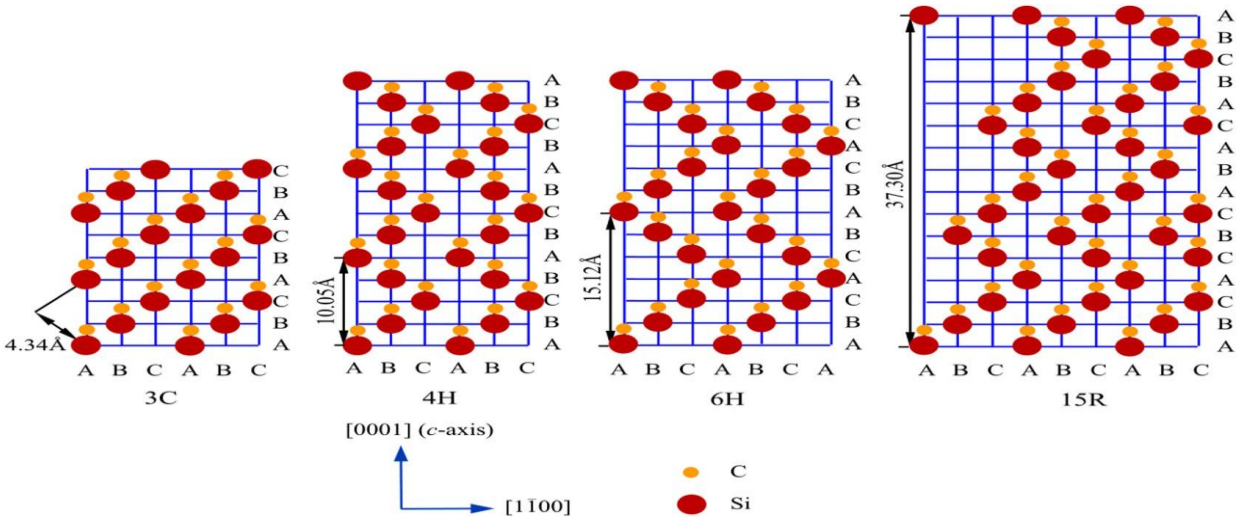


Figure 2.2 Stacking sequences of double-layers of 3C-, 4H-, 6H- and 15R–SiC[29]

Physical milling is a common top-down synthesis technique in material preparation, adept at breaking solid materials into smaller particles. This method relies on the intense local impact generated by the high-speed rotation of high-energy ball milling to disrupt lattice bonds and crush large particles into NPs. In the synthesis of SiC NPs, the initial material may consist of either micro-sized SiC particles or bulk SiC. Rao et al. conducted a study in which micro-sized SiC particles were fragmented into SiC NPs using high-energy ball milling, with a focus on exploring the influence of milling time on the resulting product [51]. Characterisation of the products' crystal structure and chemical composition was performed using X-ray diffractometer (XRD) analysis. The variation in displacement of SiC (111) XRD peaks at different milling times, revealed a decrease in peak intensity and an increase in peak broadening with prolonged milling time. This indicated a reduction in crystallinity due to high-energy milling. According to calculations using the Pseudo-Voigt function, the crystallinity of SiC decreased from 74% to 49% after 50 hours of milling. Additionally, Scherer's equation calculations showed a decrease in the average crystallite size of the products from 108.36 nm to 26.34 nm.

2.3.2 Mechanical Alloying

Mechanical alloying represents a distinct approach from physical milling, harnessing the energy generated through high-energy ball milling to instigate diffusion reactions among reactants, leading to the synthesis of targeted products. As advancements in technology and supporting equipment persist, the range of products attainable through this method has significantly diversified, encompassing intermetallic compounds, amorphous alloys, various carbides, silicides, nitrides, and hydrides. During the high-energy ball milling process, particles undergo progressive refinement through the impacts and extrusions induced by high-energy balls, facilitating the amalgamation of newly exposed surfaces. Moreover, this method promotes the generation of high-density crystal defects within particles. Consequently, under the impetus of free energy, atoms located at the crystal surfaces and grain boundaries diffuse, engendering the formation of novel phases. Ultimately, as reactants are depleted, the synthesis concludes. In the specific case of synthesizing SiC NPs, Si and C particles serve as the raw materials, as depicted in Figure 2.1, which illustrates the Si-C phase diagram[56]. The employment of balls in the milling process typically yields a broad distribution of particle sizes within the product. Noteworthy is the presence of micron-sized particles within the product composition, necessitating further sieving for refinement. Additionally, the significant impact force inherent in high-energy ball milling can induce the formation of amorphous SiC, whilst the wear and tear of milling balls may introduce impurities. Thus, it becomes apparent that mechanical alloying, while efficacious for diverse synthesis objectives, exhibits limitations in attaining the desired high-purity and high-crystallinity SiC NPs.

2.3.3 Chemical Etching

The chemical properties of SiC necessitate the use of a specialised etching solution during the synthesis process of SiC NPs. Zhu et al.[57] employed a mixture of concentrated nitric acid (HNO_3) and hydrofluoric acid (HF) as the etching solution. The synthesis process comprised two primary steps: initially, the starting bulk β-SiC underwent etching at 100°C for 1 hour to yield porous SiC. Under these conditions, HNO_3 facilitated the oxidation of a portion of SiC to SiO_2, subsequently removed by HF. Subsequently, the porous SiC underwent

ultrasonic treatment in ethanol for 30 minutes to yield β-SiC NPs with diameters less than 6.5 nm. Karolyhazy et al.[40] , alternatively, utilised 6H–SiC as the starting material and employed a mixture of Na2S2O6 solution and HF as the etching solution. The etching process was conducted at 150°C for 2 hours, resulting in NPs as small as 1 nm in size. These investigations underscored the capability of chemical etching to synthesise NPs with exceedingly minute particle dimensions and diverse crystal structures contingent upon the choice of raw materials. Moreover, besides the aforementioned etching of bulk SiC with specialised solutions, electrochemical etching presents an alternative approach. Similar to conventional chemical etching, this method necessitates ultrasonic treatment to generate SiC NPs from porous SiC. Wu et al[58]. employed electrochemical etching to synthesise SiC NPs and examined the impact of etching current densities on the resultant products. The particle size exhibited a slight increase with higher etching current densities, with the maximum particle size remaining less than 10 nm. Regarding the crystal structure of the product, research conducted by Rossi et al.[59] successfully synthesised 6H–SiC NPs utilising bulk 6H–SiC as the starting material. However, Fan et al.[60] observed polytypic transformation of SiC NPs upon ultrasonic treatment. They posited that the energy required for such transformation in SiC NPs was considerably lower than that in bulk SiC, thereby facilitating polytypic transformation under ultrasonic treatment. In contrast to high-energy ball milling techniques, chemical etching offers the capability to generate single-crystal SiC NPs with even smaller particle sizes. Nonetheless, this method necessitates the use of hazardous raw materials such as HF and HNO3, markedly heightening process-related risks. Moreover, the high cost associated with procuring these materials coupled with low yield rates pose significant constraints on the scalability and widespread adoption of this method. Consequently, while chemical etching demonstrates efficacy at the laboratory scale, its feasibility for large-scale production remains challenging.

2.3.4 Combustion Synthesis

Combustion synthesis, a traditional method for material synthesis, has garnered considerable attention for its

rapid reaction kinetics and high conversion rates. The reaction mechanism for synthesising SiC from Si and C is relatively straightforward, thus making this method widely acknowledged and studied. Combustion synthesis encompasses various heating approaches, with one of the most direct methods involving placing mixed reactants into a furnace. For instance, researcher[61] employed a furnace to synthesize β-SiC NPs, investigating the effects of different reaction conditions. Their findings revealed that variations in reaction temperature, heating rate, and reaction duration could influence the product. Higher reaction temperatures, faster heating rates, and longer reaction times tended to enhance the reaction conversion rate. Additionally, another research[42] elucidated the relationship between the crystal structure of the resulting SiC and reaction temperature. At 1800°C, β-SiC predominantly formed, whereas at 1950°C, α-SiC emerged in the product. Further temperature increases led to a gradual rise in -SiC content, potentially attributed to the exothermic reaction surpassing the transition temperature of SiC, resulting in the conversion of β-SiC to -SiC. Despite the rapid and efficient production of SiC through the combustion reaction between C and Si, stringent requirements exist for the C sources. Obtaining SiC NPs necessitates C sources with similar or smaller particle sizes, significantly elevating production costs. Consequently, efforts have been directed towards exploring precursors of C to synthesize SiC NPs, including fullerenes, sucrose, and others. These precursors, compared to C particles, exhibit the potential to increase the reaction interface area of reactants, thereby enhancing reaction rates and conversion rates. To conclude, enhancing the controllability of combustion synthesis poses a significant challenge for future research and development efforts.

2.3.5 Carbothermic reduction

Carbothermal reduction, a high-temperature reduction reaction involving carbon as a reducing agent, offers several advantages including low cost, simplicity in principle, strong process designability, and high conversion rates. This section provides a detailed overview of various carbothermal reduction methods employed for synthesising SiC NPs. The utilisation of carbothermal reduction for SiC synthesis dates back to 1893 when Acheson first synthesised scaly SiC from a mixture comprising quartz sand, coke, a small quantity of wood chips, and NaCl at elevated temperatures. However, owing to the large particle size of the reactants used

during that period, the reaction interface area was limited, resulting in a thick reaction product layer. Consequently, the reaction necessitated exceedingly high temperatures (2700°C). Increasing the reaction interface area of the reactants can increase the conversion rate, reduce the reaction temperature, and refine the diameter of obtained particles. Zhong et al.[62] mechanically activated C and SiO2 particles in advance and used the mixed particles to synthesise SiC particles. After milling the reactants, the particle size of the product could be significantly reduced, and SiC could be synthesised at a temperature much lower than that of the Acheson method. They finally synthesised β-SiC NPs with a particle size of 30 nm at 1500°C. However, agglomeration is clearly present in these SiC particles. The carbothermal reduction process for synthesising SiC necessitates high-temperature heating, approaching the melting point of SiO2. Consequently, SiO2 particles are susceptible to agglomeration, leading to undesired particle morphology in the resultant product. In contrast to the combustion method, synthesising SiC through carbothermal reduction entails an endothermic reaction, rendering the control of reaction temperature more manageable. Furthermore, the generation of SiO gas during the reaction enhances the thoroughness of reactant interaction, thereby augmenting the reaction's conversion rate. However, the high reaction temperature characteristic of this process renders conventional methods of reactant mixing susceptible to agglomeration.

2.3.6 Sol-gel

The preparation of SiC NPs via the sol-gel method typically involves using liquid Si-containing materials, such as colloidal SiO2, tetraethyl orthosilicate, and methyl trimethoxysilane, alongside carbon sources like phenolic resin, sucrose, and starch. Alternatively, organic silicon polymers containing both Si and C can serve as reactants. The synthesis process comprises two main stages: firstly, the formation of a reaction precursor through hydrolysis, gelation, and drying, followed by high-temperature heat treatment to produce SiC. This method, essentially grounded in carbothermal reduction, offers an advantage over conventional methods by mitigating the non-uniform mixing of SiO2 and C particles, thereby enhancing the reaction. However, the hydrolysis and gelation process in the sol-gel method typically span several days, necessitating the addition of catalysts to expedite the reaction. For instance, Li et al.[63] employed tetraethyl orthosilicate (TEOS) and

phenolic resin as reactants, supplemented with oxalic acid (OA) and hexamethylenetetramine (HMTA) as catalysts. The results indicated that oxalic acid (OA) primarily regulated the pH of the mixed solution, influencing the hydrolysis rate of tetraethyl orthosilicate (TEOS) - an excessively high or low pH value could diminish its hydrolysis rate. Conversely, hexamethylenetetramine (HMTA) predominantly facilitated coagulation and gelation of the solution. The addition of dispersant and adjustment of reaction times could impact the size and morphology of SiC particles. Najafi et al.[47] utilised TEOS and resol as reactants to synthesise β-SiC, incorporating ammonium polycarboxylate (APC) as a dispersant during the gelation process to control product diameter and solution stability. Their findings revealed that a pH value below 4 yielded a stable solution with β-SiC NPs diameters controllable within 10 nm. However, when the pH value ranged from 4 to 7, solution stability decreased, resulting in significantly larger particle sizes. The results indicated that oxalic acid (OA) primarily regulated the pH of the mixed solution, influencing the hydrolysis rate of tetraethyl orthosilicate (TEOS) - an excessively high or low pH value could diminish its hydrolysis rate. Conversely, hexamethylenetetramine (HMTA) predominantly facilitated coagulation and gelation of the solution. The addition of dispersant and adjustment of reaction times could impact the size and morphology of SiC particles. Najafi et al. utilised TEOS and resol as reactants to synthesise β-SiC, incorporating ammonium polycarboxylate (APC) as a dispersant during the gelation process to control product diameter and solution stability. Their findings revealed that a pH value below 4 yielded a stable solution with β-SiC NPs diameters controllable within 10 nm. However, when the pH value ranged from 4 to 7, solution stability decreased, resulting in significantly larger particle sizes. Various examples of synthesising SiC NPs using diverse raw materials via the sol-gel method are summarised. While the sol-gel method facilitates even mixing of reactants through hydrolysis and gelation processes, it also complicates the procedure. Additionally, particles tend to transform into whiskers and nanowires during heating the gel for SiC NPs preparation, owing to heterogeneous nucleation and gradient-oriented nucleation mechanisms. Hence, inhibiting this transformation of SiC NPs into whiskers during the reaction process poses an urgent challenge for the sol-gel method.

2.3.7 Pulsed Laser Ablation in Liquid

Recently, a novel method for synthesising SiC NPs, termed pulsed laser ablation in liquid (PLAL), has emerged. This method, depicted in Fig. 2.3 involves the use of pulsed laser ablation of a target to generate NPs. Upon irradiation of the target with a laser beam of sufficient energy, high pressure and temperature are promptly generated at the liquid-solid interface. Under these conditions, the target undergoes ablation into NPs, which are subsequently obtained by evaporating the solution. PLAL offers several advantages, including a simple process, environmental friendliness, low cost, and high purity of the product NPs. Shuaib et al.[64] successfully synthesised SiC NPs by ablating SiC targets in water. Transmission electron microscopy (TEM) analysis revealed that the majority of the obtained particles were β-SiC with particle sizes below 5 nm. To provide a more intuitive characterisation of the crystal structure of the product SiC, they conducted fast Fourier transform (FFT) analysis on the TEM image. As illustrated in, numerous non-periodic changes in crystalline directions were observed in particles with larger sizes (10 nm), indicative of defects in large grains. Additionally, they observed that the photoluminescence spectrum of the product resembled that of 6H–SiC. It is conjectured that the high temperature and pressure induced by the laser pulse may convert a portion of β-SiC into 6H–SiC. Castelletto et al.[50] utilised 4H–SiC as the target and synthesised 4H–SiC NPs through laser ablation in water. The photoluminescence spectrum indicated that the product NPs retained the Si vacancies present in the bulk 4H–SiC, suggesting that the NPs were fragments of the starting bulk materials. The aforementioned studies primarily focused on synthesising SiC NPs through ablating SiC targets. However, there are also reports utilising Si as targets, where the synthesis of SiC NPs is achieved through the reaction of the solution and Si NPs produced by ablation. Yang et al.[51] were the first to accomplish the synthesis of SiC NPs using Si tar-gets via the PLAL method. They employed ethanol as the reaction solvent and placed a Si wafer at the bottom as the target. Analysis of the product revealed a small amount of Si impurity, which was subsequently removed through treatment with HF and H2O2, resulting in high-purity β-SiC NPs with a diameter of 3.5 nm. Furthermore, the laser power in this method influences the synthesis of SiC NPs. Khashan et al.[12] synthesised SiC NPs using

lasers with varying intensities (1.5–5 J/cm2), demonstrating that laser intensity affects the diameter of the products. Atomic force microscopy (AFM) was utilised to estimate the particle size distribution, revealing an increase in particle diameter from 55 nm at an intensity of 1.5 J/cm2 to 78 nm at 5 J/cm2 intensity. Yu et al.[52] utilised hexane as the reaction solution and conducted a detailed characterisation of the product. They observed that large product particles with diameters exceeding 100 nm contained unreacted Si, whereas smaller particles exhibited a single crystal structure indicative of SiC . They speculated that insufficient thermal energy hindered the formation of SiC in the inner areas of large particles, resulting in the presence of Si. The PLAL method demonstrates significant potential for synthesising SiC NPs, yielding a homogeneous colloidal solution conducive to further SiC NPs applications. Additionally, NPs obtained through ablating SiC targets in water retain their original crystal structure, enabling the synthesis of -SiC NPs. However, scalability remains a challenge, limiting commercial applications of this method.

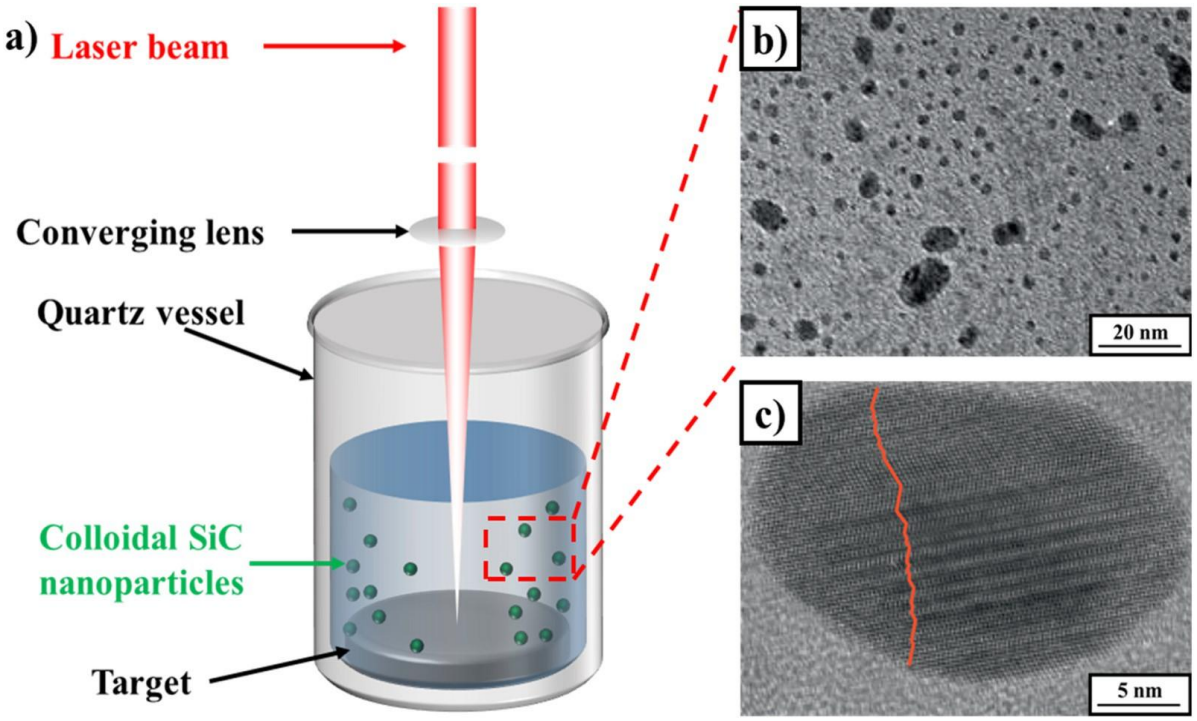


Figure 2.3 Schematic diagram of pulsed laser ablation in liquid to synthesize SiC NPs; b) TEM image of product SiC NPs via pulsed laser ablation in liquid method; c) Single β-SiC NPs for which an improvement of the compact planes imaging by Fast Fourier Transform treatment was performed [2].

2.3.8 Chemical Vapor Synthesis

The synthesis of nanomaterials through gas-phase reactions primarily involves two methods: physical vapor deposition (PVD) and chemical vapor deposition (CVD). However, due to the high boiling point of SiC, PVD is not a feasible method for its synthesis. In contrast, CVD operates on the principle of heating gaseous reactants and allowing them to chemically react at elevated temperatures to form products. Initially utilized for coating surfaces, CVD has undergone advancements enabling the synthesis of nanomaterials, a process often referred to as chemical vapor synthesis.In CVD, the reactants evaporate and react within the reactor, after which the resulting NPs are separated and purified using various methods in a flowing gas environment. CVD offers several advantages including shorter processing times, narrower diameter distributions, smaller average diameters, and higher particle purity, making it an increasingly researched area. Ultrafine, high-purity SiC NPs can be synthesised by precisely controlling the reaction conditions in CVD. Huang et al.[65] employed dimethyldichlorosilane (DMS) as reactants for synthesising SiC NPs, investigating the effects of reaction temperature, reaction gas concentration, and reaction gas flow rate. Their findings revealed that increasing the reaction temperature and the concentration of the reaction gas led to larger particle sizes in the products, while the reaction gas flow rate had minimal influence. Theitionally, they observed that at reaction temperatures below 1300°C, Si impurities were present in the product, whereas at 1400°C, the Si content in the product was significantly reduced. Hitherto, CVD has spawned a variety of technologies, including plasma CVD (PCVD), hot wire CVD (HWCVD), laser CVD (LCVD), etc. These technologies exhibit diverse reaction mechanisms and process conditions. Among them, PCVD and LCVD stand out as the most widely utilised methods for synthesising SiC NPs. Diverging from traditional CVD methods heated by reaction furnaces, PCVD and LCVD employ plasma or laser as energy sources, rendering them more environmentally friendly alternatives. Thermal plasma, in contrast to furnace heating, instigates the reaction through the collision of electrons and reactants, allowing for reactions to occur at room temperature. As mentioned previously, CVD offers the capability to produce high-purity SiC NPs with ultra-fine particle sizes

through meticulous control of temperature and reaction gas concentration. Moreover, it encompasses various evolutionary forms such as PCVD and LCVD. Consequently, the selection of the corresponding preparation process can be tailored to suit specific requirements, underscoring its strong flexibility. Furthermore, the FBCVD method facilitates the mass production of SiC NPs. Nonetheless, the reactants employed in the reaction are costly, and the conversion rate of the reaction necessitates improvement. Consequently, the cost associated with synthesising SiC NPs via this method remains prohibitively high.

2.4 Properties of SiC NPs

When comparing NPs with bulk materials, it's notable that NPs possess an exceptionally high specific surface area, thereby rendering surface properties of paramount importance. These surface characteristics significantly influence the chemical stability and dispersibility of NPs, consequently impacting their diverse applications. In light of this, researchers have directed attention towards investigating the surface properties of silicon carbide (SiC) NPs.

2.4.1 Surface Properties

Indeed, the surface properties of SiC NPs play a pivotal role in the formulation of stable colloidal solutions and ceramic slurries. While certain synthesis techniques such as the chemical etching method and PLAL method can yield SiC NPs with pronounced hydrophilicity, achieving mass production using these methods often proves challenging. Consequently, researchers have proposed surface modification strategies.

For instance, Iijima et al.[66] explored surface modification approaches employing 2,2-azobisisobutyronitrile (AIBN), 2,2-azobis(2-methylpropionamidine)dihydrochloride (AMPA), and 2,2-azobis[N-(2-carboxyethyl)-2-methylpropionamidine]n-hydrate (ACMPA) to modify SiC NPs individually. The introduction of hydrophilic functional groups, such as amino and carboxyl, represents an effective strategy for enhancing the dispersibility of silicon carbide (SiC) NPs in water, thereby facilitating the

preparation of stable SiC colloidal solutions. Moreover, aside from interacting with surface functional groups, adsorption processes can also contribute to improving particle dispersion within a solution.

In a study conducted by Loganathan et al.[67], the effects of polyethylene glycol and chitosan on the stability of SiC colloidal solutions were investigated. It was observed that oxygen elements present on the surface of SiC NPs could form hydrogen bonds with protons on polyethylene glycol and chitosan. Particularly, chitosan adsorbed on SiC NPs could ionize to generate chitosan cations, thereby enhancing electrostatic repulsion between particles and augmenting the stability of the colloidal solution. Conversely, polyethylene glycol exhibited minimal effect in this regard.

In addition to their application in colloidal solutions, SiC NPs find extensive utility in synthesising polymer-based nanocomposites. However, challenges arise due to Van Der Waals interactions and poor compatibility between SiC and polymers, which hinder uniform dispersion of SiC NPs within the polymer matrix, consequently diminishing nanocomposite performance. To address these challenges, surface modification of SiC NPs emerges as a promising solution.

Surface modification of SiC NPs can be broadly categorised into organic and inorganic approaches. Organic modification entails introducing organic materials onto the surface of SiC NPs through grafting reactions. This process results in the formation of a protective layer of organic materials, which mitigates NPs agglomeration and enhances the bonding strength at the interface between SiC and resin. Conversely, inorganic modification involves treatments such as modification with concentrated nitric acid (HNO3). This treatment induces the appearance of characteristic functional groups on the surface of SiC NPs, facilitating their uniform dispersion within matrices such as polyvinyl alcohol (PVA). The reports discussed above underscore the pivotal role of surface properties in the application of silicon carbide (SiC) NPs. Surface modification treatments emerge as a key strategy to adjust the surface properties of SiC NPs, thereby enabling their utilisation in the fabrication of advanced nanocomposites, functional ceramics, and other novel materials. By modifying the surface characteristics, SiC NPs can be tailored to meet specific requirements, enhancing their compatibility with various matrices and enabling their integration into diverse applications with improved performance and functionality.

2.4.2 Thermal Properties

Silicon carbide (SiC) boasts an exceptionally high melting point of 2700°C and excellent chemical stability, rendering it suitable for the preparation of high-temperature devices. However, at the nanoscale, the large surface area of NPs induces significant disparities in thermal properties. A nascent interdisciplinary theory known as nanothermodynamics has emerged to bridge the understanding between macroscopic and nanoscopic systems. While nanothermodynamics has extensively studied the thermal behavior of metal nanocrystals, investigations into the thermal properties of SiC NPs remain relatively preliminary.

Huseynov et al.[68] employed thermogravimetric analysis (TGA) to assess the thermal characteristics of β-SiC NPs. The analysis revealed fluctuations in NPs mass with temperature, attributed to the adsorption and subsequent removal of impurities, followed by oxidation of SiC at temperatures exceeding 800°C. Further studies explored the impact of neutron irradiation on β-SiC NPs, demonstrating enhanced oxidation resistance post-irradiation without significant alterations in thermal properties, indicative of notable radiation-resistant properties[69].

Recent attention has also been drawn to the thermal properties of nanofluids containing SiC NPs. Research by Xie et al.[70] investigated the influence of solid content on the thermal conductivity of nanofluids, revealing a linear increase in thermal conductivity with the volume fraction of SiC NPs. It showed that the thermal conductivity of the suspension increased linearly with the volume fraction of SiC NPs. When the volume fraction of SiC NPs reached 4.2 percent, the thermal conductivity of the suspension increased by 15.8 percent. Similarly, Timofeeva et al.[71] examined the effects of interfacial and particle size on heat transfer characteristics, concluding that while NPs surface charge did not affect thermal conductivity, smaller particle sizes yielded increased thermal conductivity due to their larger surface area facilitating enhanced solid-liquid interface interaction. With its impressive thermal stability below 800°C and exceptional radiation resistance properties, silicon carbide (SiC) NPs hold vast potential for applications in aerospace and nuclear energy sectors. Furthermore, SiC NPs have demonstrated the capability to notably enhance the thermal conductivity

of nanofluids, showcasing promising prospects for enhancing heat transfer in various applications.

2.4.3 Electrical Properties

Being a third-generation semiconductor, silicon carbide (SiC) exhibits outstanding electrical properties, making it highly suitable for high-frequency semiconductor devices. The size effect has been reported to exert a certain influence on the electrical properties of the material, with some SiC nanomaterials displaying unique electrical characteristics. In this section, we delve into the ongoing research concerning the electrical properties of SiC NPs, encompassing aspects such as dielectric constant and conductivity.

See et al.[72] conducted a study on the impact of temperature and frequency on the dielectric properties of β-SiC NPs. Their findings revealed that the dielectric constant of the material gradually decreased with increasing frequency, with a relaxation peak observed at 10 kHz. Moreover, they observed fluctuations in the dielectric constant of β-SiC NPs with temperature variation, attributed to the simple electron hopping mechanism in the bandgap theory. The introduction of elements into the SiC lattice, replacing Si atoms, leads to the formation of corresponding vacancies due to differences in atomic valence, consequently increasing the dielectric constant. For instance, when Fe atoms, typically in a trivalent state, replace Si atoms in SiC, a p-type material with FeSi defects is synthesized, thereby enhancing the dielectric constant. Moreover, research by Huseynov et al. demonstrated that neutron irradiation could introduce new doping elements into SiC NPs, further augmenting the dielectric constant.

In recent studies, Huseynov et al.[73] investigated the impact of temperature, frequency, and neutron irradiation on the conductivity of SiC NPs. Their findings revealed that conductivity remained relatively unchanged at frequencies below 1 kHz but increased proportionally beyond this threshold. Regarding temperature, conductivity exhibited a significant increase at frequencies below 1 kHz, suggesting that higher temperatures and frequencies could induce SiC NPs to generate more carriers. Additionally, neutron irradiation was observed to induce a nuclear phase transition of Si atoms and generate 31P, thereby enhancing the concentration of n-type donors and increasing conductivity. The aforementioned findings underscore the

potential for enhancing the electrical properties of SiC NPs through element doping and neutron irradiation, thereby expanding their potential applications.

2.4.4 Biocompatibility Properties

Studies have affirmed the favorable biocompatibility of SiC, with negligible effects on the human body. However, it's noted that SiC nanomaterials diverge from bulk SiC, with SiC whiskers resembling asbestos, posing toxicity risks to cells. Thus, investigations are warranted to assess the biocompatibility of SiC NPs.

The toxicity of SiC nanomaterials to cells may hinge on morphology. Chen et al.[74] compared the toxicity of SiC NPs and nanowires on human mesenchymal stem cells (hM-SCs). Proliferation assays revealed a 30 percent to 37 percent decrease in proliferation of hMSCs labeled with SiC nanowires, whereas those labeled with SiC NPs remained largely unaffected. Moreover, hMSCs labeled with SiC nanowires exhibited inhibited differentiation into osteocytes or adipocytes. Lozano et al.[75] conducted rat studies to assess the toxicity of SiC NPs. Rats administered with SiC NPs showed no signs of damage to their stomach, intestines, liver, or kidneys, with urine analysis revealing no abnormalities, indicating no apparent poisoning effects.

The aforementioned studies highlight that while SiC NPs demonstrate good biocompatibility, they are not entirely biologically inert materials. Pourchez et al.[76] investigated the toxicity of SiC NPs using a cell line derived from murine peritoneal macrophages. While SiC NPs did not induce cytotoxic effects, cellular responses related to oxidative stress and inflammation were observed, suggesting potential toxicity. Research on the biocompatibility of SiC NPs has yielded varied conclusions, possibly due to their selective cytotoxicity. Mognetti et al.[77] compared the cytotoxicity of SiC NPs on oral squamous carcinoma and immortalised cell lines, revealing selective inhibition of carcinoma cell proliferation, indicating that SiC NPs exhibit cell-type-dependent toxicity. These findings underscore the influence of cell types on the biocompatibility of SiC NPs. Despite SiC being traditionally regarded as biologically inert, the biocompatibility of SiC NPs warrants reconsideration. Further research on their cytotoxicity is essential to advance their development in medical

and biological applications.

2.5 Application

SiC NPs have found significant application in synthesizing SiC ceramic materials, with extensive research conducted in this domain. However, beyond ceramic synthesis, researchers have diligently explored diverse applications for SiC NPs owing to their exceptional properties. This section delves into novel and intriguing applications of SiC NPs, leveraging their unique characteristics. These applications span various fields, including the development of composites, catalysts, fluorescent biological labels, bio adhesives, and flexible field emitters as shown in Figure 2.4.

2.5.1 Composites

Composites represent a burgeoning field in material science, offering the synergistic combination of individual components to yield outcomes greater than the sum of their parts, a phenomenon often described as ”1 + 1 > 2”. Notably, composites can exhibit properties that surpass those of their constituent materials. Leveraging the diverse properties of silicon carbide (SiC) NPs, composite materials reinforced with them are emerging as promising candidates for structural applications, microwave absorption, corrosion-resistant coatings, and more.

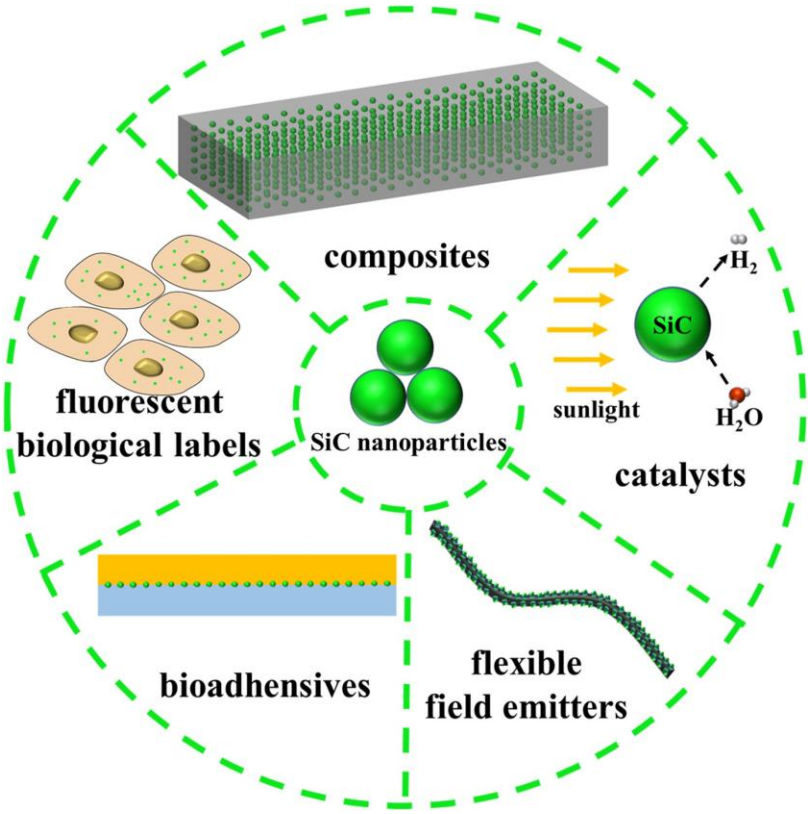


Figure 2.4 Applications for SiC NPs [3].

2.6 Summary

In recent years, there has been a surge in interest regarding the synthesis of silicon carbide (SiC) NPs, driven by their unique properties and potential applications. Researchers have developed various methods for synthesising these NPs, which can broadly be categorised into three main types: solid phase processes, liquid phase processes, and vapour phase processes. Solid phase processes involve techniques such as high energy ball milling and mechanical alloying. These methods essentially break down solid materials, either micro-sized SiC particles or bulk SiC, into smaller NPs. High energy ball milling, for example, relies on intense local impacts generated by the rapid rotation of milling balls to disrupt lattice bonds and crush large particles into NPs. While these methods offer scalability and facilitate large-scale synthesis, they may introduce

impurities and induce amorphisation in the final product. Liquid phase processes, on the other hand, utilise specialised solutions or precursor materials to generate NPs. Chemical etching and sol-gel are common techniques in this category. Chemical etching involves the use of etching solutions to selectively remove material, yielding NPs with exceedingly small dimensions. Sol-gel methods involve the hydrolysis and gelation of liquid precursors, followed by high-temperature treatment to produce NPs. While these methods offer better control over particle size and purity, they may require hazardous materials and involve complex procedures. Vapour phase processes, including pulsed laser ablation in liquid and chemical vapor synthesis, utilise gas-phase reactions to produce NPs. Pulsed laser ablation in liquid involves irradiating a target material with a laser beam in a liquid medium, leading to the generation of NPs. Chemical vapor synthesis, on the other hand, involves heating gaseous reactants to high temperatures to induce chemical reactions and produce NPs. These methods offer advantages such as short processing times, narrow diameter distributions, and high particle purity. Each synthesis method has its own set of advantages and limitations, ranging from scalability and simplicity to purity and control over particle size. However, PLAL as a new green technology fulfils the requirement of reducing the carbon footprint for fabrication of highly pure SiC NPs. Researchers have discovered that doping SiC NPs with different elements can significantly alter their dielectric properties. To date, various doping strategies have been explored to enhance the dielectric constant of SiC NPs. The properties of SiC NPs encompass a range of characteristics crucial for their behavior and applications. These NPs possess a notably high surface area relative to their volume, making surface properties pivotal in dictating their performance. Surface modification techniques are employed to tailor these properties, enhancing dispersibility in solutions and compatibility with other materials, thereby facilitating their use in various applications such as colloidal solutions, ceramic slurries, and polymer nanocomposites. Furthermore, SiC NPs exhibit exceptional thermal stability and radiation resistance, rendering them suitable for high-temperature applications. Research in nanothermodynamics sheds light on their thermal behaviour, while studies on oxidation resistance and thermal conductivity highlight their potential for enhancing heat transfer in diverse systems. In terms of electrical properties, SiC NPs serve as third-generation semiconductors, boasting outstanding characteristics conducive to high-frequency semiconductor devices.

Investigations into their dielectric constant and conductivity elucidate their behaviour under different conditions, offering insights into strategies such as element doping and neutron irradiation to enhance their electrical properties for expanded applications. Regarding biocompatibility, while SiC NPs have shown promise with minimal effects on the human body, concerns about potential toxicity persist, prompting detailed examination. Studies on their interactions with cells reveal varying responses influenced by factors like morphology and cell type, underscoring the need for ongoing research to ensure their safe and effective use in medical and biological applications.

2.7 Aluminium Oxide Nanoparticles Reinforced Material

Aluminium oxide (Al_2O_3), commonly known as alumina, is one of the most extensively utilised ceramic materials due to its exceptional combination of mechanical, thermal, chemical, and electrical properties[79]. Owing to its high hardness, excellent wear resistance, superior chemical stability, and remarkable thermal resistance, alumina has found widespread applications in abrasives, refractories, cutting tools, biomedical implants, catalyst supports, electronic substrates, and structural composites[80]. The unique characteristics of alumina originate from the strong ionic-covalent bonding between aluminium and oxygen atoms, which provides excellent structural stability even under harsh environmental conditions[81].

In recent decades, significant attention has been directed towards aluminium oxide nanoparticles (Al_2O_3 NPs) because materials at the nanoscale often exhibit properties that differ substantially from their bulk counterparts[82], [83], [84]. The reduction of particle dimensions to the nanometre scale increases the specific surface area and the proportion of surface atoms, resulting in enhanced surface reactivity, improved interfacial interactions, and modified physical and chemical properties. Consequently, Al_2O_3 NPs have emerged as important reinforcing materials in advanced composites, nanofluids, coatings, and functional materials[85].

The incorporation of Al_2O_3 NPs into polymeric, metallic, and ceramic matrices has been shown to significantly improve mechanical strength, stiffness, wear resistance, fracture toughness, and thermal

conductivity[86], [87]. The reinforcing effectiveness of alumina nanoparticles depends on several factors, including particle size, particle morphology, particle distribution, interfacial bonding, and processing technique[88]. Among these parameters, particle size plays a particularly important role because decreasing particle dimensions increases the interfacial area between the nanoparticles and the surrounding matrix. This enhanced interfacial interaction promotes more efficient stress transfer and improves the overall performance of the composite material[89].

The influence of particle morphology on the properties of reinforced composites has also attracted considerable research interest. Spherical alumina nanoparticles generally provide uniform dispersion and minimise stress concentration effects within the matrix. Conversely, elongated or irregularly shaped particles may promote mechanical interlocking and improve reinforcement efficiency but can also increase the likelihood of particle agglomeration. Therefore, achieving uniform dispersion of Al_2O_3 NPs remains one of the primary challenges in the fabrication of high-performance nanocomposites[90].

The crystal structure of alumina is more complex than that of many conventional ceramic materials because aluminium oxide exists in several polymorphic forms. These include α-, γ-, δ-, θ-, κ-, η-, and χ-alumina phases, each possessing distinct crystallographic structures and physicochemical properties[91]. Among these phases, α-Al_2O_3, commonly known as corundum, is the most thermodynamically stable form and exhibits the highest hardness, density, and chemical resistance. The α-phase possesses a rhombohedral crystal structure in which oxygen ions form a hexagonal close-packed arrangement while aluminium ions occupy two-thirds of the available octahedral sites.

In contrast, transition alumina phases such as γ-Al_2O_3 exhibit lower crystallinity and significantly higher specific surface areas. Owing to their porous structures and large surface areas, these phases are extensively utilised as catalyst supports and adsorbent materials. The transformation of transition alumina phases into α-Al_2O_3 generally occurs at elevated temperatures between 1000°C and 1200°C. During this phase transformation process, significant changes occur in particle morphology, crystallinity, porosity, and surface area, which subsequently influence the performance of the resulting material[91].

Since the first successful synthesis of alumina nanoparticles, numerous fabrication techniques have been

developed to control particle size, morphology, phase composition, and surface characteristics. Common synthesis methods include high-energy ball milling[92], chemical precipitation[93], sol-gel processing[94], hydrothermal synthesis[95], combustion synthesis[96], chemical vapour deposition[97], and pulsed laser ablation in liquid (PLAL)[98]. Each method offers specific advantages and limitations regarding particle size control, production yield, purity, crystallinity, and scalability.

For instance, high-energy ball milling is a relatively simple and cost-effective technique capable of producing alumina nanoparticles in large quantities. However, this method may introduce contamination from the milling media and often results in broad particle size distributions. Conversely, wet chemical methods such as sol-gel and precipitation techniques provide better control over particle size and morphology but generally require more complex processing procedures and post-synthesis heat treatment. Hydrothermal synthesis offers excellent crystallinity and phase control, while combustion synthesis enables rapid production of nanoparticles through highly exothermic chemical reactions.

More recently, pulsed laser ablation in liquid has emerged as a promising green synthesis technique for the fabrication of high-purity Al_2O_3 nanoparticles. This method involves the interaction of high-energy laser pulses with a solid target submerged in a liquid medium, producing nanoparticles without the need for chemical precursors or surfactants. Consequently, PLAL offers advantages such as high purity, environmental friendliness, and the ability to produce stable colloidal nanoparticle suspensions.

Beyond their role as reinforcing agents, Al_2O_3 NPs possess numerous functional properties that make them attractive for advanced technological applications[99]. Their excellent thermal stability enables operation at elevated temperatures, while their high dielectric strength and electrical insulation properties facilitate their use in electronic and electrical devices. Furthermore, the biocompatibility and chemical inertness of alumina have encouraged extensive investigation of Al_2O_3 NPs for biomedical applications including dental implants, orthopaedic devices, drug delivery systems, and tissue engineering scaffolds[100].

The large surface area associated with Al_2O_3 NPs also significantly influences their surface chemistry. Surface hydroxyl groups present on alumina nanoparticles can interact with polymers, biological molecules, and other inorganic materials, facilitating surface modification and functionalisation. These surface

engineering approaches are frequently employed to improve nanoparticle dispersion, compatibility with host matrices, and overall material performance.

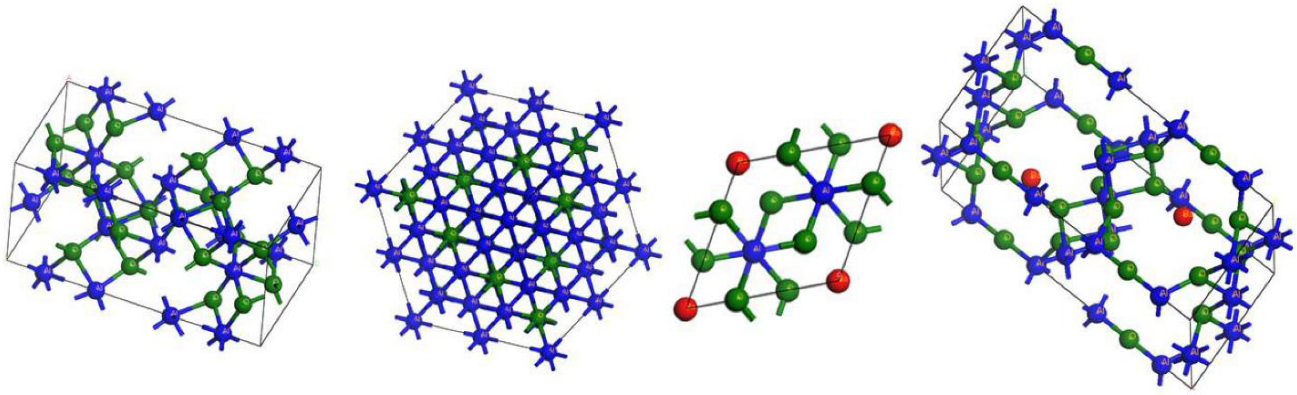
In recent years, growing industrial demand for lightweight, durable, and multifunctional materials has further accelerated research into aluminium oxide nanoparticles. Their ability to simultaneously enhance mechanical, thermal, and tribological properties has made them particularly attractive for applications in aerospace[101], automotive, defence[102], energy[103], and biomedical sectors[104]. Consequently, understanding the synthesis methods, structural characteristics, properties, and applications of Al_2O_3 nanoparticles has become increasingly important for the development of next-generation engineering materials.

The following sections discuss the crystal structures of alumina, the various synthesis techniques employed for producing Al_2O_3 nanoparticles, their physical and chemical properties, and their diverse applications in modern science and engineering.

Crystal Structure and Phases of Al_2O_3

Aluminium oxide (Al_2O_3) is a ceramic oxide material that exhibits a complex polymorphic nature. Unlike many engineering ceramics that exist in a single crystal structure, alumina can occur in several crystallographic phases depending on synthesis conditions, temperature, pressure, and thermal treatment history. The polymorphic behaviour of Al_2O_3 has attracted considerable research interest because each phase possesses distinct structural, thermal, mechanical, and surface properties that influence its suitability for specific applications.

The crystal structure of alumina consists of aluminium cations (Al^{3+}) and oxygen anions (O^{2-}) arranged in highly ordered atomic configurations. The strong electrostatic attraction between these ions gives rise to exceptional hardness, high melting temperature, chemical stability, and mechanical strength. The Al–O bond energy is approximately 512 kJ mol^{-1}, contributing significantly to the excellent thermal and chemical resistance exhibited by alumina[91]. A schematic picture showing the crystallographic structure of Aluminium oxide is illustrated in Figure 2.5.



α-Al_2O_3 γ-Al_2O_3 $BaO{\cdot}Al_2O_3$ Ba-β-Al_2O_3

Crystalline phase	Crystallographic system	Length (Å)		Angle (°)	
α-Al_2O_3	Hexagonal	a	4.759	α	90
		b	4.759	β	90
		c	12.991	γ	120
γ-Al_2O_3	Cubic	a	7.9382	α	90
		b	7.9382	β	90
		c	7.9382	γ	90
$BaO{\cdot}Al_2O_3$	Hexagonal	a	5.209	α	90
		b	5.209	β	90
		c	8.761	γ	120
Ba-β-Al_2O_3	Triclinic	a	5.7072	α	90
		b	17.1216	β	90
		c	40.4870	γ	120

Figure 2.5 Crystalline systems and network parameters of Al2O3[105]

2.8 Synthesis Methods of Al_2O_3 Nanoparticles

The increasing demand for aluminium oxide nanoparticles (Al_2O_3 NPs) in advanced engineering, biomedical, electronic, and catalytic applications has stimulated extensive research into the development of efficient synthesis techniques. The physical, chemical, and structural properties of Al_2O_3 nanoparticles are strongly influenced by the synthesis method employed. Parameters such as particle size, morphology, crystallinity, phase composition, purity, and surface characteristics depend significantly on the preparation

route and processing conditions. Consequently, selecting an appropriate synthesis method is crucial for tailoring the nanoparticles to specific applications.

Various techniques have been developed for the synthesis of Al_2O_3 nanoparticles, which can generally be classified into three major categories: solid-phase processes, liquid-phase processes, and vapour-phase processes. Each category possesses distinct advantages and limitations regarding particle size control, production rate, purity, crystallinity, cost, and scalability. A summary of the synthesis methods of Al2O3 is illustrated in Table 2.3.

Table 2.2 . Summary of synthesis techniques used for synthesising Al2O3 and their relative information

Synthesis Method	**Category**	**Principle**	**Advantages**	**Limitations**	**Typical Particle Size**
High-Energy Ball Milling	Solid-phase	Mechanical reduction of bulk particles through repeated impact and fracture	Simple, low cost, scalable, large production volume	Contamination, agglomeration, broad size distribution	20–200 nm
Chemical Precipitation	Liquid-phase	Formation of aluminium hydroxide precipitates followed by calcination	Easy operation, low processing temperature, economical	Agglomeration during drying, requires calcination	10–100 nm

Sol-Gel Method	Liquid-phase	Hydrolysis and condensation of aluminium precursors to form a gel network	Excellent homogeneity, high purity, precise size control	Long processing time, expensive precursors	5–100 nm
Hydrothermal Synthesis	Liquid-phase	Crystal growth under high temperature and pressure in sealed reactors	High crystallinity, controlled morphology, narrow size distribution	High equipment cost, limited scalability	10–100 nm
Combustion Synthesis	Solid/Liquid-phase	Exothermic reaction between metal salts and fuel compounds	Rapid synthesis, low energy consumption, high yield	Difficult particle size control, agglomeration	20–150 nm
Chemical Vapour Deposition (CVD)	Vapour-phase	Thermal decomposition or reaction of gaseous precursors	High purity, excellent crystallinity, uniform particles	Expensive equipment, complex operation	10–100 nm
Pulsed Laser Ablation in Liquid (PLAL)	Physical/Vapour-phase	Laser irradiation of a solid target immersed in liquid producing nanoparticles through plasma formation and rapid quenching	High purity, environmentally friendly, surfactant-free synthesis	Low production yield, high energy consumption	5–100 nm

2.8.1 High-Energy Ball Milling

High-energy ball milling is one of the most widely employed top-down approaches for the synthesis of aluminium oxide nanoparticles (Al_2O_3 NPs). The technique relies on the repeated fracturing, cold welding, and refinement of larger particles through high-energy collisions between milling balls and the precursor material. Owing to its simplicity, scalability, and relatively low production cost, high-energy ball milling has attracted considerable attention for the large-scale fabrication of ceramic nanoparticles.

The principle of high-energy ball milling involves placing bulk alumina powder together with hardened steel, tungsten carbide, zirconia, or ceramic balls inside a rotating milling chamber. During operation, the balls are accelerated by centrifugal forces and repeatedly collide with the powder particles. These impacts generate localised regions of extremely high pressure and temperature, causing particle fracture and progressive reduction in particle size. As milling continues, the crystallite size decreases from the micrometre range into the nanometre regime.

Several studies have demonstrated the effectiveness of high-energy ball milling for producing nanoscale alumina. Researchers have reported that increasing milling duration generally leads to a reduction in particle size and crystallite dimensions. X-ray diffraction (XRD) analyses commonly reveal peak broadening with prolonged milling time, indicating grain refinement and the development of lattice strain. Transmission electron microscopy (TEM) observations further confirm the formation of nanoparticles with dimensions ranging from several tens of nanometres to below 20 nm depending on the milling conditions.

The milling parameters significantly influence the characteristics of the resulting Al_2O_3 nanoparticles. Important factors include milling speed, milling duration, ball-to-powder ratio, milling atmosphere, ball material, and process control agents. Higher milling speeds increase collision energy and accelerate particle size reduction; however, excessive milling energy may promote particle agglomeration and structural defects. Similarly, increasing the ball-to-powder ratio generally improves milling efficiency by increasing the frequency of particle impacts.

One of the primary advantages of high-energy ball milling is its ability to produce nanoparticles without

the need for complex chemical precursors or expensive processing equipment. Furthermore, the method can readily be scaled for industrial production. The technique is also versatile, allowing simultaneous particle size reduction, mixing, and mechanical alloying processes. Consequently, ball milling has been extensively employed in the preparation of alumina-reinforced composites and nanostructured ceramic materials.

2.8.2 Pulsed Laser Ablation in Liquid (PLAL)

In recent years, pulsed laser ablation in liquid (PLAL) has emerged as a promising technique for the synthesis of high-purity metal oxide nanoparticles, including aluminium oxide nanoparticles (Al_2O_3 NPs). Unlike conventional chemical synthesis methods that require chemical precursors, reducing agents, surfactants, or stabilising compounds, PLAL employs a physical process in which a high-energy pulsed laser irradiates a solid target immersed in a liquid medium. Owing to its simplicity, environmental friendliness, and ability to produce contaminant-free nanoparticles, PLAL has gained increasing attention as a green nanomaterial fabrication technology.

The fundamental principle of PLAL involves focusing a pulsed laser beam onto the surface of an aluminium or alumina target submerged in a liquid environment such as deionised water, ethanol, acetone, or other organic solvents. When the laser fluence exceeds the ablation threshold of the target material, rapid absorption of laser energy occurs at the solid–liquid interface. This interaction generates extremely high local temperatures, often exceeding several thousand Kelvin, accompanied by high pressures within the irradiated region. Under these conditions, material is removed from the target surface in the form of atoms, ions, clusters, and molten droplets, resulting in the formation of a plasma plume.

The plasma plume generated during laser irradiation undergoes rapid expansion within the surrounding liquid medium. Due to the confinement effect imposed by the liquid, cooling rates are extremely high, typically in the range of 10^8–10^{10} K s^{-1}. This rapid quenching promotes nucleation and growth of nanoparticles from the ablated species. Subsequently, the nanoparticles disperse throughout the liquid, forming a stable colloidal suspension without requiring additional stabilising agents.

The characteristics of Al_2O_3 nanoparticles produced by PLAL are strongly influenced by laser parameters and experimental conditions. Important factors include laser wavelength, pulse duration, pulse repetition rate, laser fluence, ablation time, target composition, and liquid medium. Researchers have demonstrated that increasing laser fluence generally increases nanoparticle production rates; however, excessive laser energy may lead to particle aggregation and broad particle size distributions. Similarly, longer ablation times often increase nanoparticle concentration but may also promote secondary laser–particle interactions that alter particle morphology.

The choice of liquid medium plays a crucial role in determining nanoparticle properties. Water is the most commonly employed solvent due to its environmental compatibility and low cost. During laser ablation in water, oxidation reactions readily occur, facilitating the formation of aluminium oxide nanoparticles from ablated aluminium species. Organic solvents such as ethanol and acetone may influence particle growth kinetics, particle stability, and surface chemistry through interactions with the plasma plume and nanoparticle surfaces. Consequently, the selection of an appropriate solvent provides an effective means of controlling nanoparticle characteristics.

Numerous studies have investigated the synthesis of Al_2O_3 nanoparticles using PLAL. Transmission electron microscopy (TEM) analyses commonly reveal nearly spherical nanoparticles with diameters ranging from a few nanometres to several tens of nanometres, depending on processing conditions. High-resolution TEM observations frequently indicate high crystallinity and well-defined lattice fringes, demonstrating the ability of PLAL to produce crystalline nanoparticles directly without requiring extensive post-processing. Furthermore, X-ray diffraction (XRD) studies have confirmed the formation of various alumina phases, including γ-Al_2O_3 and α-Al_2O_3, depending on the laser energy and thermal conditions generated during ablation.

One of the most significant advantages of PLAL is the exceptionally high purity of the resulting nanoparticles. Since the synthesis process does not require chemical precursors or catalysts, contamination from residual reaction by-products is minimised. This characteristic is particularly important for applications in electronics, optics, biomedicine, and advanced composites, where material purity strongly

influences performance. Furthermore, the absence of toxic chemical reagents makes PLAL an environmentally sustainable alternative to many conventional nanoparticle synthesis methods.

Another important advantage of PLAL is its flexibility. By adjusting laser parameters and liquid composition, researchers can tailor particle size, morphology, crystallinity, and surface chemistry. The method also enables the production of stable colloidal nanoparticle suspensions that can be directly utilised in coating technologies, nanofluids, composite fabrication, and biomedical applications without extensive purification procedures.

Despite these advantages, several challenges continue to limit the widespread industrial adoption of PLAL. The production yield of nanoparticles is generally lower than that achieved using conventional chemical synthesis methods. Additionally, the energy consumption associated with laser systems can be relatively high, increasing operational costs. The scalability of PLAL remains a significant challenge because nanoparticle production rates are often insufficient for large-scale manufacturing applications. Researchers are therefore exploring approaches such as high-power laser systems, multi-beam configurations, and continuous-flow reactors to improve production efficiency.

The mechanism of nanoparticle formation during PLAL is also highly complex and remains an active area of research. Processes including plasma formation, cavitation bubble dynamics, shock wave generation, nucleation, growth, and particle fragmentation occur simultaneously within extremely short timescales. A comprehensive understanding of these phenomena is essential for improving process control and optimising nanoparticle quality.

2.8.3 Sol-Gel Method

Among the various techniques employed for the synthesis of aluminium oxide nanoparticles (Al_2O_3 NPs), the sol-gel method is one of the most widely studied and utilised due to its ability to produce highly homogeneous nanoparticles with controlled composition, morphology, and particle size. The process offers several advantages over conventional solid-state synthesis techniques, including lower processing temperatures, excellent chemical uniformity, high purity, and precise control of the final microstructure.

Consequently, the sol-gel method has become an important route for producing alumina nanoparticles for applications in catalysis, ceramics, coatings, sensors, electronics, and composite materials.

The term "sol-gel" refers to the transformation of a colloidal suspension (sol) into a three-dimensional interconnected network (gel). In the synthesis of Al_2O_3 nanoparticles, the process typically begins with aluminium-containing precursors such as aluminium alkoxides, aluminium nitrate, aluminium chloride, or aluminium isopropoxide. These precursors undergo hydrolysis and condensation reactions in the presence of water and suitable solvents, resulting in the formation of a stable colloidal solution. Continued condensation leads to the development of a gel structure containing interconnected aluminium-oxygen bonds.

The hydrolysis reaction can be represented by the interaction of aluminium alkoxide molecules with water molecules, producing hydroxylated species. Subsequently, condensation reactions occur between neighbouring hydroxyl groups, generating Al–O–Al bonds and releasing water or alcohol molecules as by-products. Through these reactions, a three-dimensional inorganic network gradually develops throughout the solution.

After gel formation, the material undergoes an ageing process during which further polymerisation and structural rearrangement occur. The gel is subsequently dried to remove residual solvents and volatile compounds, producing a porous solid known as a xerogel. Finally, calcination at elevated temperatures converts the precursor material into crystalline aluminium oxide nanoparticles. The calcination temperature plays a critical role in determining the phase composition, crystallinity, and particle size of the final product.

Numerous studies have demonstrated that the sol-gel method provides excellent control over nanoparticle characteristics. Researchers have reported the successful synthesis of Al_2O_3 nanoparticles with particle sizes ranging from approximately 5 to 100 nm by carefully controlling reaction parameters such as precursor concentration, pH, solvent composition, hydrolysis rate, and calcination temperature. The ability to manipulate these parameters enables the production of nanoparticles with tailored properties suitable for specific applications.

2.9 Summary

Aluminium oxide nanoparticles (Al_2O_3 NPs) have attracted considerable scientific and industrial interest due to their exceptional mechanical, thermal, electrical, chemical, and biological properties. Extensive research has been conducted on the synthesis, characterisation, and application of alumina nanoparticles using various physical, chemical, and mechanical fabrication techniques. Despite significant advancements in this field, several challenges and knowledge gaps remain, limiting the widespread implementation and optimisation of Al_2O_3 nanoparticle technologies.

One of the primary challenges associated with the synthesis of Al_2O_3 nanoparticles is achieving precise control over particle size, morphology, crystallinity, and phase composition while maintaining high purity and scalability. Conventional synthesis methods such as sol-gel processing, chemical precipitation, hydrothermal synthesis, and combustion techniques often require multiple processing steps, elevated temperatures, chemical precursors, and post-synthesis purification procedures. These requirements may introduce impurities, increase production costs, and generate environmentally undesirable by-products. Consequently, the development of sustainable and environmentally friendly synthesis routes remains an important area of investigation.

Although pulsed laser ablation in liquid (PLAL) has emerged as a promising green synthesis technique for nanoparticle production, studies focusing specifically on the synthesis of Al_2O_3 nanoparticles using PLAL remain relatively limited compared with other nanomaterials. Existing research has primarily concentrated on demonstrating the feasibility of nanoparticle formation, while the influence of laser parameters and solvent properties on nanoparticle characteristics has not been comprehensively explored. As a result, the mechanisms governing particle nucleation, growth, and phase evolution during PLAL synthesis of alumina nanoparticles are not yet fully understood.

Another significant research gap concerns the influence of liquid media on nanoparticle formation during

laser ablation processes. Previous studies have demonstrated that solvent properties such as viscosity, density, surface tension, thermal conductivity, and dielectric constant can strongly affect plasma dynamics, cavitation bubble behaviour, cooling rates, and nanoparticle growth mechanisms. However, systematic investigations examining the relationship between solvent viscosity and the resulting characteristics of Al_2O_3 nanoparticles remain scarce. A deeper understanding of these relationships is essential for controlling particle size distribution, morphology, crystallinity, and colloidal stability.

Particle agglomeration continues to represent a major challenge in the synthesis and application of Al_2O_3 nanoparticles. Due to their high surface energy, nanoparticles tend to aggregate during synthesis, storage, and processing. Agglomeration reduces effective surface area, alters particle size distribution, and negatively impacts performance in composite, catalytic, and biomedical applications. Although various surface modification and dispersion techniques have been proposed, achieving long-term colloidal stability without compromising material purity remains an unresolved issue.

The phase composition of alumina nanoparticles also requires further investigation. Alumina exists in several polymorphic forms, including α-, γ-, δ-, θ-, and κ-Al_2O_3, each possessing distinct physical and chemical properties. While numerous studies have reported phase transformations during thermal processing, the influence of synthesis conditions on phase formation during PLAL remains insufficiently understood. Further research is required to establish reliable methods for controlling phase composition during nanoparticle production.

In the area of nanocomposite development, the relationship between nanoparticle characteristics and reinforcement efficiency remains an active field of research. Although Al_2O_3 nanoparticles have been shown to improve the mechanical, thermal, and tribological properties of composite materials, inconsistencies in reported results frequently arise due to differences in particle size, morphology, surface chemistry, and dispersion quality. A more comprehensive understanding of nanoparticle–matrix interactions is therefore required to optimise composite performance.

Similarly, the application of Al_2O_3 nanoparticles in thermal management systems continues to present challenges. While numerous studies have reported enhanced thermal conductivity in alumina-based

nanofluids, the underlying heat transfer mechanisms remain a topic of debate. Issues related to sedimentation, stability, viscosity increase, and long-term performance must be addressed before widespread industrial implementation can be achieved.

From a biomedical perspective, although Al_2O_3 nanoparticles are generally considered biocompatible, uncertainties remain regarding their long-term biological interactions and potential toxicity. Most investigations have focused on short-term in vitro studies, while comprehensive in vivo assessments remain limited. Further research is required to understand nanoparticle biodistribution, cellular uptake mechanisms, long-term accumulation, and clearance pathways in biological systems.

Recent advances in laser-based nanoparticle synthesis, nanocomposite engineering, and nanofluid technologies have created new opportunities for the development of high-performance alumina nanomaterials. Future research should focus on improving process control, enhancing nanoparticle stability, increasing production efficiency, and establishing clear relationships between synthesis parameters and material properties. In particular, environmentally friendly techniques such as PLAL offer considerable potential for producing high-purity nanoparticles without the use of hazardous chemical reagents.

Therefore, continued investigation into the synthesis and optimisation of Al_2O_3 nanoparticles is essential for overcoming current limitations and expanding their application across engineering, biomedical, environmental, and energy-related fields. The present research contributes to this objective by exploring the synthesis of aluminium oxide nanoparticles using pulsed laser ablation in liquid and examining the influence of solvent properties on nanoparticle characteristics and performance.

3 Chapter 3

Fabrication of Silicon Carbide Nanoparticles Using Pulsed Laser Ablation in Liquid and Viscosity Optimisation via Solvent Tuning

Abstract

In this study, silicon carbide nanoparticles (NPs) were produced through the implementation of pulsed laser ablation in liquid, aiming to investigate the influence of processing parameters on the properties of the resultant NPs and their applicability for inkjet printing. The samples were analysed using ultraviolet-visible spectroscopy, revealing an increase in NPs concentration with increasing the laser power percentage and a peak at the wavelength of 195nm representing produced polyynes. Dynamic light scattering was employed to determine the size distribution of the NPs, demonstrating a range of 89 to 155 nm. Notably, an inverse relationship was established between increasing laser scanning speed and pulse repetition rate (PRR), and the mean size of the NPs. Higher PRR and laser power exhibited an augmentation in the concentration of NPs. Conversely, an increase in scanning speed resulted in a reduction in NPs concentration. Examination of the resulting NPs through field emission scanning electron microscopy unveiled a predominantly spherical morphology, accompanied by minor instances of particle agglomeration. Furthermore, the modulation of colloidal solution viscosity was explored by incorporating glycerol, yielding a maximal viscosity of 10.95 mPa.s.

Keywords: nanoparticles, laser, synthesis, silicon, SEM, PLAL, ceramics

3.1 Introduction

Nanoparticles (NPs) have garnered significant technological interest owing to their multifaceted functions, wide-ranging applications, and distinctive physicochemical attributes[106]. One of the key characteristics that make NPs particularly intriguing is their substantial surface area-to-volume ratio. This feature renders them highly reactive and imparts exceptional catalytic, optical, physicochemical, and magnetic properties when compared to bulk materials[107]. In terms of practical applications, metal NPs have found extensive use across diverse industrial sectors. They are employed in nano filters for wastewater treatment within the petroleum industry[108], serve as heterogeneous catalysts in chemical processes[109], play a role in photodetectors used in the automotive and aerospace sectors[110], [111], find application as quantum dots in the semiconductor industry[112], and have important roles in disease diagnosis and drug delivery within the medical and pharmaceutical fields[113]. These NPs can be classified through different approaches, primarily based on either a top-down method (transforming bulk materials into powder or particle forms) or bottom-up approaches (building up from individual atoms to nanoclusters) including physical, chemical, and biological methods[114]. Chemical methods have been idely used for many years. However, they have some challenges as they involve the use of precursors, surfactants, capping agents, and solvents to stabilize and control particle formation. This can lead to issues such as residual contamination, difficulties in functionalizing particles, and potential environmental harm. Biological synthesis represents a green and environmentally friendly approach to NP production which utilizes extracts from various biological sources, including plants (such as algae, fungi, and yeast), microbes, and natural materials[115]. This method has shown promise in producing biocatalysts in the agriculture sector and is under ongoing research for other applications. However, significant improvements are still required to scale up this technology for commercial NP production. Physical methods involve a top-down approach to NP synthesis, which can be implemented to avoid solvent contamination. These methods typically employ high-temperature and high-pressure conditions to stabilize and control particle growth. Physical methods are attractive to researchers and industries due to their environmentally friendly nature. However, they can be challenging in terms of

cost-effectiveness, as the manufacturing equipment and energy requirements for large-scale NP fabrication can be expensive.

Pulsed laser ablation in liquid (PLAL) is a top-down method of synthesizing NPs, which involves laser irradiation of a target that is submerged in a liquid medium to produce NPs based on the material of the target[116], [117], [118], [119]. There has been increasing interest in the implementation of PLAL in recent years to generate colloids for various applications. The PLAL process is operated within a relatively straightforward system that is kept at room temperature[118]. The technique has been used for synthesizing different metallic NPs including magnesium[4], [120], carbon[121], [122], gold[6], silver[7], [8], silicon[123], and ceramic NPs including silicon carbide[123], [124], [125] titanium oxide[13] silver oxide[8]. PLAL has a variety of advantages over other NPs production methods due to the low cost of equipment for atmospheric ablation, the simplicity of the method which does not require a special environment such as a vacuum, and the ability to alter the properties and morphology of the NPs by changing the laser parameters and liquid media[13], [126]. Parameters in PLAL include laser fluence, pulse repetition rate (PRR), scanning speed, ablation time, and liquid media. These affect the physical or chemical properties of produced NPs.

Moreover, silicon carbide SiC is a promising wide-bandgap semiconducting material that exhibits superior and attractive properties such as high breakdown field strength, high chemical stability, high thermal conductivity, outstanding resistance to oxidation and corrosion, and extreme hardness. SiC NPs have been used widely in various applications that require high temperatures and high frequency such as light-emitting diodes, and UV detectors. In addition, SiC has excellent high-temperature properties such as oxidation resistance, high thermal conductivity, and low thermal expansion coefficient so that it can be used as raw material for advanced refractories, functional ceramics, and abrasive[124], [127], [128]. There are several ways to produce SiC NPs, where PLAL has significantly emerged in the past years due to its benefits rather than other methods. For instance, Castelleto et al.[16] fabricated 4H-SiC NPs using ultra-short pulsed laser ablation for biomedical imaging applications, whereas Yamada et al.[17] studied the resulting sizes, shapes, and crystal structure of produced SiC NPs using femtosecond PLAL in acetone. Few data have been

reported on the pulsed laser ablation in liquid of SiC NPs in DI water using nanosecond laser source, which requires further investigation to understand the correlation of the PLAL parameters and SiC NPs properties[129], [130], [131], [132].

Despite numerous reports on SiC nanoparticle production via PLAL for a wide range of applications, a noticeable gap in the literature pertains to studies that establish a correlation between the properties of the resulting NPs and their suitability for inkjet printing applications. Recognizing this deficiency in existing research, this study's principal objective is to address this knowledge gap. It seeks to examine and establish the connection between the characteristics of SiC NPs synthesized through PLAL and their applicability in inkjet printing applications. By doing so, this research aims to provide valuable insights that can enhance the understanding and utilization of SiC NPs in the context of inkjet printing, thereby advancing this field of study.

3.2 Experimental

3.2.1 NPs Synthesis

The effect of laser power percentage, pulse repetition rate (PRR), and scanning speed on the fabrication of SiC NPs from a rod target (99.9% purity, diameter of 5.0mm, and reaction bonded supplied from Goodfellow) was investigated. The rod was cut into 50 pieces each having a 5 mm height and 5 mm diameter. The target was polished (using a 2000 grit size polishing paper) before each laser ablation process and placed vertically into a 100 ml glass beaker. A 3 × 3 full factorial design of the experiment as shown in Table 3.1 was created using Design Expert software, where three different laser power percentages (60, 80, 100), PRR (10, 30, 50 kHz), and scanning speeds (1, 2, 3 m/s) were investigated (27 samples in total). The ablation time, laser spot diameter, and liquid media were kept constant at 5 min, 50 μm, and de-ionized

water respectively. Ablations were performed using a Nd:YAG laser system (WEDGE HF 1064, Bright Solutions) with pulses centered at 1064 nm with a pulse width of 600 ps at a repetition rate of 10 kHz. The target was submerged in DI water in a 100 ml glass beaker so that a 5 mm distance was kept between the surface of the water and the target. The laser was used to ablate the target using an Archimedean spiral pattern as a scanning strategy with an outer diameter of 2 mm and a hatch spacing of 50 µm.

Table 3.1Design of experiments used for production of sample colloids

Level	**-1**	**0**	**1**
Laser power percentage (%)	60	80	100
Scanning speed (m/s)	1	2	3
PRR (kHz)	10	30	50

3.2.2 NPs Characterisation

Ultraviolet-visible spectroscopy (UV-Vis) measurements were conducted, and the absorbance was recorded for SiC NPs as a measure of NPs yield. UV-Vis was conducted with a Shimadzu UV-2600 UV-Vis spectrometer using a quartz cuvette, Helma (10 mm pathlength) and scan range of 185- 300 nm. Before conducting the measurements, the baseline scan was measured to ensure that the UV-Vis absorbance detector was working properly and conditions inside the capillary were conducive to successful analyte detection. All the optical spectra were corrected for the liquid medium absorption by subtracting its contribution from the recorded spectrum. Moreover, the NPs mean sizes and concentrations (particles per ml) were measured using Dynamic Light Scattering (DLS) Malvern Zetasizer Ultra, where three measurements were taken for each sample and averaged. The absorbance coefficient and refractive index of SiC were obtained and inserted as input parameters for DLS. Furthermore, Field Emission Scanning

Electron Microscopy (FESEM) was performed using a Hitachi S5500 Field Emission SEM. A drop (0.1 µl) of SiC colloid was placed on a 400-mesh size copper grid (purchased from Agar Scientific) and air pumped for 2 minutes to evaporate the water of colloids (drop-casting) before examining within the SEM. The viscosity of the colloids was measured using a viscometer (Brookfield Ametek DVNext Cone/Plate Rheometer) with a rotational speed of 60 RPM at 25 ˚C for 5 minutes. The machine was calibrated before measuring each sample's viscosity. First, the viscosity of samples was measured without adding any additive to colloids, then by adding three different additives into the colloids including Acetone (99.9 % purity sup- plied from Sigma-Aldrich), Isopropyl alcohol (99.9% purity supplied from Sigma-Aldrich), and glycerol solution (86% purity supplied form Sigma-Aldrich). The viscosity was measured three times and averaged for each sample.

3.3 Results and Discussion

3.3.1 Visual inspection and Ultraviolet-visible spectroscopy

Figure 3.1a shows the beaker containing DI water with the target SiC sample, and Figure 3.1b shows the same beaker with the target after 5 min of laser ablation, where the color of the liquid medium has changed from colorless to brown . This observation has been reported in previous work [16], where the color transition is attributed to presence of SiC NPs within the liquid medium. In Figure 3.1c, 3.1d, and 3.1e, a set of samples is shown which were prepared in a constant PRR of 50 kHz and the laser power percentage of 60, 80, and 100, and different scanning speeds of 1, 2, and 3 m/s from left to right respectively. By increasing the laser power percentage from 60 to 100, a slight change in the intensity of the color from light brown to dark brown was observed. The color difference before and after the PLAL is attributed to the presence of SiC NPs and a slight intensity change of the brown color for the laser power percentage of 60 to dark brown for the laser power percentage of 100 is associated with the increasing the NPs yield across the liquids[16]. Therefore, visual inspection indicated that increasing the laser power percentage and scanning speed resulted in

increasing the nanoparticles yield. Furthermore, UV-Vis analysis was performed on each sample after the experiments to confirm the presence of the SiC NPs (Figure 3.2). The pattern of DI water was subtracted from the overall spectrum by putting a reference sample of DI water into the instrument while the colloid spectrum was recorded. In Figure 3.2 (a-c) the spectrum of UV-Vis for produced colloid samples was categorized based on the same laser power percentage and various scanning speeds and PRRs (from left to right laser power percentage of 60, 80, and 100 with scanning speeds 'ss' between 1, 2, 3 m/s and PRRs of 10, 30, 50 kHz respectively). Generally, all the recorded spectra showed a similar trend with a peak at 195 nm that can be correlated to the formation of polyynes during the synthesis of carbon NPs DI water[133]. This peak also has been reported in a previous work[123]. Furthermore, increasing the laser power percentage resulted in increasing the optical absorption index, which is attributed to increasing the concentration of the NPs within the liquid. This can happen because higher laser power percentage typically provides more energy to vaporize or ablate the target material, leading to the production of more nanoparticles[134]. Moreover, at higher wavelengths up to 300 nm, the absorption of resulting SiC NPs in all the laser power percentages falls linearly and tends to saturate.

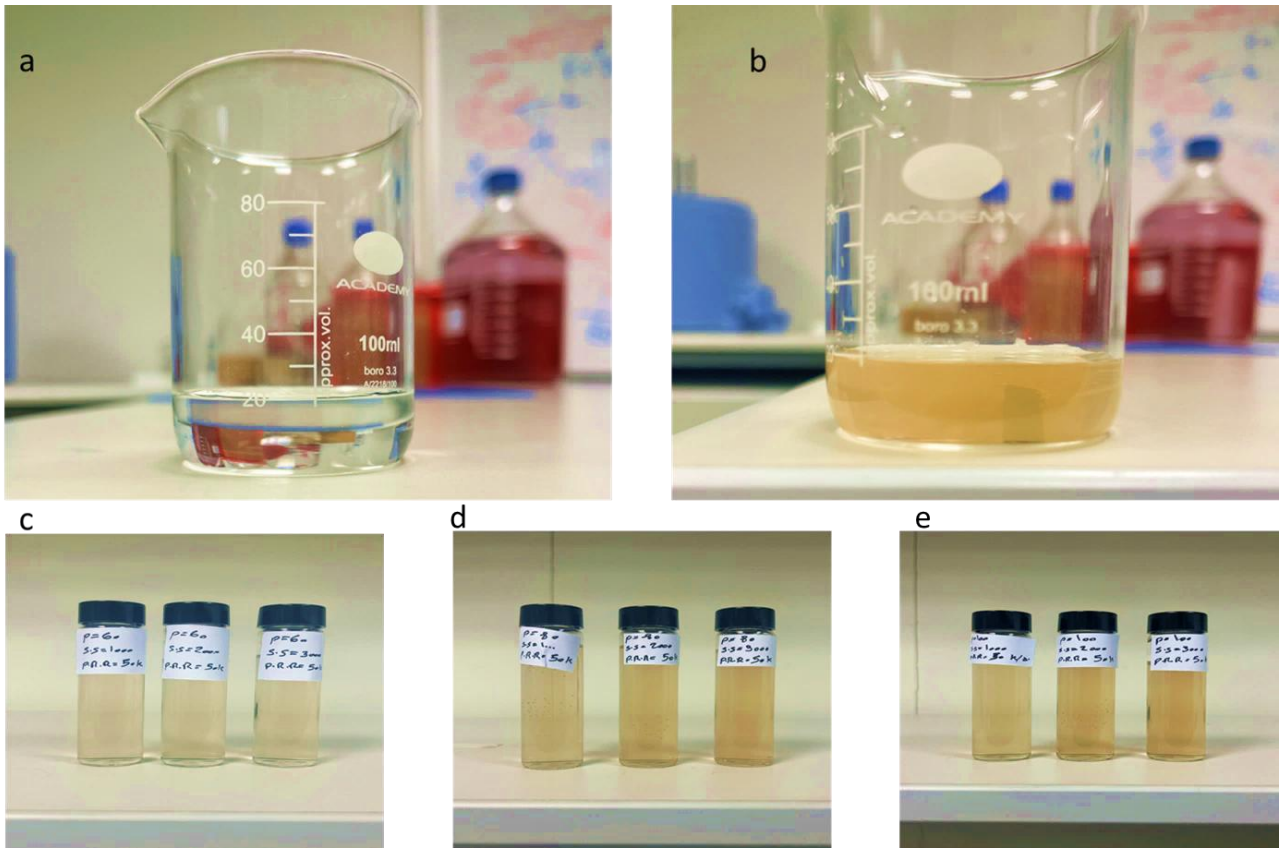
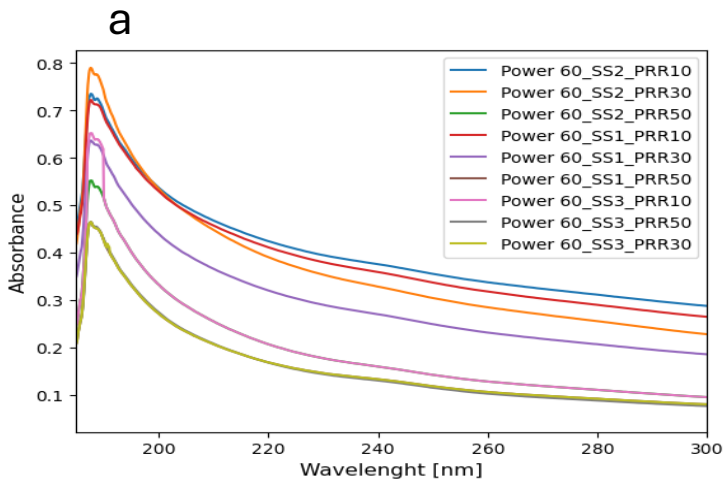


Figure 3.1Photographs of a) DI water with SiC target before PLAL, b) after 5 min PLA; and set of samples produced at a constant PRR of 50 kHz, and scanning speed 1, 2, 3 m/s from left to right respectively for laser powers of c) 60%, d) 80%, and e) 100%.



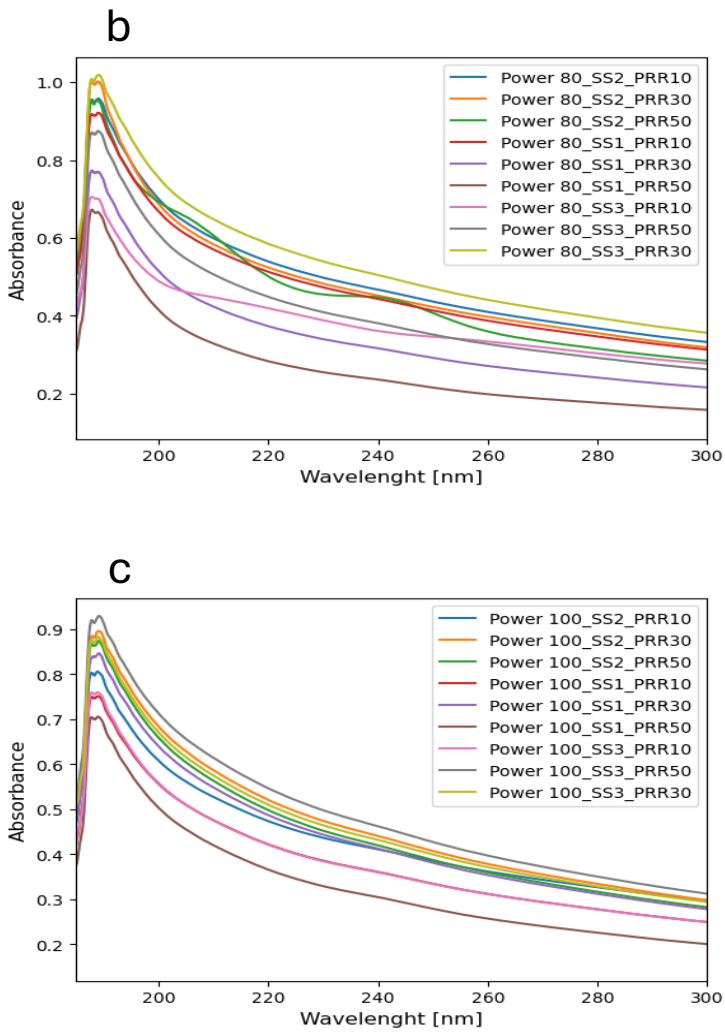


Figure 3.2 UV-Vis for the samples prepared at constant laser power percentages of a) 60, b) 80, and c)100, for the various scanning speeds and PRR.

3.3.2 Dynamic Light Scattering (DLS)

DLS measurements were carried out on the nano colloids produced by PLAL at different scanning speeds, PRR, and laser power percentages to determine the mean size and concentration of the resulting NPs. As shown in Figure 3.3a, b**,** and **c**, the produced NPs mean sizes are categorized based on the laser power percentages. Figure3.3 a, 3.3 b, and 3.3 c show the mean sizes of resulting NPs in constant laser power percentages of 80, 100, and 60 and various PRR and scanning speeds respectively. Generally, as can be observed from Figure 3.3 (a-c), the mean sizes of all resulting NPs are close together and were seen to

be in the range of 89 to 155 nm. However, the mean size of resulting NPs that were produced at the laser power percentage of 60 (Figure 3.3a) is broader compared to those generated at the laser power percentages of 80, and 100 which have a close range of the NPs mean sizes. In Figure 3.4(a-c) the changes in NPs mean sizes with changing the laser parameters are illustrated. In Figure 3.4(a-c) the changes in NPs mean sizes with changing the laser parameters are illustrated. Figure 3.4a shows the changes of NPs mean size with increasing the scanning speed in a constant PRR of 10 kHz and a laser power percentage of 60, 80, and 100. As shown in Figure 3.4a, with increasing the scanning speed from 1 to 3 m/s a unilinear decrease in NPs mean size was observed. It can be associated with the fact that under low scanning speed, the repetitive enhancement and attenuation of the plume shielding effect results in an intermittent ablation process in terms of particle ejection and morphological characteristics. In contrast, at the high scanning speed, the ablation process enters a steady state as the plume shielding effect is circumvented[135]. Figure 3.4b, demonstrates the changes of NPs mean size with changing the PRR in a constant laser power percentage of 60, 80, and 100 respectively, and a scanning speed of 2 m/s. The total trend suggests that increasing the PRR resulted in decreasing the NPs size. Higher repetition rates can lead to increased heating of the target material due to the cumulative effect of multiple laser pulses. This additional heating can influence the size and morphology of the generated nanoparticles. Smaller nanoparticles may form due to increased thermal effects[136]. Furthermore, by increasing the PRR up to 50 kHz the NPs sizes were declined for all the resulting NPs produced in various laser power percentages. Moreover, Figure **4c** shows the changing of the NPs size with changing the laser power percentage in a constant PRR of 10 kHz, and scanning speed of 2 m/s. The NPs size increased with increasing the percentage of laser power, where the size was found 122, 124 and 128 nm for the samples produced at laser power percentage of 60, 80, and 100 respectively. This trend suggests that higher laser power percentages led to bigger NPs being produced. Laser power directly affects the thermodynamic properties of the cavitation bubbles and the produced plasma, which also increases the local concentration of ablated species due to the liquid confinement. An increase in laser power allows the plasma plume to reach a higher temperature and pressure, which results in a longer duration of the cavitation bubbles which would promote the formation of larger-sized particles by

coalescence[137]. This observation could also be attributed to the fact that at the used laser power, a bubble is generated in the liquid, producing discontinuity of the refractive index at the liquid–gas interfaces and consequent high laser light scattering, reducing the laser energy reaching the solid target and decreasing the total amount of NPs generated in the liquid[138]. In addition, as shown in Figure 3.5 **(a-c)** a size range of between 410 to 450 nm was observed in all the samples, which is attributed to the agglomeration of NPs within the colloids. The NPs concentration measurements were carried out and the results are presented in Figure 3.6 (a-c) with changing the laser scanning speed, PRR, and laser power percentage respectively. For all the graphs, two variables were kept constant to determine the effect of changing one parameter on the particle concentration. Based on these results, the concentration of NPs increased from 1.71E+9 to 2.07E+9 particles/ml with increasing PRR from 10 to 50 kHz. An increase from 1.32E+9 to 2.1E+9 particles/ml was found for an increase in laser power percentage from 60 to 100. This observation is in good match with the visual inspection section where increasing the NPs yield was observed with increasing the laser power percentage. On the other hand, increasing the scanning speed resulted in decreasing the NPs concentration from 2.38 to 1.68 particles/ml. The concentration of NPs in a liquid under pulsed laser ablation is influenced by the scanning speed. Generally speaking, a lower scanning speed produces a larger concentration of NPs while a higher scanning speed produces a lower concentration. This is so because the laser beam's residence period on the target material depends on the scanning speed. Higher scanning rates cause the laser pulses to engage with the target material for a shorter period of time, which reduces material ablation and NPs generation. Lower scanning speeds, on the other hand, enable the laser pulses to remain on the target material for a longer period of time, resulting in greater ablation and NPs production[139].

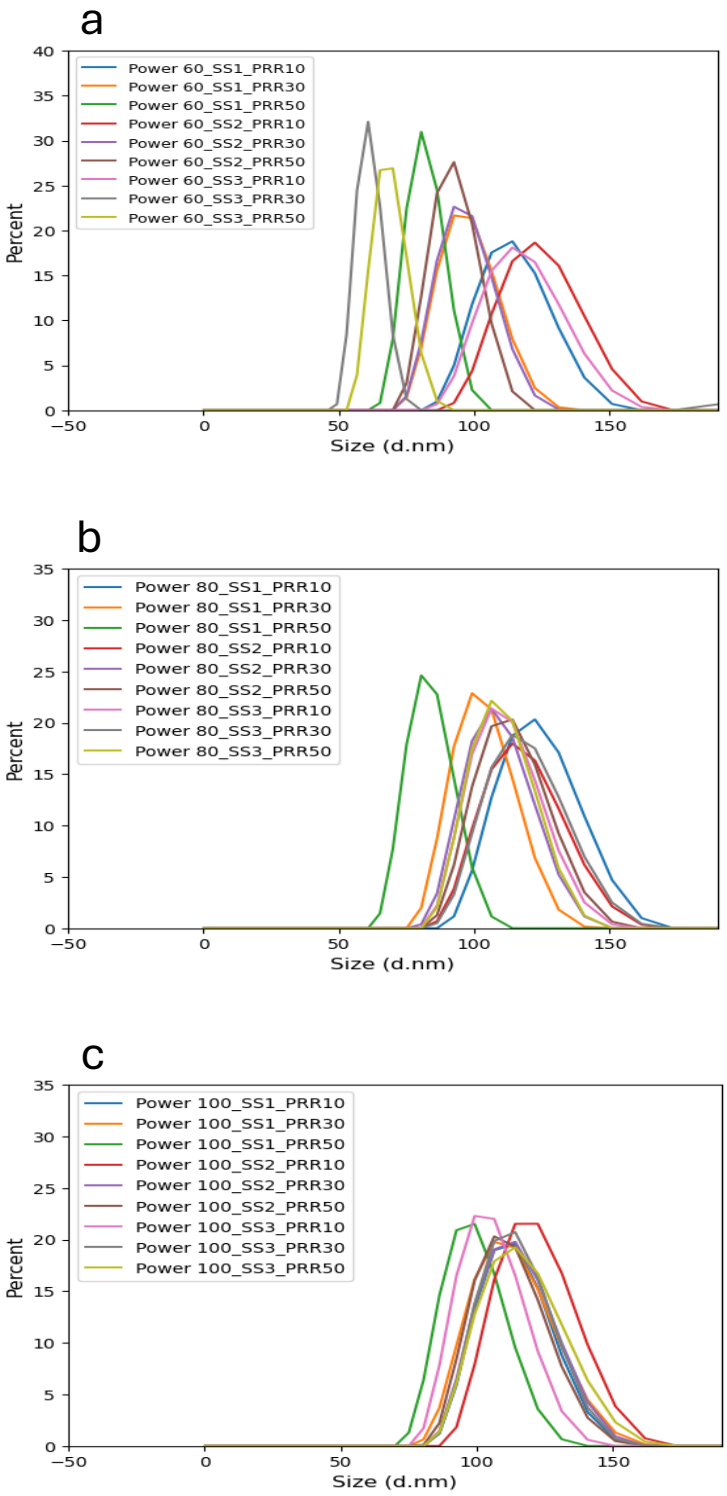
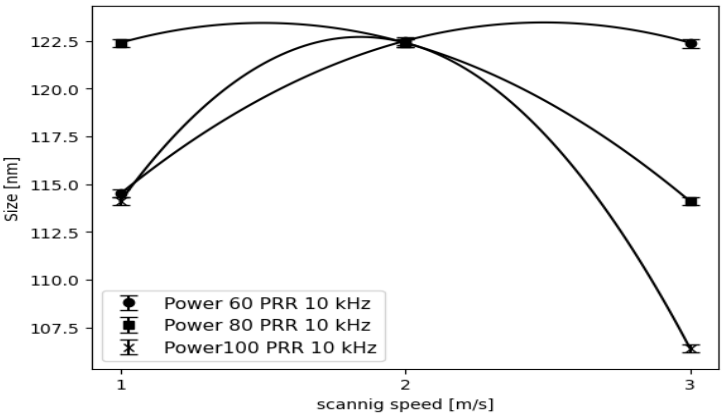
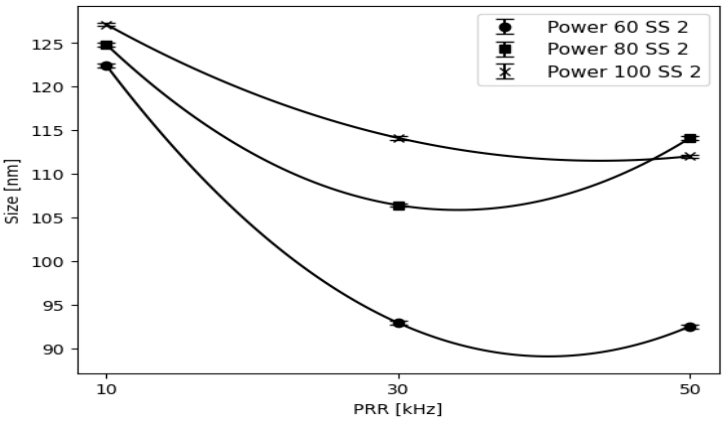


Figure 3.3 Dynamic Light Scattering results for the samples prepared at constant laser power percentages of a) 60, b) 80, and c)100, for the various scanning speeds and PRR.

a


122.5
120.0
117.5
115.0
112.5
110.0
107.5
Size [nm]
Power 60 PRR 10 kHz
Power 80 PRR 10 kHz
Power100 PRR 10 kHz
1
2
3
scannig speed [m/s]

b


Power 60 SS 2
Power 80 SS 2
Power 100 SS 2
125
120
115
110
105
100
95
90
Size [nm]
10
30
50
PRR [kHz]

c

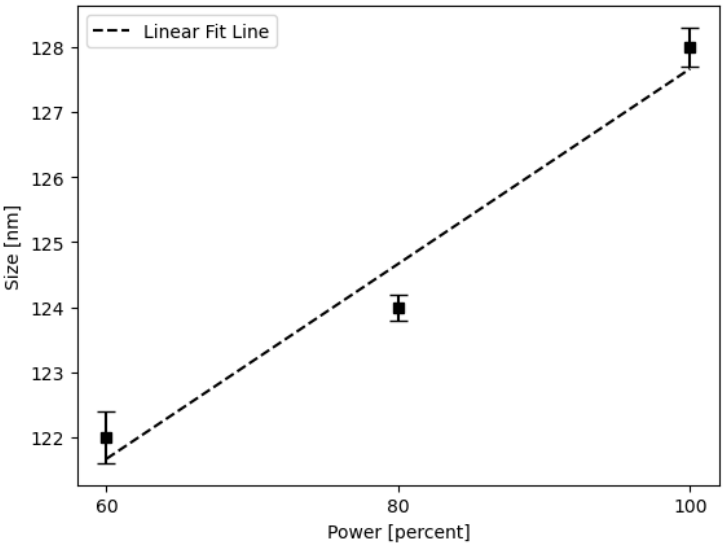
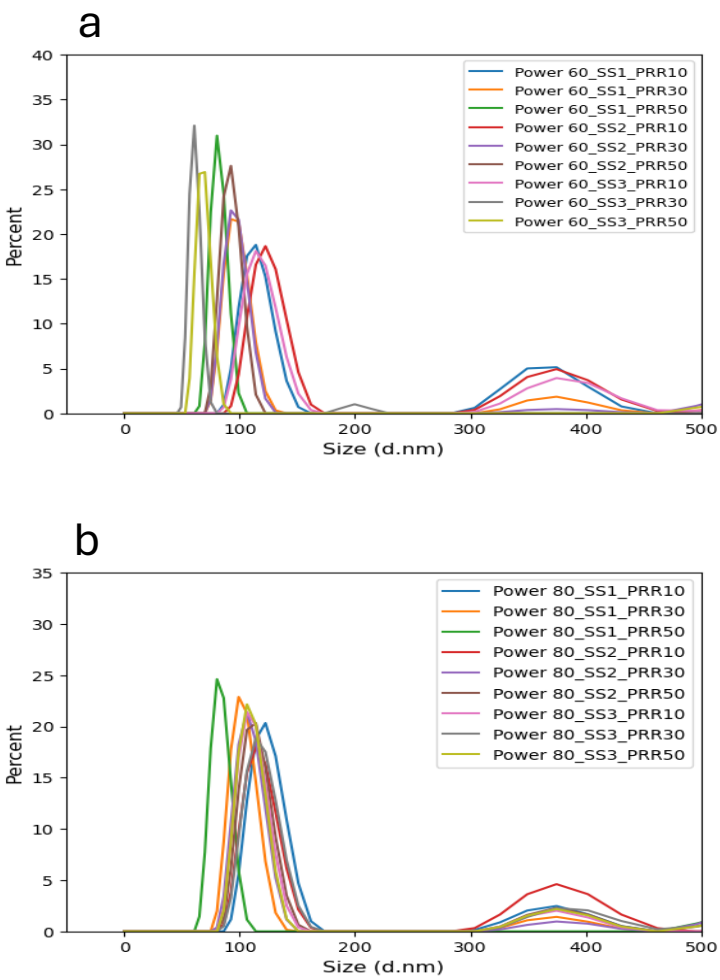

Linear Fit Line
128
127
126
125
124
123
122
Size [nm]
60
80
100
Power [percent]

Figure 3.4 The change in NPs sizes with a) changing scanning speed at a constant PRR of 10, b) PRR in a constant scanning speed of 2 m/s, and c) laser power percentage in a constant scanning speed and PRR of 2 m/s and 10 kHz.



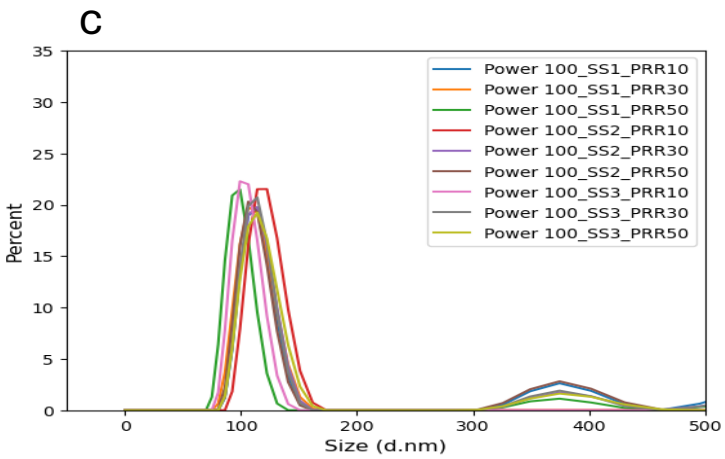
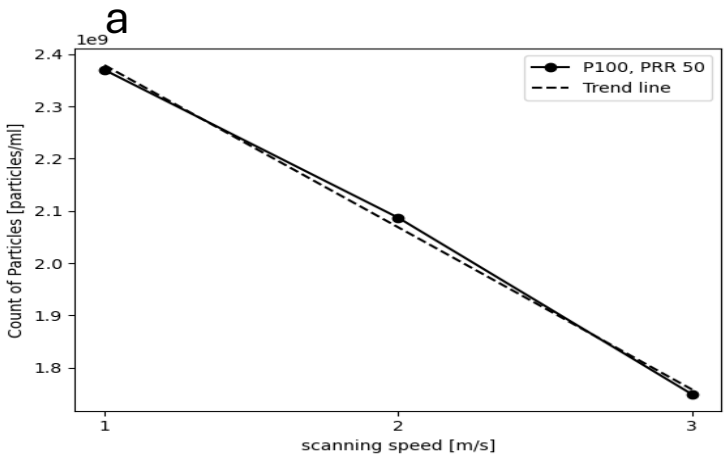
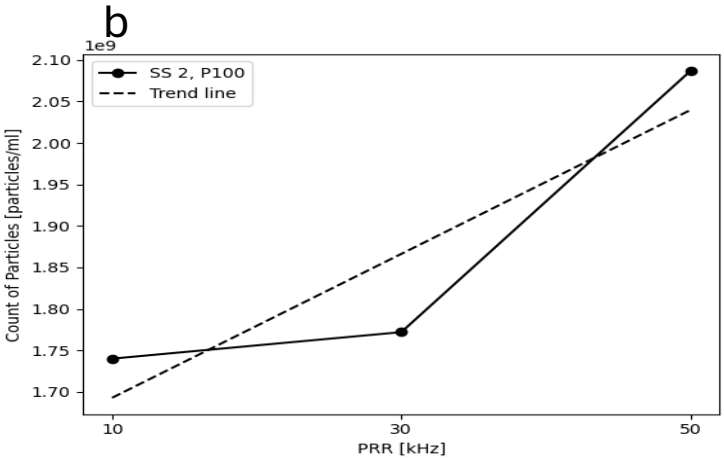


Figure 3.5 Dynamic Light Scattering patterns in the size range up to 450 nm for a set of samples laser power percentages of a) 60, b) 80, and c) 100.



.



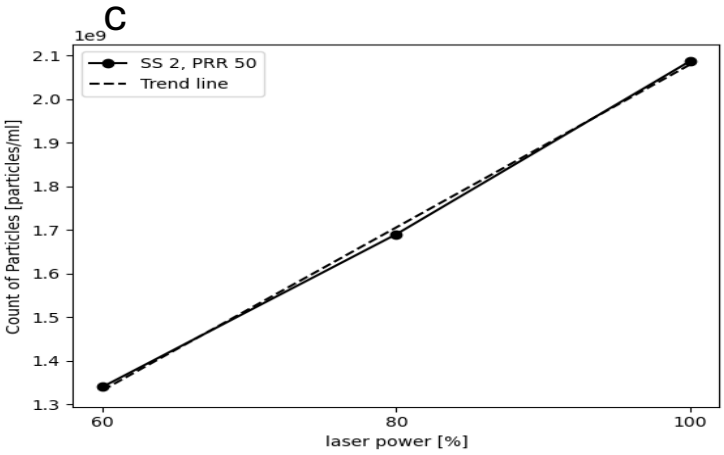


Figure 3.6 The NPs concentration measurements as a function of various laser parameters a) scanning speeds, b) PRR, and c) laser power percentages.

3.3.3 Field emission scanning electron microscopy (FESEM) and scanning transmission electron microscopy (STEM)

FESEM was used to image the resulting NPs shapes and sizes. The as-fabricated colloids were drop-cast on a 400-mesh copper grid and dried with air for 5 min to evaporate the water of the colloid. Figure3. 7 **(a-e)** represents the FESEM images and Figure 3.7 **(f)** shows the bright field STEM of dried SiC NPs in laser power percentage of 60, scanning speed of 2 m/s, and PRR of 10 kHz in different acceleration voltage and magnifications. These figures confirm the formation of spherical and nanosized NPs with some agglomerations and clusters in the STEM image. The dominant mechanism behind nanosecond pulsed laser ablation is the thermal evaporation mechanism in which the laser produces high temperature on the surfaces of larger particles and thereby it gets melted and vaporized into atoms or molecules. These atoms rearrange into smaller nanostructures with the same or different shapes depending on the surrounding medium and laser parameters[140]. As the surrounding medium in this case is DI water all the NPs have the same shape which is a spherical shape. In addition, as can be observed from Figure 3.7 **(a, b, d, f,** and **h)**, the agglomeration in NPs is in good match with DLS results (see Figure 3.5), where a peak was observed in

410 to 450 nm size range.

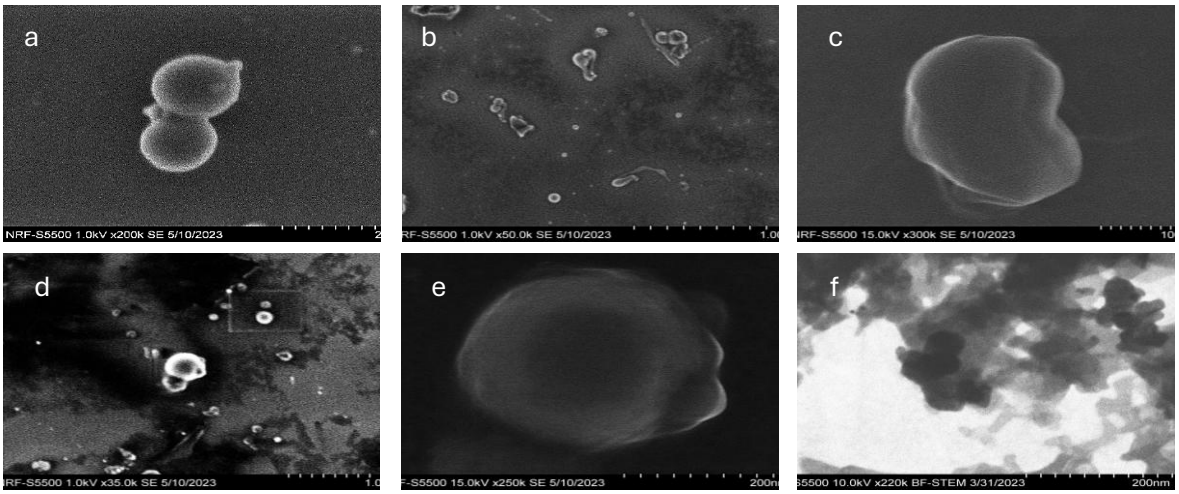


Figure 3.7 FESEM images of produced SiC NPs - a & b & d) SE acceleration voltage 1 kV, e & c) SE acceleration voltage 15 kV, and f) bright field STEM acceleration voltage 10 kV.

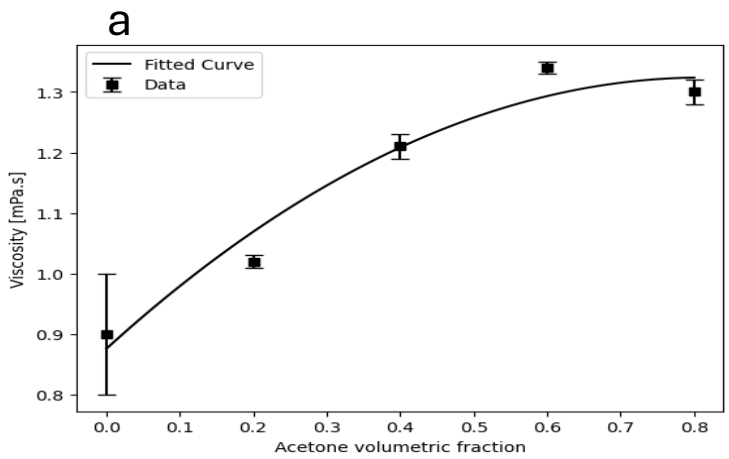
3.3.4 Viscosity Optimization

These NPs without any additives have the potential to be utilized in the production of ink for inkjet printing applications. The ink's fluid properties, including viscosity, particle size, particle concentration, density, and surface tension, are crucial factors during the printing process. To prevent issues like excessive flow or printer head blockage, it is desirable for the ink viscosity to fall within the range of 1-20 mPa.s[133]. In this work, the viscosity of the as-produced SiC NPs was modified in order to meet the criteria of viscosity range for the commercially available inkjet printer by adding various solvents. In this work, three solvents including Acetone, Isopropyl Alcohol (IPA), and Glycerol in various volumetric fractions were mixed with the colloids to tune the viscosity of the bare NPs colloids. The viscosity as a function of solvent volumetric fractions is presented in **Figure 8(a-c)** and **Table 2** for IPA, Glycerol, and Acetone in the final solution respectively. A viscosity range of 0.9 to 1.41 mPa.s was achieved with a maximum viscosity at 0.7 volumetric fraction of Acetone in water (**Figure 8c**), while a maximum viscosity of 10.95 mPa.s was obtained at 0.8

volumetric fraction of Glycerol in water. The IPA-water mixture indicated a viscosity range of 0.9 to 2.34 mPa.s with a maximum viscosity of 2.93 mPa.s at a 0.8 volumetric fraction of acetone-water mixture, which is in good agreement with previous work[133]. Several factors, including the interaction between NPs and the solvent, can cause changes in the viscosity of the liquid. Glycerol, a non-toxic and highly viscous solvent, was used in varying proportions with water to achieve a wide range of viscosity values.

Table 3.2 Viscosity of the colloids using a 0.8 volumetric fraction of acetone, IPA and glycerol.

Solvent	**Viscosity (mPa.s)**
Acetone	0.7
IPA	2.93
Glycerol	10.95



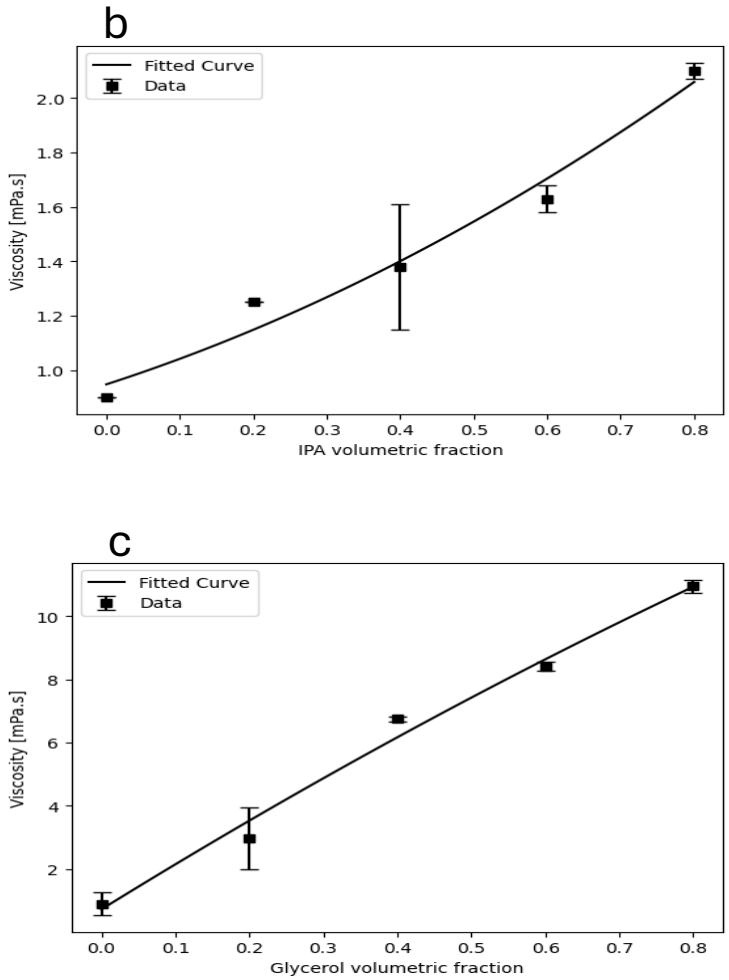


Figure 3.8 Dynamic viscosity measurements at 25 ◦C as function of volumetric concentration of a) Acetone, b) IPA and c) Glycerol.

3.4 Conclusion

This work examined pulsed laser ablation in liquid as a method to obtain high-quality colloids of silicon carbide NPs for inkjet printing applications. The effect of parameters in PLAL including laser power percentage, scanning speed, and pulse repetition rate (PRR) on the properties of resulting NPs such as NPs yield, optical, size and concentration, and morphology were examined and discussed. The results confirmed that increasing the laser power percentage resulted in increasing the NPs yield for all investigated liquids.

Moreover, increasing the laser power percentage resulted in increasing the optical absorption index, which is attributed to increasing the concertation of the NPs within the liquid, also, a peak in the wavelength of 195 nm was observed which is associated with the formation of polyynes. Furthermore, the DLS results revealed the NPs mean size distribution of around 89 to 155 nm for different laser parameters, from which a decrease in NPs mean sizes with increasing the scanning speed and PRR was concluded. The concentration measurement was carried out and the result revealed that, with increasing the PRR and laser power percentage, the concentration of NPs increases. Increasing the scanning speed led to a decrease in concentration. Field Emission Scanning Electron Microscopy (FESEM) was used to determine the morphology and size of the resulting NPs, in which spherical NPs of approximately the same size were obtained. Lastly, viscosity measurements were conducted to tune the viscosity of the colloids for inkjet printing. A volumetric fraction of 0.8 for glycerol-water mixture resulted in the maximum viscosity of 10.95 mPa.s which is suitable for processing with commercial inkjet printers. PLAL for the production of high-purity laser generated NPs colloids with controllable viscosities could be used as a core and affordable technique for SiC colloid production.

4 Chapter 4

Ablation efficiency and properties of SiC NPs synthesised via PLAL

Abstract

This study optimised the synthesis and ablation efficiency of 3C silicon carbide (SiC) NPs using nanosecond pulsed laser ablation in liquid for electronic and biomedical applications. Various process parameters, including laser fluence, scanning speed, and ablation time, were systematically varied to assess their impact on ablation efficiency and NP properties. Statistical analysis identified optimal conditions: a 15-minute ablation time, 0.5 m/s scanning speed, and 7.5 J/cm² laser fluence with the maximum mass productivity of

1.196 mg.h-1W-1. Characterisation techniques, including UV-Vis, Dynamic Light Scattering (DLS), FESEM with EDX, FTSEM, and XRD, confirmed that higher laser fluence, scanning speed, and ablation time increased colloid concentrations without altering NP shape or size. XRD analysis verified the phase composition as 3C SiC, with DLS showing smaller NP sizes than image analysis. The results also suggested that increasing the NP size decreased the optical band gap. A direct correlation was found between ablated mass and colloid concentration.

Keywords: PLAL, Laser synthesis, FESEM, SiC, Nanoparticles, Nd-YAG

4.1 Introduction

Nanomaterials (NMs) exhibit notable properties applicable across a diverse range of sectors, including physics, biology, materials science, chemistry, and engineering[141]. Depending on the NMs size range, they have various unique physical properties including a huge surface-to-volume ratio. The methods of producing NMs can be divided into three main categories: physical, chemical, and biological methods[99]; and two main approaches: top-down and bottom-up [142]. The top-down method reduces the size of bulk material into smaller dimensions, whereas in the bottom-up method, larger-dimension particles are produced from smaller elements such as atoms or molecules[143]. Pulsed laser ablation in liquid (PLAL) is a green method and in the category of the physical and top-down method to produce nanoparticles (NPs) based on the energy of a laser, in which a submerged target in a liquid is ablated by the laser over time[5, 6]. Generation of NPs using PLAL consists of focusing the pulsed laser beam on a bulk material submerged into a liquid medium from which metal NPs, doped nanocrystals, core-shells, hollow microspheres, and nanotubes can be obtained just by changing the laser processing parameters, liquid medium, temperature, and the composition of the bulk target[7, 8]. In recent years the implementation of this method has increased for diverse applications and materials, as it is considered a relatively easy process for producing NPs[4], [6], [7], [8], [120], [121], [122], [123], [146], [147]. PLAL offers several advantages over alternative methods for NPs production. These benefits stem from the cost-effectiveness of the equipment used for atmospheric ablation, the straightforwardness of the method, the elimination of the need for a specialised environment, and the flexibility to modify the properties and morphology of the NPs by adjusting laser parameters and liquid media[13], [126]. One main issue of the PLAL is the productivity of the method. This issue has led researchers to try to increase the productivity of the method for different materials. For instance, Freeland et al. showed the possibility of increasing the productivity of the PLAL by using a dynamic liquid flow and decreasing the pressure inside the chamber for silicon NPs[148]. However, using dynamic mode increases the cost of the mass production of the NPs. So, increasing the productivity of the NPs in static mode requires more work as a cost-effective and straightforward method of NPs fabrication.

Furthermore, the utilisation of ultra-high scanning speeds and pulse repetition rates has been demonstrated to augment the productivity of PLAL to as much as 4 g h^{-1} for platinum and gold nanoparticles. Nevertheless, the adoption of these ultra-fast scanning speeds and elevated repetition rates remains challenging, rendering the procedure prohibitively expensive[139].On the other hand, increasing the productivity of silicon carbide (SiC) NPs as a potential candidate for electronics, high-temperature applications and abrasives remains a gap in this field. SiC presents a promising prospect as a wide-bandgap semiconducting material, surpassing the performance of their monometallic counterparts. SiC boast advantageous properties, including a high breakdown field strength, excellent chemical stability, lower thermal conductivity compared to metals, remarkable resistance to oxidation and corrosion, and elevated hardness[21–23]. SiC nanoparticles have found extensive applications in a range of high-temperature and high-frequency scenarios, including light-emitting diodes and UV detectors[125], [149], [150], [151]Moreover, the low thermal expansion coefficient of SiC further enhances its suitability as a raw material for advanced refractories, functional ceramics, and abrasives. This underscores its versatility in a wide range of industrial applications[15], [152]. Depending on the phases of the SiC, the properties of the material will be different. For instance, cubic phase (3C SiC, also known as β-SiC) was reported to be served in electronic and biomedical applications[153]. However, the hexagonal phase (4H and 6H) was used mostly in power diodes[154]. Among top-down methods, high-energy ball milling has traditionally been employed for the fabrication of nano-sized silicon carbide. However, the considerable time and energy requirements, coupled with challenges in mitigating impurities introduced by the milling balls, render this conventional method impractical for certain applications [155].There are also other methods to produce SiC NPs such as chemical synthesis, chemical etching, electrochemical etching, electrochemical etching, and liquid phase reaction [156], and relatively new methods such as PLAL. For instance, Castelleto and coworkers [16] fabricated SiC NPs using ultra-short pulsed laser ablation and studied the resulting NPs for biomedical imaging applications where the structural, optical, sizes and morphologies were studied. Yamada et al. [17] studied the resulting sizes, shapes and crystal structure of produced SiC NPs in acetone using a picosecond laser. A femtosecond pulsed laser was also used by Guo et al. [129] to produce SiC NPs

in DI water with the resulting NP optical properties and shapes studied. Moreover, a picosecond pulsed laser was used to micromachine SiC wafers in non-thermal mode and ablation depth, thermal effects and mechanism for micromachining were studied[131]. Moreover, SiC nanoparticles, both amorphous and crystalline, were produced through laser ablation of micro-sized SiC powder in water and ethanol. Analysis using X-ray and HRTM revealed the amorphous nature of SiC nanoparticles, averaging 44 nm in water, and crystalline SiC polytype nanoparticles, averaging 18 nm in ethanol[130]. The SiC NPs also were synthesised using a 532 nm laser to ablate the silicon wafer in ethanol, where the possibility of obtaining the SiC without any catalyst was investigated [126] Only a few articles have been published on the fabrication of SiC NPs via PLAL [126], [131]. While studies have explored the fabrication of SiC NPs utilising different laser energy sources, there remains a notable gap in the literature concerning the investigation of the productivity of the SiC NPs fabrication using static mode PLAL. This study adopts a systematic approach to investigate the ablation efficiency and the influence of varying laser fluences, scanning speeds, and ablation times on the resulting SiC NPs in batch mode to reduce the cost of the mass production of this material. This work also introduces the 3C SiC NPs as a potential candidate in high-temperature, biomedical and electronic applications. Furthermore, in this study, we present a novel investigation into the ablation efficiency of SiC NPs in batch mode, the first exploration of its kind for this material. Our findings not only advance the synthesis and characterisation of SiC NPs in relation to laser processing parameters but also establish a crucial correlation between ablation efficiency and these parameters. This optimisation offers valuable insights for scaling up the process using the batch method of PLAL, providing a foundational guide for researchers in this field.

4.2 Experimental and Design of Experiment

4.2.1 NPs synthesis

In this study, the effect of laser fluence (J/cm²), scanning speed (m/s), and ablation time (minutes) on the fabrication of SiC NPs from a rod target (99.9% purity, a diameter of 5.0mm, and reaction bonded supplied from Goodfellow) were investigated. The target was polished (using a 2000 grit size polishing paper) before each laser ablation process and placed vertically into a 100 ml glass beaker so that a 5 mm distance was maintained between the surface of the target and water. A 3 × 3 full factorial design of the experiment was created using Design-Expert software, where three different laser fluences of 3.78, 6.52, and 7.5 J/cm², scanning speeds of 0.1, 0.3, and 0.5, and ablation times of 5, 10, and 15 minutes were investigated. Table 4.1 shows the fabrication conditions applied for each sample. The pulse width, laser spot size, and liquid media were kept constant at 0.6 ns, 50μm, and deionized water, respectively. Ablations were performed using a Nd:YAG laser system (WEDGE HF 1064, Bright Solutions) with pulses centred at 1064 nm with a pulse repetition rate of 10 kHz. An Archimedean spiral pattern scanning strategy was used to ablate the target, where a 2 mm outer diameter and a hatch spacing of 50 μm were chosen to focus the laser spot on the centre of the rod.

Table 4.1 Design of Experiment for all the samples and their assigned sample names

Sample Name	**Laser Fluence (J/cm2)**	**Scanning Speed (m/s)**	**Ablation Time (minutes)**
S1	3.78	0.1	5
S2	3.78	0.1	10
S3	3.78	0.1	15
S4	3.78	0.3	5
S5	3.78	0.3	10

S6	3.78	0.3	15
S7	3.78	0.5	5
S8	3.78	0.5	10
S9	3.78	0.5	15
S10	6.52	0.1	5
S11	6.52	0.1	10
S12	6.52	0.1	15
S13	6.52	0.3	5
S14	6.52	0.3	10
S15	6.52	0.3	15
S16	6.52	0.5	5
S17	6.52	0.5	10
S18	6.52	0.5	15
S19	7.5	0.1	5
S20	7.5	0.1	10
S21	7.5	0.1	15
S22	7.5	0.3	5
S23	7.5	0.3	10
S24	7.5	0.3	15
S25	7.5	0.5	5
S26	7.5	0.5	10
S27	7.5	0.5	15

4.2.2 NPs characterisation

UV-Vis spectroscopy measurements were conducted to assess the absorbance of SiC NPs as an indicator of NP yield. The Ultrospec 7500 Spectrophotometer and a Biochrom UV-Vis spectrometer with a quartz cuvette (Helma, 10 mm path length) were utilised, scanning in the range of 190 to 500 nm. To eliminate the influence of the liquid medium's absorption, optical spectra were adjusted by subtracting its contribution from the recorded spectrum. The size, zeta potential, and concentration of NPs (particles/ml) were determined using Dynamic Light Scattering (DLS) on the Malvern Zetasizer Ultra. Field Emission Scanning Electron Microscopy (FESEM) was performed using the Hitachi S5500 instrument. For SEM analysis, a 0.1 µl SiC colloid was drop-cast onto a 400-mesh size copper grid (Agar Scientific), and the sample was air-pumped for 2 minutes to remove colloidal water before examination. Energy Dispersive X-ray Analysis (EDAX) was utilised with the FESEM system to explore the composition of the colloid drop and map its constituents. Ablation efficiency was determined by measuring the target's weight before and after each ablation process, with three measurements averaged for accuracy. Careful drying of the target was performed to exclude water weight, ensuring the precise measurement of the target's actual weight. X-ray Diffraction (XRD) was used (model STOE STADI P with the detector MYTHEN DSC4) to determine the crystallographic structure of the resulting NPs. A Molybdenum Kα1 X-ray source in transmission mode with a step size of 0.016 degrees and diffraction angle of 4 to 50 degrees was used to analyse the resulting NPs. Moreover, the Malvern Panalytical Empyrean high-energy diffractometer with the same step size, diffraction angle, and X-ray source was used to investigate the crystallographic structure of the target material. The particle sizes in FESEM images were carried out using the Image Analysis software ImageJ. In this method, although there is agglomeration present in the image. In this case, only the non-agglomerated particles were considered for the particle size calculation.

4.2.3 Statistical analysis

The assessment of statistical significance was modelled using Design Expert software, which relies on P-values, where a level of significance of P-value < 0.05 is commonly employed. A P-value below 0.05 is typically considered to be statically significant, whereas a P-value greater than 0.05 means that it is not statistically significant. Additionally, the F-value was used in the regression analysis to assess the significance of the results. R-squared (R^2) was calculated for the results, with values ranging from 0 to 1; higher values indicate a better match between the model-predicted result and the actual result. The signal-to-noise ratio was calculated using Adequate Precision which compares the range of the predicted values at the design points to the average prediction error. Ratios greater than 4 indicate adequate model discrimination. Equation 1 shows the calculation method for the signal-to-noise ratio, where $\hat{Y}$ are the predictions at the run settings, $p\hat{o}^2$ is the residual mean square from the ANOVA table, p is the number of terms in the model, and n is the number of runs in the design. The variables used for this experiment as independent factors were laser fluence (J/cm^2), scanning speed (m/s), and the duration of the ablation (minutes). The productivity of the ablated mass was the key response investigated in the model. In total, 27 experimental runs were conducted to comprehensively explore the interactions among these factors and their impact on PLAL ablated mass productivity. The response surface method was modelled using Design Expert (Stat-Ease Inc.) software, specifically employing a quadratic 2-factor interaction (2-FI) process order, which was determined to be the most suitable fit for this study among the various models considered.

$$4 < \frac{max(\hat{Y}) - min(\hat{Y})}{\sqrt{V_{\hat{Y}}}}$$

$$V_{\hat{Y}} = \frac{p\hat{o}^2}{n}$$

Equation 1.

4.3 Results and Discussion

4.3.1 Optimisation of the PLAL for high-yield SiC NPs fabrication

Table 4.2 shows the analysis of variance (ANOVA) calculated F-value, P-value**,** R^2, Adj- R^2, and Pred- R^2 values. According to the data presented in Table 4.2, the P-value of the linear model is less than 0.0001, significantly lower than the customary threshold of 0.05. This result signifies the statistical significance of the model, indicating that the terms within the model exert a substantial influence on the response variable. This conclusion is corroborated by the high R^2 value, which indicates that 93.38% of the data's variation is accounted for by the model. Furthermore, the model's robustness is evidenced by the close agreement between the Adj- R^2 value of 0.8860 and the Pred- R^2 value of 0.6486. The adequacy precision, reflecting the signal-to-noise ratio, is notably high at 17.44, indicating a strong signal in the data. The standard deviation of the model was also calculated and found to be 0.15, which highlights the significance of the model accuracy. This suggests that the DoE model is suitable for predicting outcomes within the chosen range of variables. The study includes 3-dimensional (3D) response surface plots (Figure 4.1**,** panels a-d) generated using the ANOVA table, providing insights into the relationship between each independent variable and the ablated mass. Plot 4.**1d** also demonstrates the model's accuracy in predicting ablated mass when compared to actual values. In Figures 4.1(a-c)**,** it is apparent that the optimal conditions for maximising SiC NPs ablated mass are achieved at a laser fluence of 7.5 J/cm2, a scanning speed of 0.5 m/s, and an ablation time of 15 minutes, resulting in an ablation productivity of 1.9 mg in 10 ml of deionized (DI) water. Ablation productivity was quantified by measuring the target's weight before and after each ablation process.

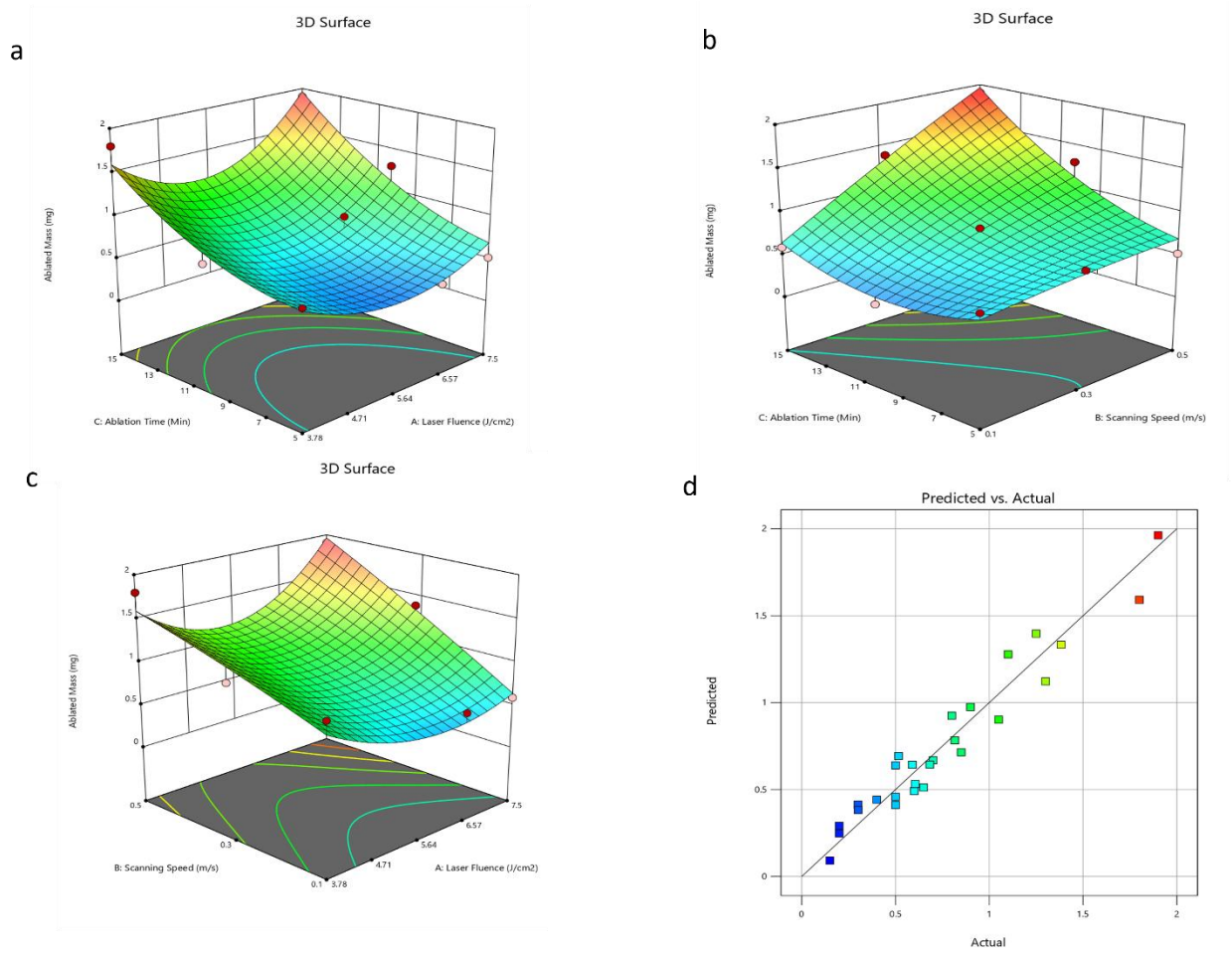


Figure 4.1Response-surface graphs show the outcome of the ablation time, scanning speed, and laser fluence on the yield of SiC NPs in DI water. Response surface plot of SiC NP productivity as a function of a) scanning speed, b) laser fluence, c) ablation time and d) predicted vs actual graph

Table 4.2 ANOVA analysis for a quadratic fit of the data

Model	**F-Value**	**P-Value**	**R^2**	**Adj-R^2**	**Pred-R^2**
Linear	22.26	<0.0001	0.9338	0.8860	0.6486
Square root	15.23	<0.0001	0.9289	0.8679	0.6398
Natural Log	11.93	<0.0001	0.9109	0.8346	0.5969
Inverse square root	9.49	<0.0001	0.8905	0.7967	0.5341

4.3.2 Effect of ablation time on the properties of resulting NPs

In the context of this research study, a comprehensive investigation was conducted, involving the application of three distinct ablation durations: 5, 10, and 15 minutes. The primary objective was to examine the influence of each respective ablation time on various crucial characteristics of the resulting NPs. The investigation encompassed an analysis of optical absorption, particle mean size, concentration, and morphology. The samples generated from the ablation processes were designated as S1, S2, and S3 which corresponded to the ablation durations of 5, 10, and 15 minutes, respectively. It is noteworthy that all samples were generated employing a consistent scanning speed of 0.1 m/s and a laser fluence of 3.78 J/cm^2. Figure 4.2 illustrates the UV-Vis spectra obtained for the samples S1, S2, and S3 and the inset images show the corresponding fabricated samples. Based on Figure 4.2, by increasing the ablation time from 5 to 15 minutes the NPs optical absorption index increased accompanied by a peak at nearly 250 nm for all samples. This observation is attributed to increasing the NPs yield across the liquid medium which resulted in higher optical absorption in the spectra [126]. In addition, visual inspection of the fabricated samples clearly shows a transition from almost colourless to grey for samples S1 to S3 respectively, which confirms the yield increase of the NPs. In nanosecond PLAL, rapid heating of the target occurs, and subsequent plasma formation happens. This plasma reaches a high temperature and high pressure [116] and transfers its energy to the liquid with its collapsing [157], which leads to the vaporisation of the liquid medium and the formation of cavitation bubbles. Then NPs nucleation and growth occur within the cavitation bubbles in the later stages at around 10^{-6} to 10^{-4} seconds until it collapses and NPs are released into a liquid medium. The observed correlation between ablation time and NPs yield can be attributed to the mechanics of this process. Prolonged ablation times within the context of a constant laser fluence and scanning speed facilitate a more pronounced formation and subsequent collapse of cavitation bubbles [158]. Consequently, a greater quantity of NPs is liberated into the surrounding liquid medium. This mechanism is inherently responsible

for the observed escalation in nanoparticle yield, a phenomenon that aligns harmoniously with the observed rise in optical absorption. Moreover, Figure 4.3 shows the EDX result obtained from the resulting NPs in which the elements present in the NPs were indicated. As obvious from Figure 4.3**,** carbon, oxygen and silicon are the most dominant elements in the NPs followed by a small amount of copper. The elemental composition distribution images clearly confirm that the NPs observed consist of carbon, silicon and some oxygen. The presence of oxygen in the recorded EDX result is attributed to silicon oxidation during laser irradiation or due to oxygen molecules adsorbed in the SiC particle surface [19]. There are amount of copper recorded in the EDX results which comes from the copper grid used for the FESEM. The XRD pattern for the target material and the resulting NPs are presented in Figure 4.4. Based on the result obtained using the XRD, the produced SiC NPs have the same crystallographic structure as the target material. The indexed XRD pattern of SiC target material and resulting NPs indicates that they have a cubic phase (3C-SiC) with the lattice parameter of a= 4.358 Å (Card No.96-101-1032, JCPDS card no. 29-1129; a = 4.359 Å). The peaks at 2θ = 29.14, and 21.35 are also present in the XRD patterns which are related to the formation of the SiO_2 phase in the produced NPs[159], [160]. The micrographs of FESEM, BF-STEM, and size distribution for the samples S1, S2, and S3 are portrayed in Figure 4.5 (a-k) respectively. These graphs indicated that the resulting NPs were spherical so changing the ablation time did not change the NPs shapes. Image analysis was executed to ascertain the dimensions of the NPs, as depicted in Figure 4.5 (subfigure **c, f,** and **k**). Notably, the measurements obtained through image analysis yielded NPs sizes notably smaller than those determined through DLS (Table 4.3). This intriguing discrepancy has been previously documented in detail in the work of reference [161]. In the aforementioned study, the observed size differentiation was attributed to the different mechanisms involved in both FESEM image analysis and DLS techniques. Figure 4.6 illustrates the total ablation mass of the target in different ablation times of 5 to 15 minutes in a constant laser fluence and scanning speed of 3.78 J/cm^2 and 0.1 m/s. Overall, by increasing the ablation time from 5 to 15 minutes, an increase in the ablated mass from 0.3 to 0.6 mg was observed. The observed trend in Figure 4.6 suggests that ablated mass increased exponentially with increasing the ablation time. more NPs could be fabricated in higher ablation times, which was previously reported for

other elemental NPs in both gas and liquid environments [162], [163], [164], [165]. Moreover, the mass productivity which is dependent on the laser power was measured and mass productivity reached a maximum level of 0.398 $mgh^{-1}W^{-1}$ once the ablation time increased to 15 minutes. On the other hand, the concentration of the NPs is a different term compared to NPs yield. NPs yield refers to the total quantity of NPs produced, while concentration measures the density of NPs in a given volume of liquid. The concentration and the average size of the resulting NPs were evaluated using DLS, and the outcomes are displayed in Figure 4.7. The resulting NPs mean sizes are shown in Table 4.3, in which the change of the NPs mean size is not significant. Furthermore, the concentration of the resulting NPs exhibited an upward trend when the ablation time was extended from 5 to 10 minutes. However, this trend reversed when the ablation time was further increased to 15 minutes. This observation implies that prolonging the ablation time up to 15 minutes introduces a change in the dynamics. The laser's interaction with the NPs already formed in the liquid medium seems to play two roles, first leading to a reduction in the laser energy reaching the target and second, further breaking down the already fabricated NPs into smaller pieces [164]. Consequently, as the ablation time further increases to 15 minutes, the formation of cavitation bubbles is hindered, resulting in a decrease in nanoparticle concentration and decreasing the NPs mean size with further breaking down the already formed NPs. This process is caused by the laser shielding effect and is known as laser fragmentation in liquid (LFL). Moreover, Figure 8 displays the zeta potential measurement of the samples S1, S2, and S3. The zeta potential decreased from -17.432 to -10.97 mV by increasing the ablation time from 5 to 15 minutes. Based on the results obtained the zeta potential decreased by increasing the ablation time, so the colloidal stability of the samples that were fabricated in higher ablation time is higher.

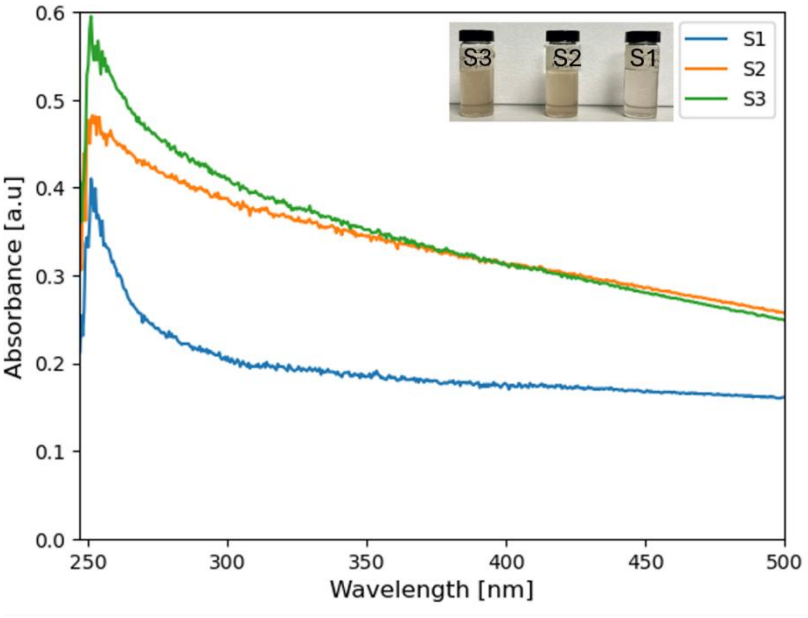


Figure 4.2 UV-Vis spectra for the samples S1, S2, and S3 in a constant laser fluence of 3.78 J/cm2, scanning speed of 0.1 m/s and ablation time of 5, 10, and 15 minutes respectively; the inset image shows the visual inspection of the corresponding samples

Table 4.3 The NPs mean size at the three different laser ablation times

Ablation Time (min) sample name	DLS NPs Mean Sizes (nm)	STEM NPs mean size (nm)
5 S1	146	119
10 S2	147	123
15 S3	143	120

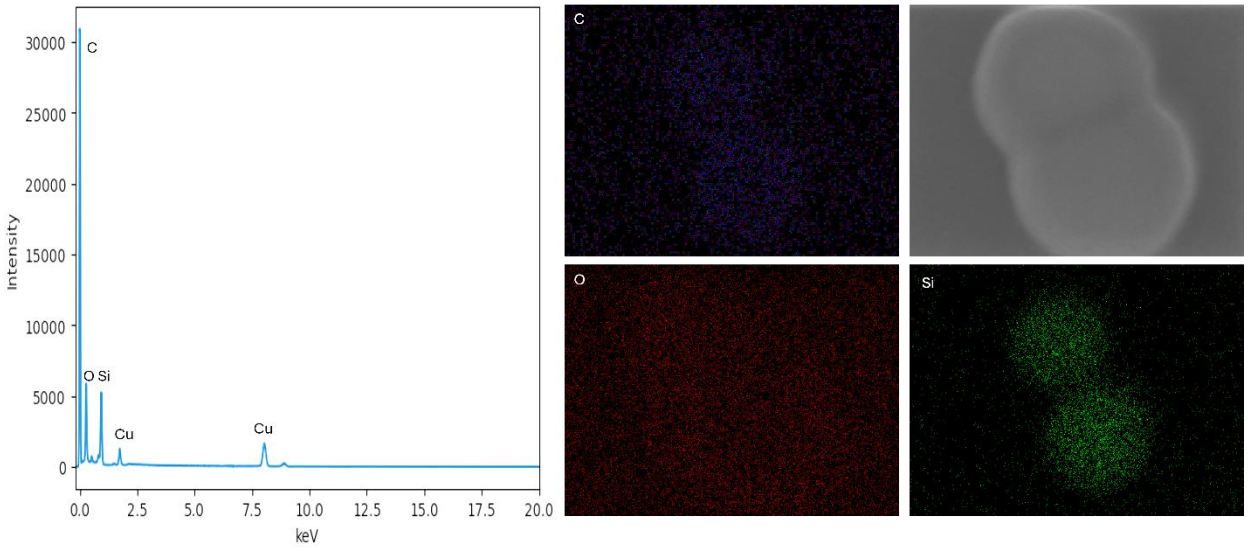


Figure 4.3 EDX keV response, SEM image of NP, and colour maps of the measured Si, O, and C concentrations for the sample S3

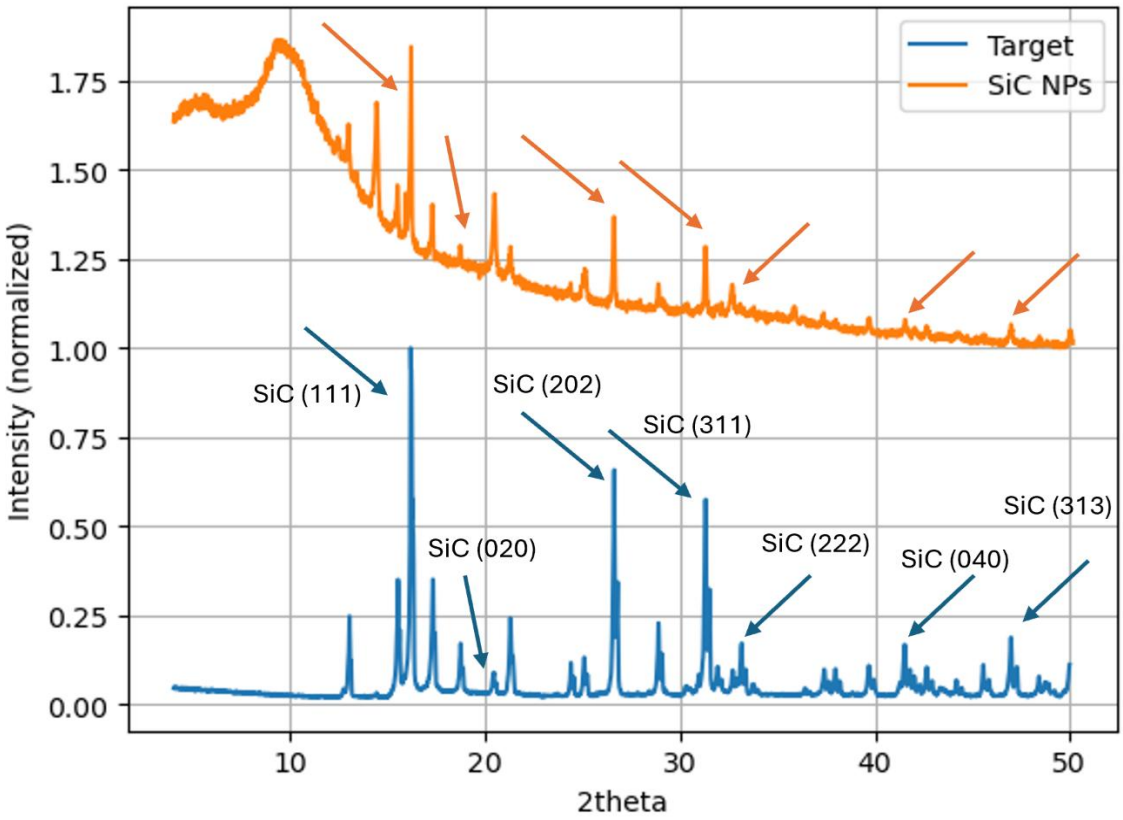


Figure 4.4 XRD patterns of the target material and produced NPs

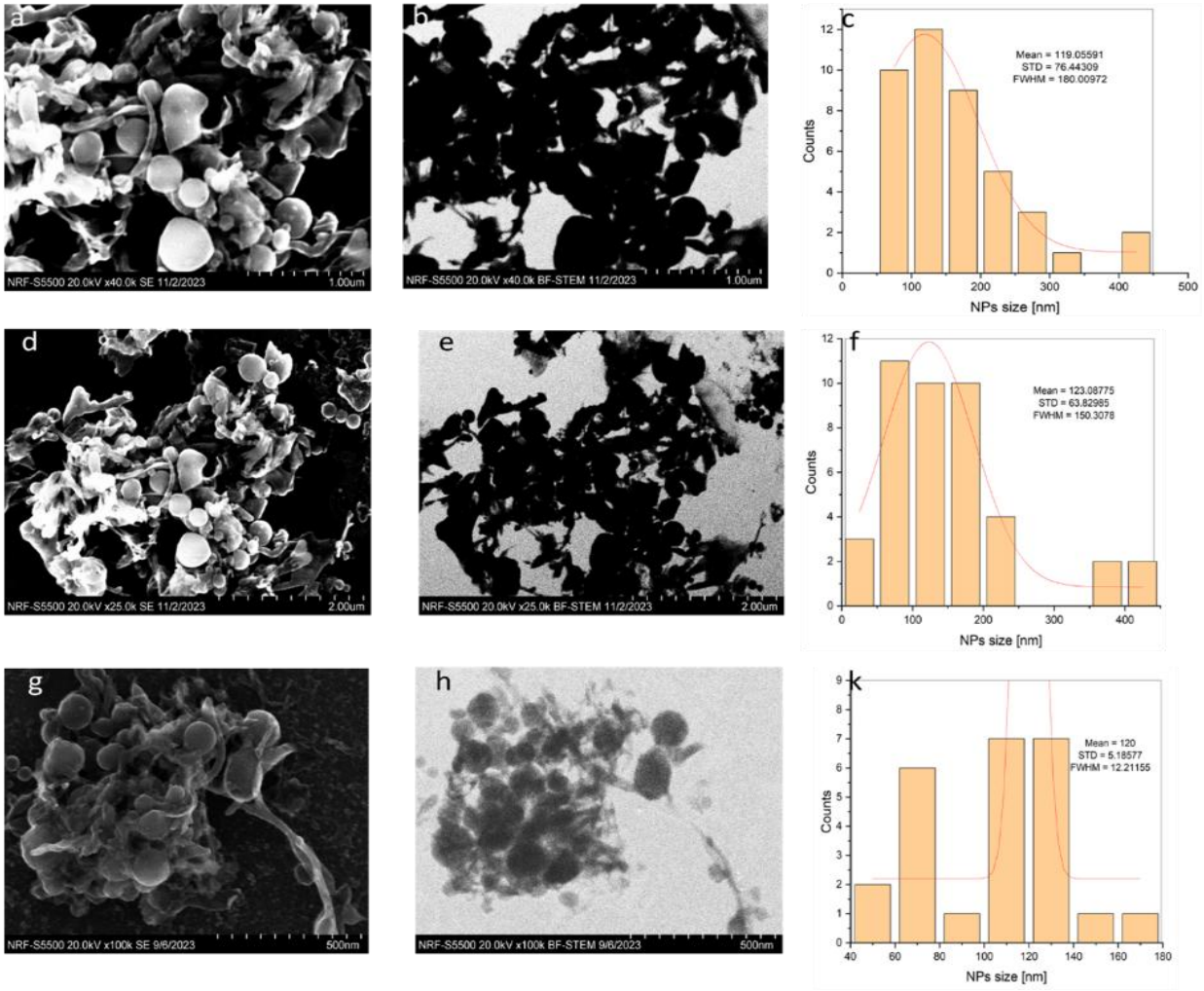


Figure 4.5 Micrographs FESEM, BF-STEM and size distribution of a, b, and c of the sample S1. d, e, and f for the sample S2, and g, h, and k for the sample S3

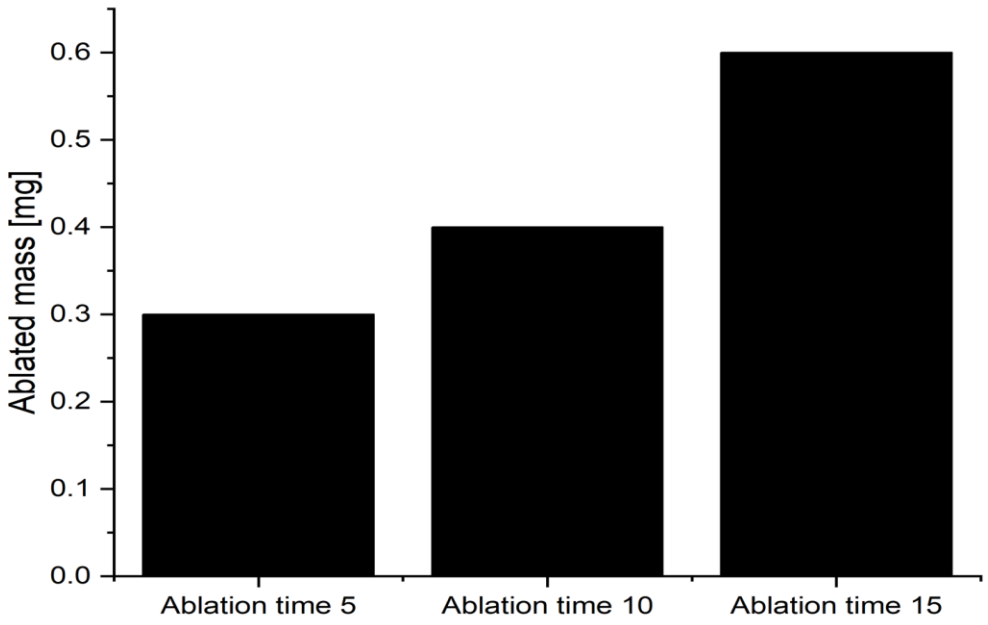


Figure 4.6 Actual ablated mass [mg] for a constant laser fluence of 3.78 J/cm2, a scanning speed of 0.1 m/s, and ablation times of 5, 10, and 15 minutes

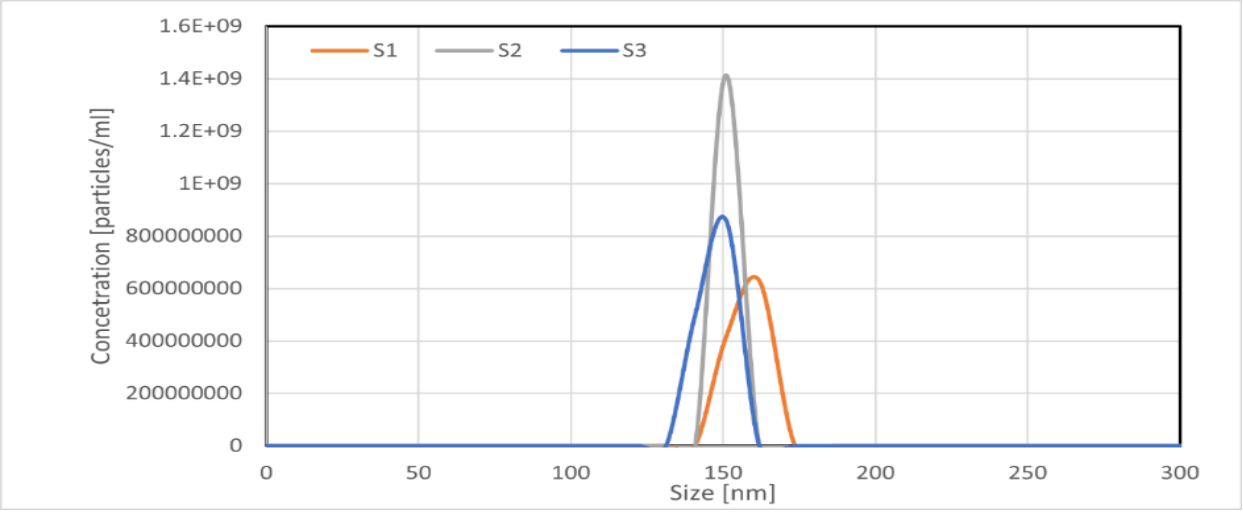


Figure 4.7 DLS results for the samples S1, S2, and S3 in a constant laser fluence of 3.78 J/cm2, scanning speed of 0.1 m/s and ablation times of 5, 10, and 15 minutes, respectively

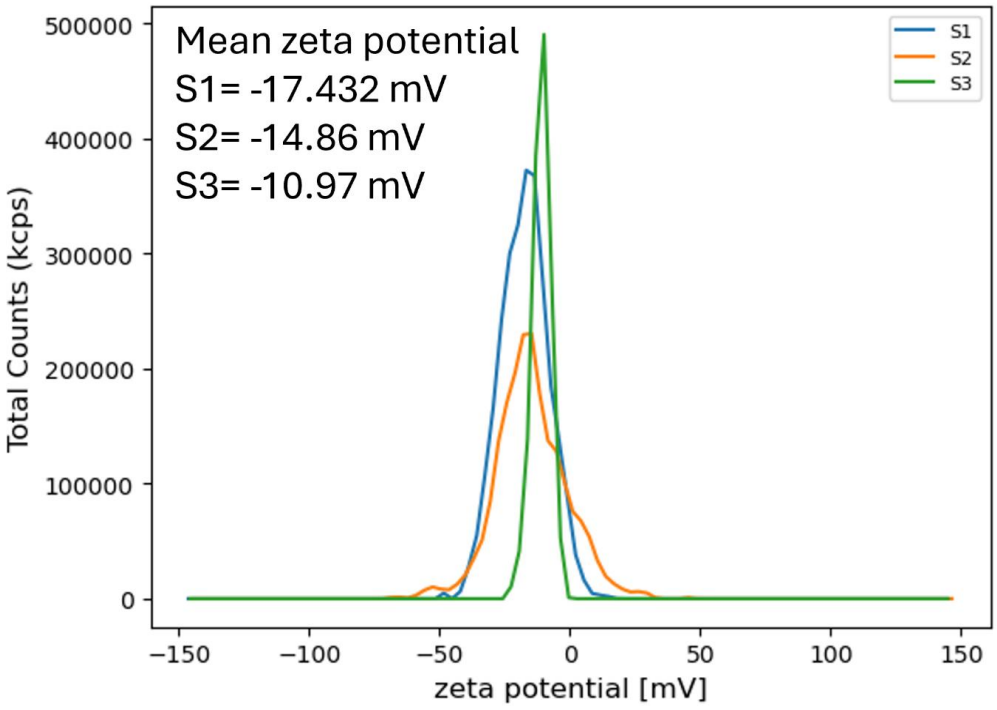


Figure 4.8 Zeta potential measurement of the samples S1, S2, S3.

4.3.3 Effect of scanning speed on the resulting NPs

This section examines the influence of different scanning speeds on the properties of the resulting SiC NPs. Throughout the results which are presented in this section, the laser fluence and ablation time were held constant at 3.78 J/cm² and 15 minutes, respectively. The generated samples were designated as S3, S6, and S9, corresponding to scanning speeds of 0.1 m/s, 0.3 m/s, and 0.5 m/s, while maintaining a consistent laser fluence and ablation time for each respective sample. The UV-Vis spectroscopy with a wavelength range of 240 to 500 nm was conducted for the samples S3, S6, and S9 and the results are shown in Figure 4.9. Generally, the patterns indicated that the optical absorption index of the NPs increased with increasing scanning speed up to 0.5 m/s, following a peak at around 250 nm for all the samples. Beyond this peak, a

subsequent decline in optical absorption was evident. This decline occurred linearly and tended towards saturation as the wavelength was further extended, up to the limit of 500 nm. In essence, the optical absorption behaviour of the nanoparticles exhibited a nuanced response to the varying scanning speeds, characterised by distinct absorption patterns across the specified wavelength range. The inset image in Figure 4.9 illustrates the corresponding S3, S6, and S9 samples. As is evident from the inset image, increasing the scanning speed causes an increase in NPs yield as a shift in colour can be seen from light grey to brown for the samples S3 to S9. The observed increase in the optical absorption index with higher scanning speeds is attributed to the concurrent increase in nanoparticles yield. This connection becomes evident upon visual inspection of the results. As scanning speed increases, more nanoparticles are generated, leading to a greater presence of these particles in the sample. This higher yield of NPs translates to enhanced light absorption, resulting in the observed rise in the optical absorption index. Figure 4.10 presents the data on the NPs mean size and concentrations for the specified samples (S3, S6, and S9), where the concentration of the produced samples increased with increasing scanning speed. For each scanning speed considered, a notable sequence of events unfolds immediately following the irradiation of the target by the initial laser pulse, where a hemispherical shockwave is observed to propagate outward into the surrounding liquid medium [166]. This occurrence is succeeded by the emergence of a high-temperature, dense plume comprised of vapour, gas, and NPs expelled from the target. A discernible discrepancy emerges when examining the effects of these events. For lower scanning speed, it is evident that the plume emissions induced by earlier pulses exhibit a milder character in comparison to those generated by subsequent pulses. As the laser pulses traverse the plume in its initial phase, they retain the capability to ablate the target material. However, as the plume's intensity grows and its spatial distribution expands, the influence of the laser's ponderomotive force becomes insufficient to effectively disperse the high-density plume background. Consequently, the efficacy of the laser in pushing away the plume diminishes, resulting in a scenario where the subsequent ablation is impeded. Eventually, as the plume relaxes and reverts to its original state, the ablation process resumes. Contrastingly, when the scanning speed is at higher rate, the plume left by previous pulses demonstrates a limited impact on subsequent pulses, apart from a minor

attenuation effect on the energy of the later pulses. These findings underscore that, under the condition of lower scanning speed, the intermittent laser ablation process is significantly influenced by the phenomenon of plume shielding [135], [167]. Therefore, increasing the scanning speed resulted in higher NPs yield and concentration, as evident in Figures 4.9, and 4.10. Furthermore, the NPs mean sizes vary from 161.8, 92.81, and 140.7 nm for the samples S3, S6, and S9, respectively. In the quest to elucidate the morphological characteristics of NPs produced from samples S3, S6, and S9, a comprehensive analysis was conducted utilising both FESEM and Field Transmission Electron Microscopy (FTSEM). The acquired micrographs, as presented in Figures 4.11 (a-k) collectively reveal a predominant spherical morphology for the NPs, interspersed with instances of agglomeration or clustering within the colloid. Remarkably, it is worth noting that the size trends established in the DLS analysis align consistently with those observed through STEM. This result indicates that increasing the scanning speed resulted in a decrease in the NPs mean sizes which was also reported before [120], and further increasing the scanning speed increased the NPs mean size. The outcomes of the ablated mass assessment are portrayed in Figure 4.12. A clear trend emerges from the graph which is an augmentation in the scanning speed from 0.1 to 0.5 m/s corresponds to an increase in the amount of material ablated. Specifically, the ablated mass goes up from 0.6 mg to 1.3 mg when the scanning speed increases to 0.5 m/s which suggests an exponential trend. Also, the mass productivity reached a maximum level of 0.86 $mg.h^{-1}.W^{-1}$ once the scanning speed increased to 0.5 m/s. This observed relationship is consistent with the trend seen in the UV-Vis spectra. The escalating ablated mass with higher scanning speeds correlates well with the previously noted increase in NP yield, as depicted in the UV-Vis graphs. In essence, the alignment between the ablated mass and nanoparticle yield reinforces the notion that higher scanning speeds result in more effective ablation processes, leading to both larger quantities of ablated material and heightened production of NPs, as indicated by the optical absorption measurements. In the course of the experiment, variations in the zeta potential of the samples were observed as the laser scanning speed was incrementally adjusted and the results are displayed in Figure 13. Specifically, the zeta potential exhibited a decline from -10.97 mV to -8.27 mV with an increase in scanning speed from 0.1 m/s to 0.3 m/s. Subsequently, a resurgence in the zeta potential to -14.39 mV was noted upon further acceleration of

the scanning speed to 0.5 m/s. These observations indicate that there is no linear correlation between the scanning speed and the stability of the produced colloidal suspensions.

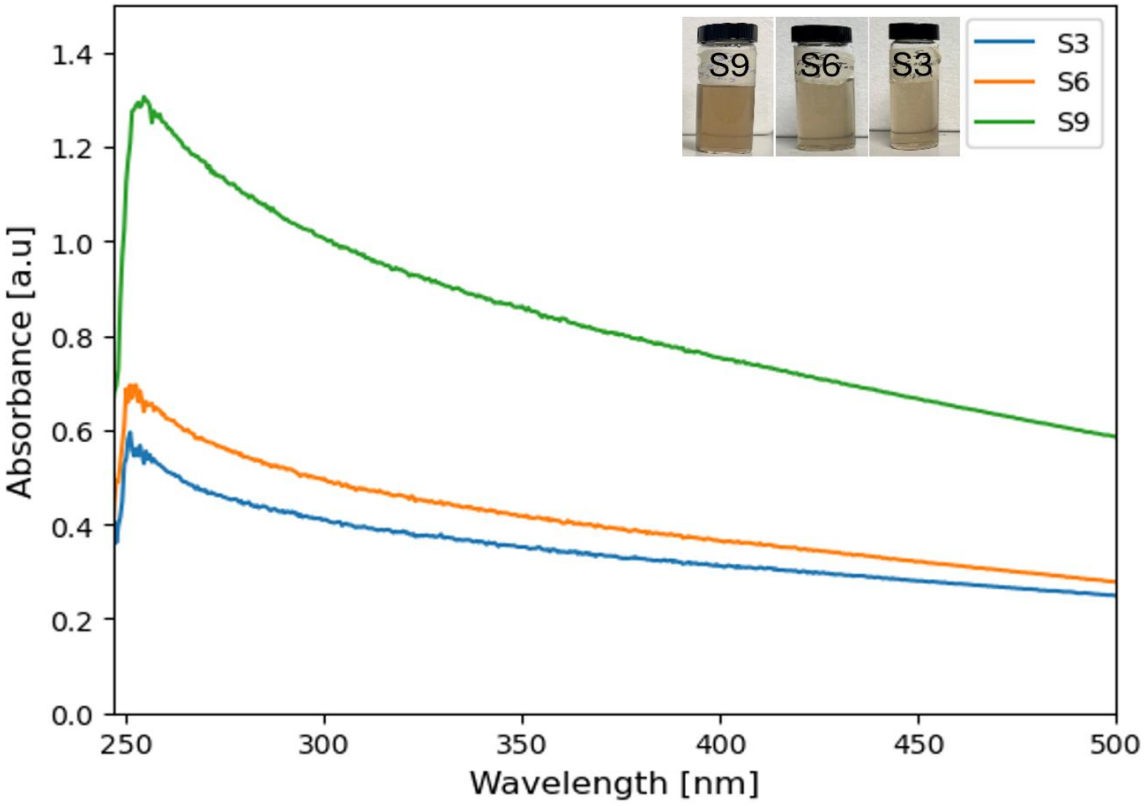


Figure 4.9 UV-Vis spectra for the samples S3, S6, and S9 in a constant laser fluence of 3.78 J/cm2, ablation time of 15 minutes and scanning speed of 0.1, 0.3, and 0.5 m/s respectively, inset image shows the visual inspection of the corresponding samples

Table 4.4 DLS and STEM size measurements of the NPs for samples S3, S6, and S9.

Scanning Speed (m/s) sample name	**DLS NPs Mean Sizes (nm)**	**STEM NPs mean size (nm)**
0.1 S3	143	120
0.3 S6	92	52
0.5 S9	140	109

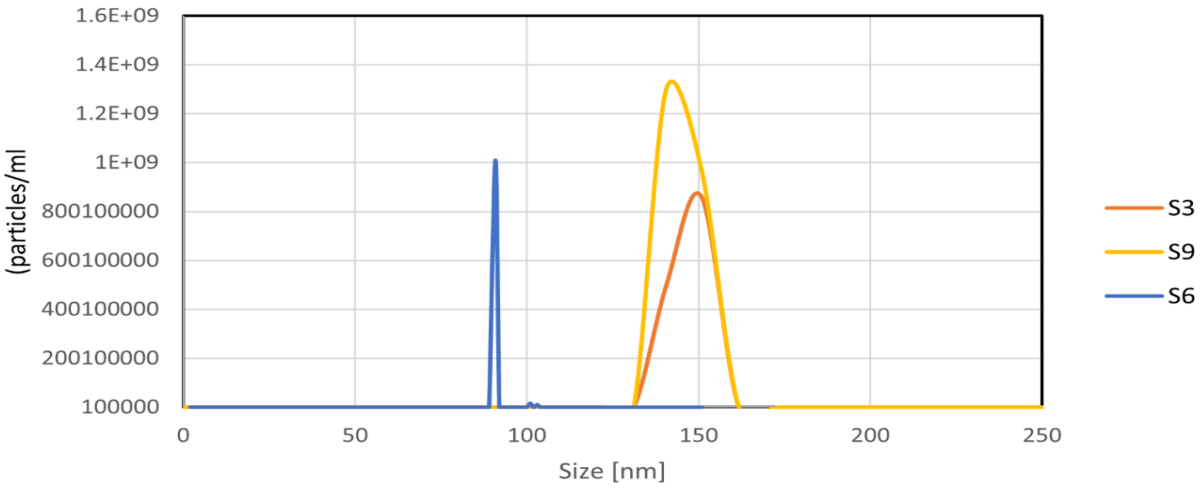


Figure 4.10 DLS results for the samples S3, S6, and S9 in a constant laser fluence of 3.78 J/cm2, ablation time of 15 minutes, and scanning speed of 0.1, 0.3, and 0.5 m/s, respectively.

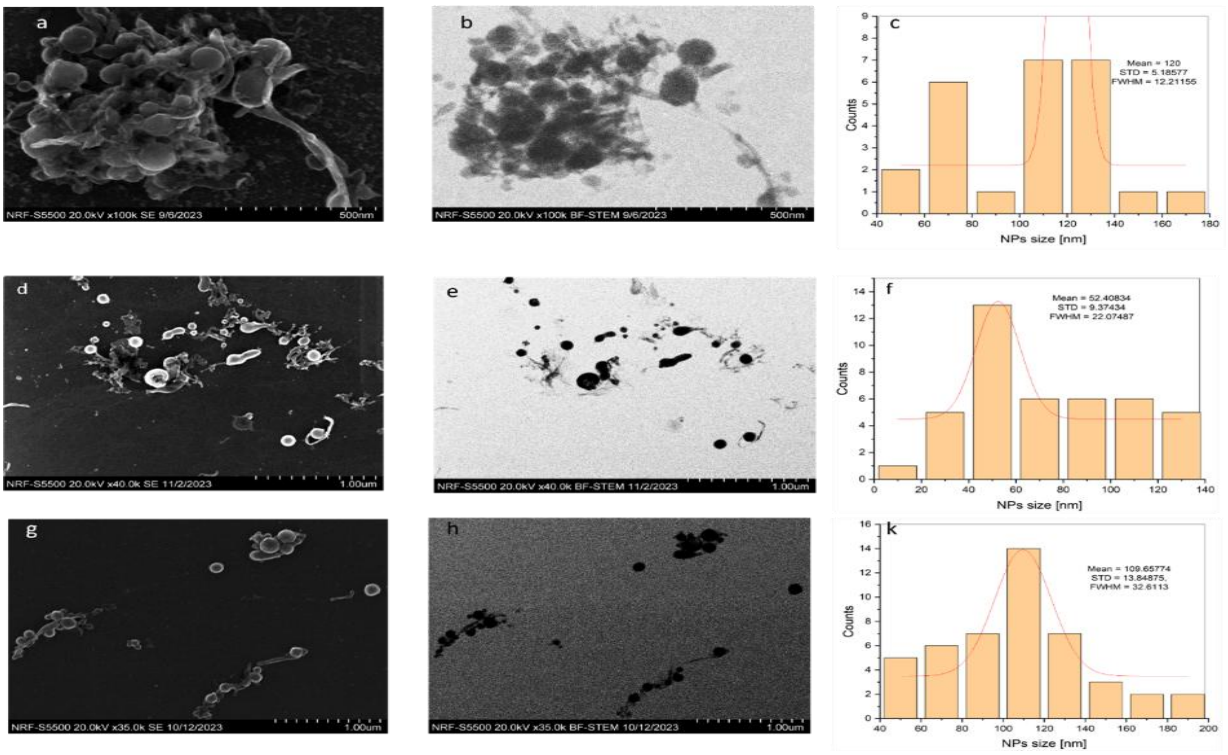


Figure 4.11 Micrographs FESEM, BF-STEM and size distribution of a, b, and c of the sample S3. d, e, and f for the sample S6, and g,h, and k for the sample S9.

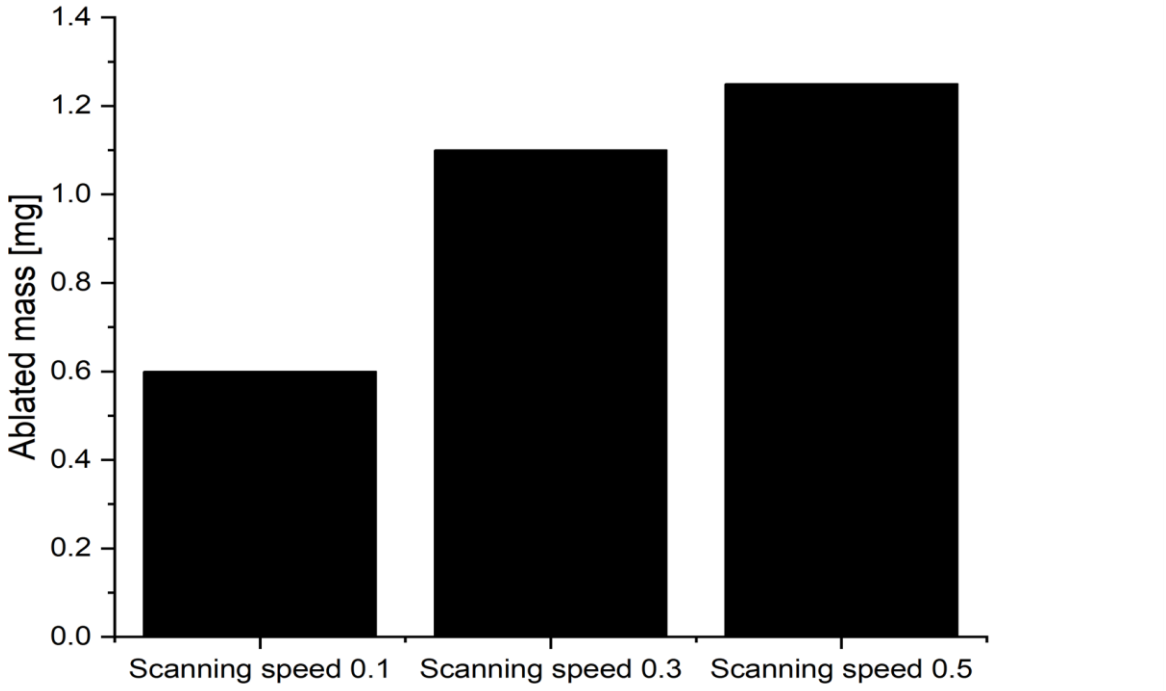


Figure 4.12 Actual ablated mass [mg] in a constant laser fluence 3.78 J/cm2ablation time of 15 minutes, and scanning speed of 0.1, 0.3, and 0.5 m/s.

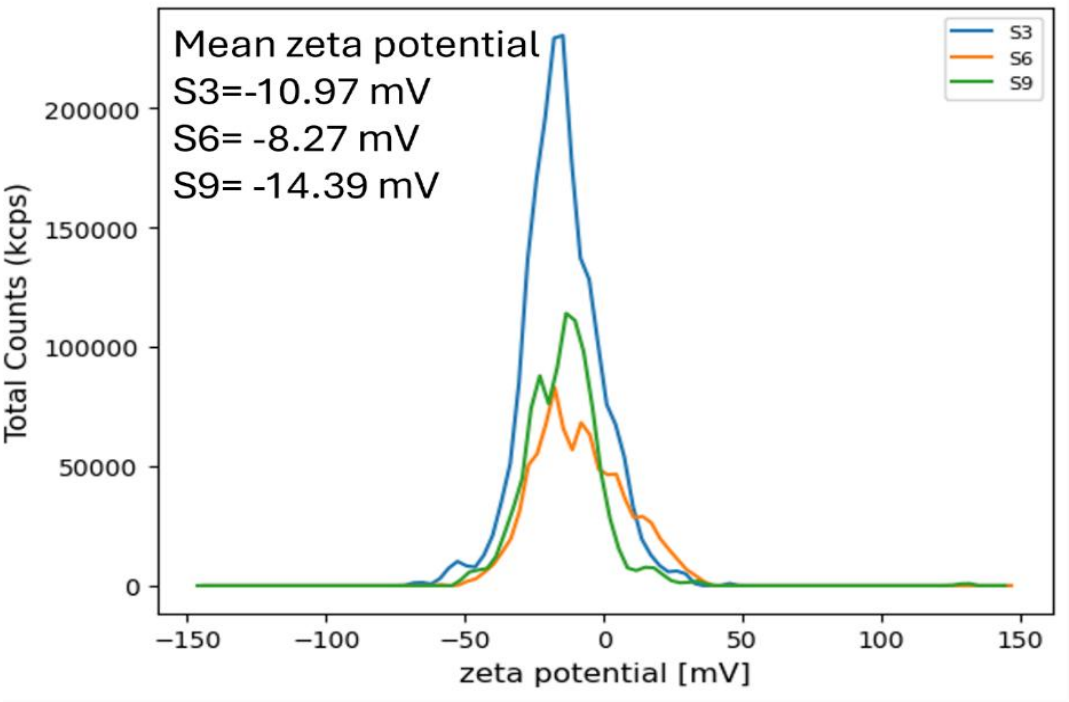


Figure 4.13 Zeta potential measurement of the samples S3, S6, and S9

4.3.4 Effect of laser fluence on the properties of resulting NPs

This section primarily concentrates on the influence of laser fluence on the characteristics of the produced SiC NPs within the colloidal suspensions. Throughout the entirety of the experiments conducted in this segment, the laser scanning speed and ablation time were maintained at constant values of 0.3 m/s and 15 minutes, respectively. Three various laser fluences as mentioned in the DOE, were investigated (3.78, 6.5, and 7.5 J/cm^2). These distinct fluence values were assigned to the respective samples denoted as S6, S15 and S24 respectively. Figure 4.14 illustrates the UV-Vis pattern for the samples S6, S15, and S24 and the inset image shows the corresponding sample photographs, from which an increase in the optical absorption was observed with increasing the laser fluence. This trend was previously reported in the reference[19], where increasing the concentration with increasing the laser fluence was assumed to be related to increasing the ablation area. The optical absorption trends are felt linearly by increasing the wavelength up to 500 nm

and tend to saturate. As per the definition of laser fluence which is the amount of optical energy per unit area on the material, a minimum deposition energy is required to ablate the material [168]. Obviously, in this case, the minimum energy was provided to ablate the material in all the given laser fluences. Furthermore, Figure 4.15 displays the distribution of mean nanoparticle size and concentration obtained through DLS. The data in Figure 4.15 reveals that as the laser fluence was increased, both the mean size and concentration of the generated nanoparticles exhibited an upward trend. This trend was relatively modest when the laser fluence was raised from 3.78 to 6.5 J/cm^2. However, a substantial increase in both mean size and concentration was observed when the laser fluence was further elevated to 7.5 J/cm^2. At lower laser fluences, the target's surface atoms are evaporated, resulting in the formation of NPs through the nucleation of these evaporated atoms. This process tends to produce NPs with a uniform size distribution. Conversely, when the laser fluence is increased, a higher amount of energy is delivered to the target, causing the removal of material through melting rather than evaporation. In this scenario, the interactions of molten metal droplets are disrupted by the laser beam and rapidly cooled, leading to the more NPs being generated with a larger and wider range of sizes [169], [170]. Therefore, increasing the laser fluence resulted in increasing both the concentration and mean size of the SiC NPs. This trend suggests that laser fluences of 7.5 J/cm^2 have the highest impact in the process of SiC NPs using PLAL, which was confirmed in the statistical analysis. Furthermore, Figure 4.16 (a-k) presents the FESEM and BF-STEM images of samples S6, S15, and S24, respectively. These micrographs confirm the presence of spherical NPs, which is further corroborated by size distribution measurements (depicted in subgraphs **c**, **f**, and **k**). The results of the assessment of ablated mass are depicted in Figure 4.17. A noticeable trend becomes apparent in the graph, showing that an increase in laser fluence from 3.78 to 7.5 J/cm² corresponds to a greater amount of material being ablated, where the ablated mass increases from 0.9 mg to 1.42 mg as the laser fluence is raised to 7.5 J/cm². In addition, the mass productivity reached the maximum level at the laser fluence of 7.5 J/cm² with the value of 944 mgh^{-1}W^{-1}. This observed relationship aligns with the trend observed in the UV-Vis data. The increase in ablated mass with higher laser fluences correlates with the previously noted rise in nanoparticle yield, as shown in the UV-Vis graphs. Essentially, the concordance

between ablated mass and nanoparticle yield reinforces the idea that higher laser fluence leads to more effective ablation processes, resulting in both larger quantities of ablated material and increased production of nanoparticles, as indicated by the optical absorption measurements. Furthermore, the colloidal stability of the samples was assessed across a range of laser fluences, as depicted in Figure 4.18. It was observed that an increase in the laser fluence led to a corresponding elevation in the zeta potential values of the colloidal suspensions, ranging from -8.27 mV to -14.22 mV. Ultimately, the optical band gap for all the studied samples was estimated using the Tauc plot method as shown in Figure 4.19. This method involves plotting the square of ($\alpha h\upsilon$) versus the photon energy ($h\upsilon$) and extrapolating the linear portion of the curve to the x-axis intercept, which corresponds to the band gap energy (Eg). The optical band gap of the fabricated silicon carbide ranged from 2.63 to 3.83 eV at room temperature. The actual band gap of 3C silicon carbide is 2.24 eV, and the difference between the estimated value in this study with the actual value can be correlated to the quantum size effect [19]. The results also suggested that increasing the NP size decreased the optical band gap. As the particle size diminishes, the widening of the band gaps can be attributed to the corresponding increase in lattice parameters as the particle diameter decreases [171].

Table 4.5 DLS and STEM size measurements of the NPs for samples S6, S15, and S24.

Laser Fluence (J/cm2) sample name	**DLS NPs Mean Sizes (nm)**	**STEM NPs mean size (nm)**
3.78 S6	92	52
6.5 S15	99	59
7.5 S24	140	83

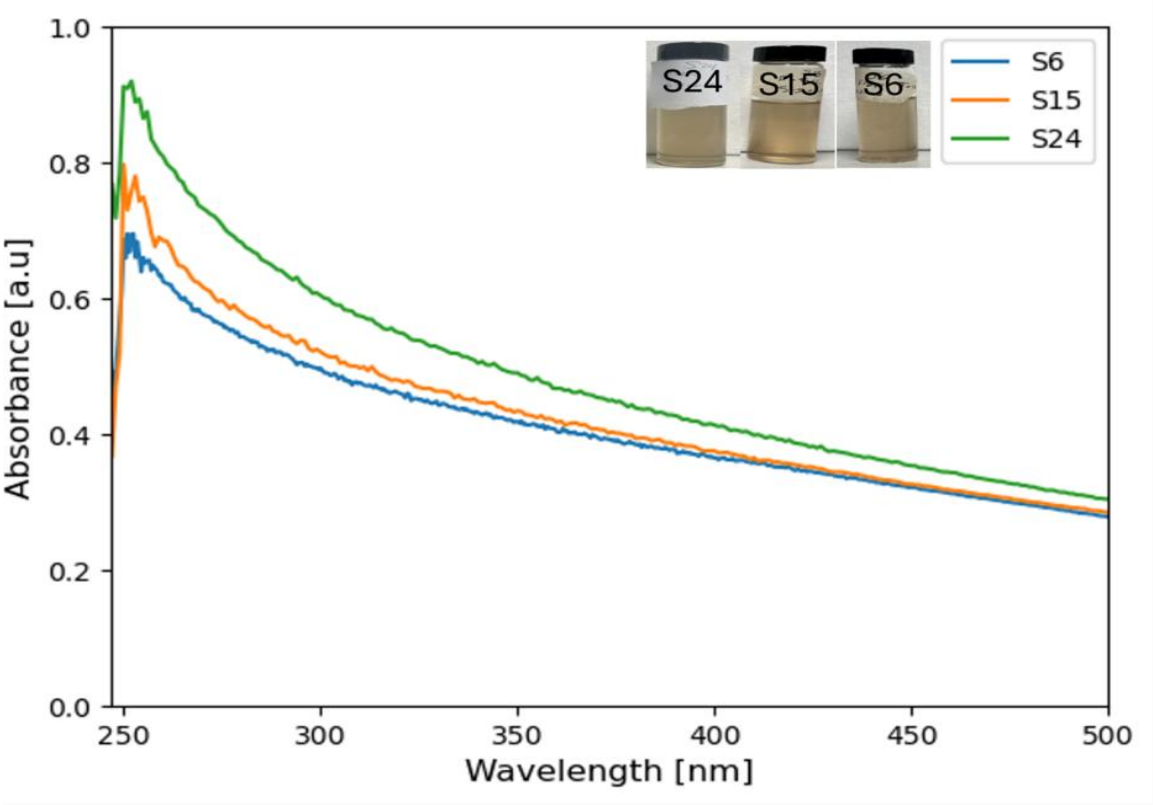


Figure 4.14 UV-Vis spectra for the samples S6, S15, and S24 in a constant scanning speed of 0.3 m/s, ablation time of 15 minutes and laser fluences of 3.78, 6.5, and 7.5 J/cm2 respectively, inset image shows a picture of the corresponding samples.

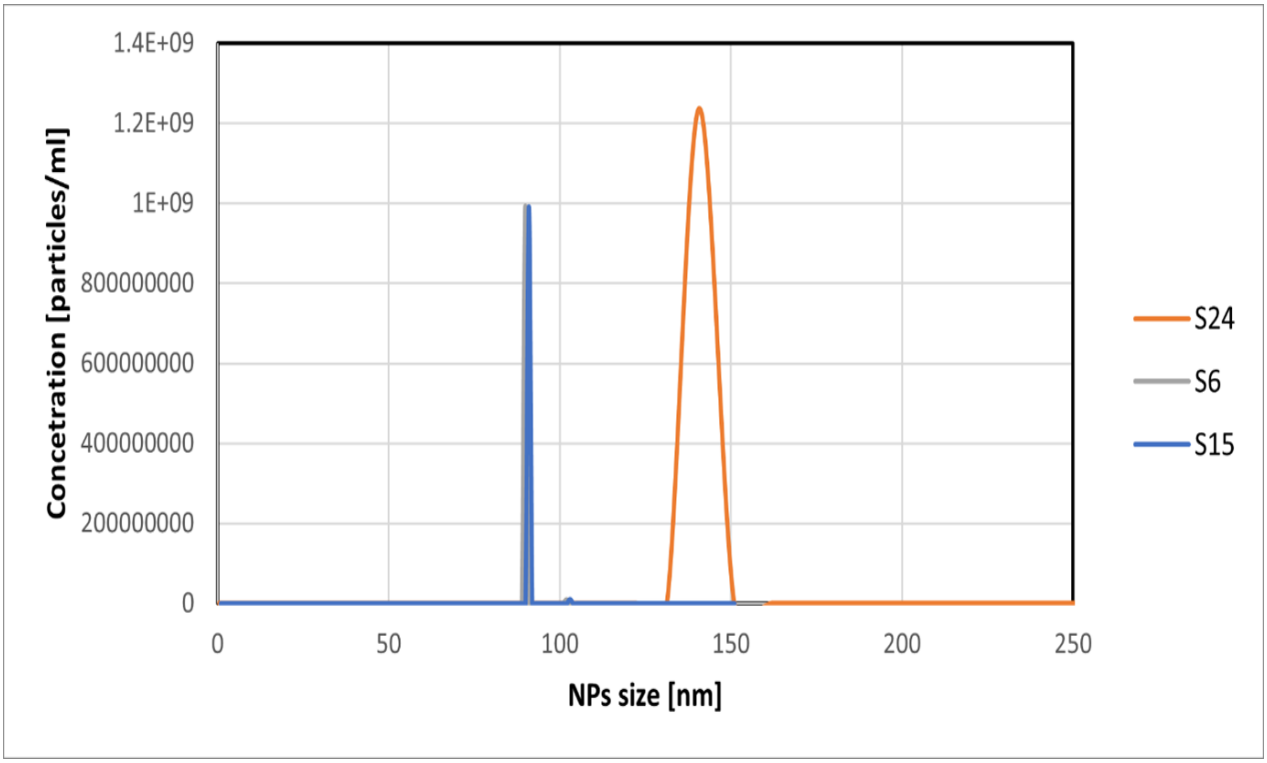


Figure 4.15 DLS results for the samples S6, S15, and S24 in a constant scanning speed of 0.3 m/s, ablation time of 15 minutes, and laser fluences of 3.78, 6.5, and 7.5 J/cm2 respectively.

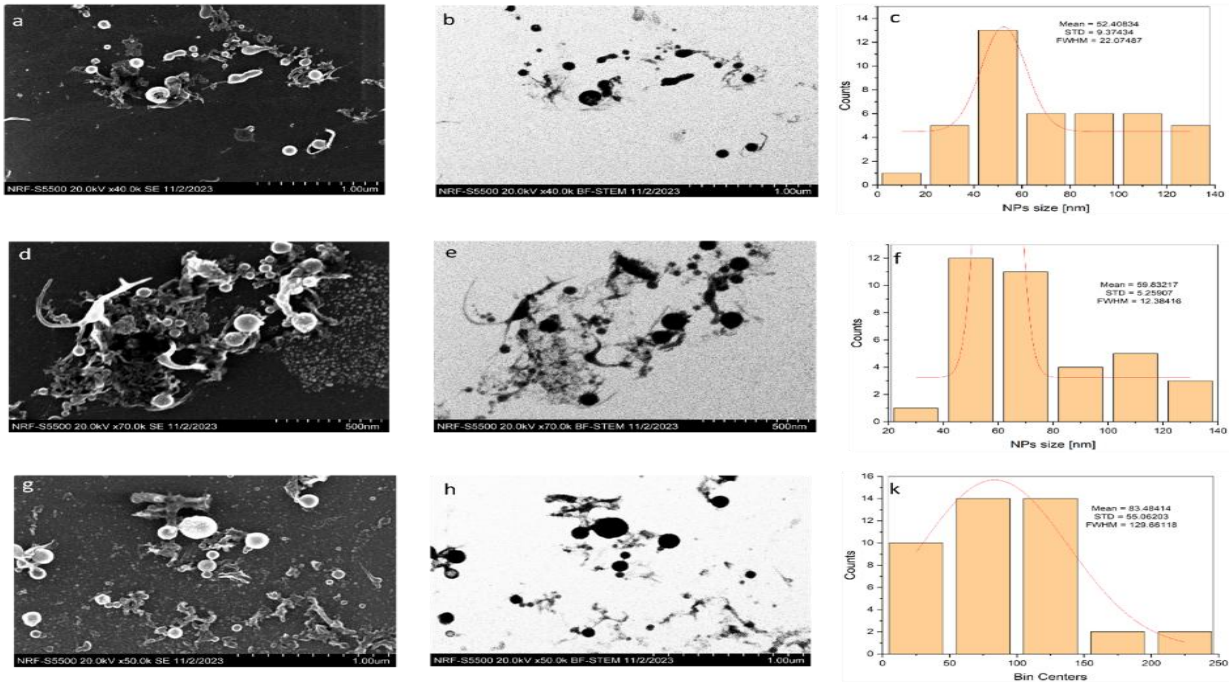


Figure 4.16 Micrographs FESEM, BF-STEM and size distribution of a, b, and c of the sample S6. d, e, and f for the sample S15, and g,h, and k for the sample S24.

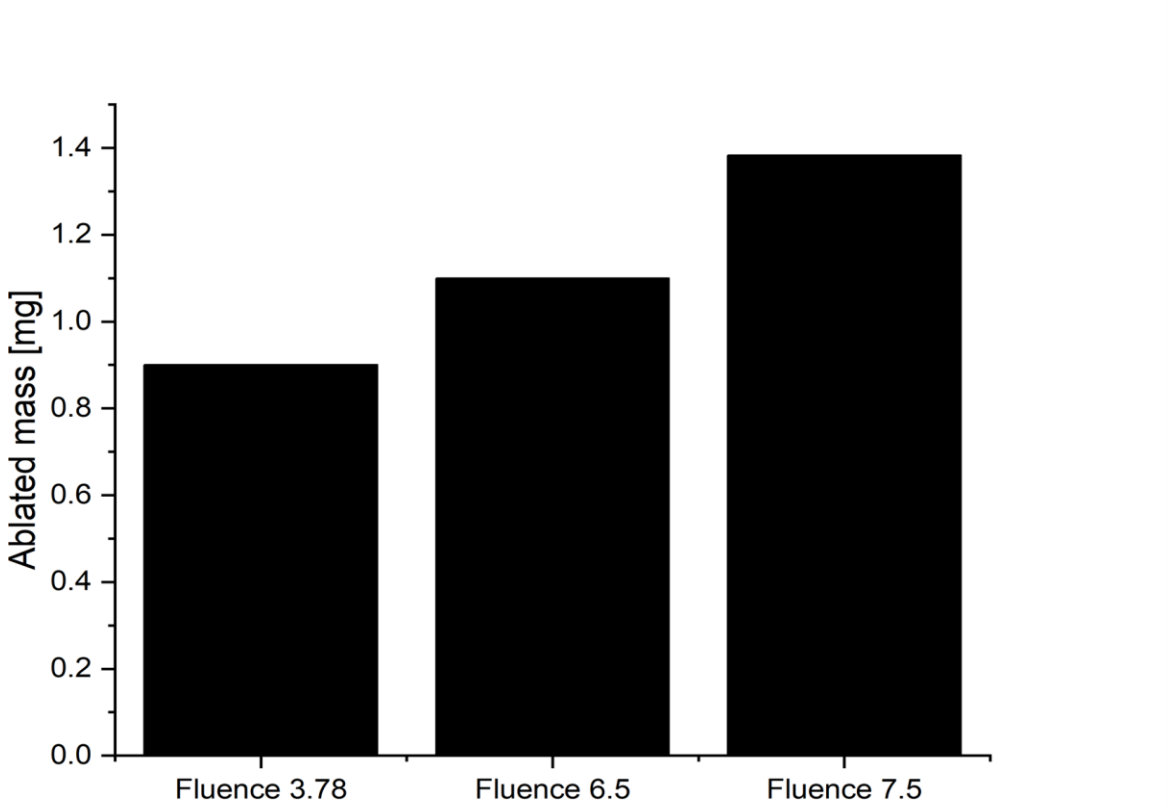


Figure 4.17 Actual ablated mass [mg] in a constant ablation time of 15 minutes and scanning speed of 0.3 m/s and laser fluences of 3.78, 6.5, and 7.5 J/cm2.

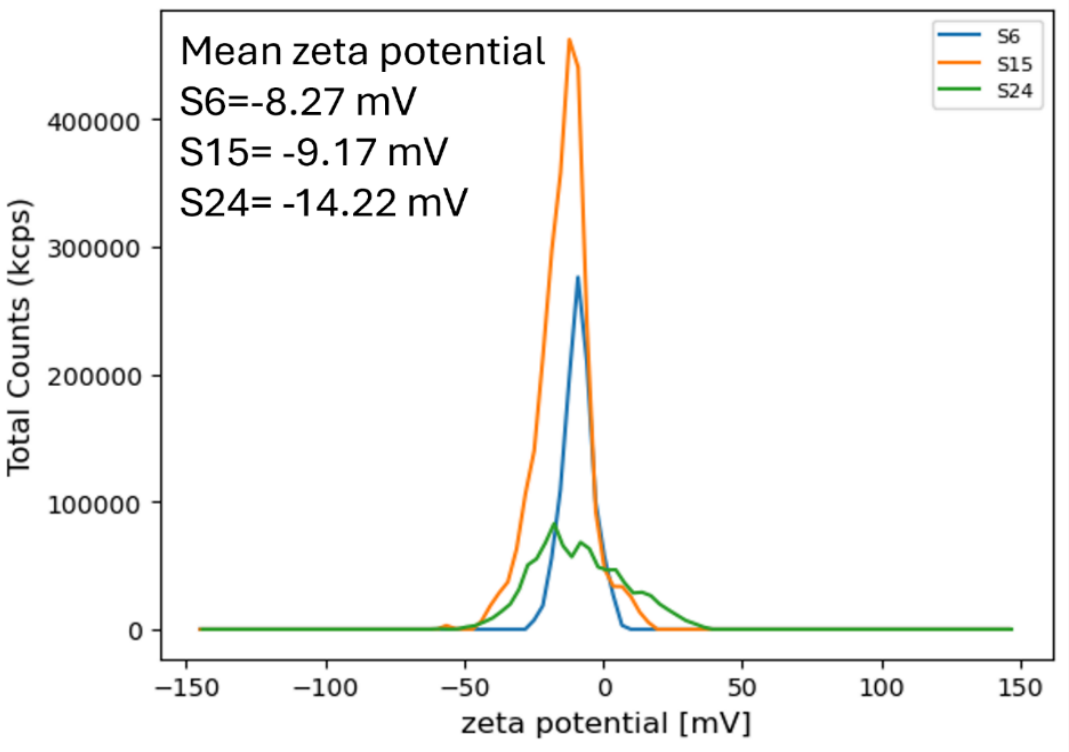


Figure 4.18 Zeta potential measurement of the samples S6, S15, and S24

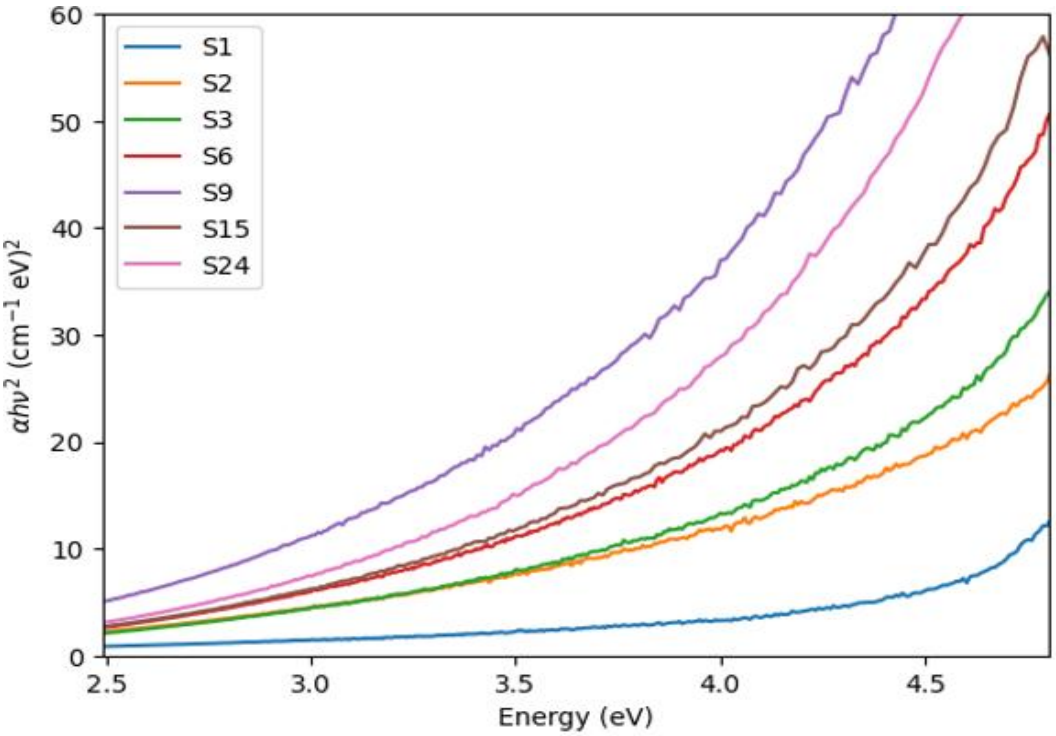


Figure 4.19 Optical band gap estimation using the Tauc plot method

4.4 Conclusion

In conclusion, this study successfully synthesised silicon carbide NPss (SiC NPs) through nanosecond Pulsed Laser Ablation in Liquid (PLAL) in deionised water. The investigation into the impact of laser processing parameters specifically, laser fluences, scanning speed, and ablation time revealed a direct correlation between these factors and the resulting ablation efficiency and properties of SiC NPs. The ablation efficiency of SiC NPs was determined for the first time[20], [36], [39], [40], and under optimised conditions, an ablation time of 15 minutes, a scanning speed of 0.5 m/s, and a laser fluence of 7.5 J/cm² the total ablated mass reached a maximum of 1.8 mg with the maximum mass productivity of 1.196 mgh-1W-1. Notably, an increase in laser fluence, scanning speed, and ablation time led to higher SiC NP concentrations, as evidenced by UV absorption and DLS results. The non-linear trend observed between ablated mass and laser fluence indicated the sensitivity of the process to these parameters, which was not

reported in previous work[37].. Furthermore, the study highlighted a substantial increase in mean size, zeta potential and concentration of SiC NPs at a fluence of 7.5 J/cm². Although there was a difference in size distribution between image analysis and DLS data, the overall trend remained consistent. The XRD pattern showed that the 3C SiC NPs were fabricated which had the same phase composition as the target material. Moreover, the EDX result confirmed the presence of silicon and carbon in the resulting NPs. Moreover, the results also suggested that increasing the NP size decreased the optical band gap. Overall, this research demonstrated the feasibility of producing highly concentrated SiC NP colloids through nanosecond pulsed laser ablation in liquid, providing valuable insights for the controlled synthesis of SiC NPss with tailored properties for various applications. The inkjet printing of the highly concentrated SiC colloids under the optimum condition of ablation, and investigation of the concentration of the colloid on properties such as thermal conductivity, electrical conductivity, and heat resistance of the printed layer will be desirable for further works.

5 Chapter 5

Thermal Conductivity Enhancement of Epoxy Abrasive Composites Using Hybrid SiC–Al_2O_3 Fillers: Experimental, Analytical, and FEA Approaches

Abstract

This study investigates the thermal conductivity of epoxy matrix-based abrasive composites through the incorporation of silicon carbide (SiC) and aluminium oxide (Al_2O_3) particles. A goal of such material design is to achieve controlled heat transfer with the potential to increase component lifetimes. Thermal conductivity measurements, infrared thermal imaging, scanning electron microscopy (SEM), analytical modelling, and finite element analysis (FEA) were employed to examine the influence of particle type, particle size, particle loading, and hybrid filler ratios on heat transfer behaviour. The results demonstrated that composites with both SiC and Al_2O_3(called hybrid composites) exhibited higher thermal conductivity and longer lifetimes compared to just using Al_2O_3alone. Hybrid SiC-filled composites exhibited significantly higher thermal conductivity than the hybrid Al_2O_3-filled systems due to improved phonon transport, stronger covalent bonding, and superior particle dispersion. Increasing particle size and filler loading enhanced thermal conductivity, with the highest value of approximately 2.78 W/mK achieved for a hybrid composite containing a 9:1 SiC-to-Al_2O_3 ratio. In contrast, nano-sized particles showed reduced thermal conductivity at high loadings because of particle agglomeration and increased interfacial thermal resistance. Infrared thermal imaging further confirmed that composites with higher thermal conductivity exhibited improved thermal stability and prolonged operational lifetime during grinding applications. Analytical and FEA models successfully predicted the experimental trends, with FEA demonstrating closer agreement with experimental measurements. The findings highlight the potential of hybrid ceramic-filled epoxy composites for the development of thermally stable and longer life time abrasive materials for demanding industrial applications.

Keywords: Thermal conductivity, silicon carbide, aluminium oxide, hybrid, composite

5.1 Introduction

Epoxy resins are among the most widely used thermosetting polymers in structural, electrical, and coating applications due to their excellent mechanical strength, chemical resistance, dimensional stability, and strong adhesion to diverse substrates [172], [173], [174]. In abrasive systems—such as grinding tools, polishing pads, bonded abrasives, and wear-resistant coatings—epoxy matrices serve as effective binders that securely hold abrasive particles while maintaining structural integrity under mechanical stress. However, a major limitation of epoxy resins is their inherently low thermal conductivity (typically 0.2–0.3 $W \cdot m^{-1} \cdot K^{-1}$), which restricts their performance in applications involving frictional heating and high mechanical loads [175].

During abrasive operations, significant heat is generated at the contact interface due to friction and material removal processes. Poor heat dissipation can lead to thermal degradation of the backing material, reduced bonding strength, dimensional instability, and premature tool failure [176]. Therefore, enhancing the thermal conductivity of epoxy-based abrasive composites and using them as the grinding backing material is critical to improving thermal stability, wear resistance, and service lifetime. One effective strategy to overcome this limitation is the incorporation of thermally conductive ceramic fillers into the polymer matrix [177], [178], [179].

Among the available ceramic fillers, silicon carbide (SiC) and aluminium oxide (Al_2O_3) have attracted considerable attention because of their high intrinsic thermal conductivity, excellent hardness, chemical inertness, and compatibility with abrasive applications [180], [181], [182], [183], [184], [185], [186], [187]. Silicon carbide exhibits high thermal conductivity, superior mechanical strength, and outstanding thermal stability, making it suitable for high-performance abrasive systems. Similarly, Aluminium oxide offers high hardness, good thermal conductivity, and cost-effectiveness, which are advantageous for industrial-scale composite fabrication [188], [189], [190], [191].

The particle size of fillers plays a crucial role in determining the thermal and mechanical performance of

polymer composites [192], [193], [194]. Micron-sized particles can form effective heat-conducting pathways at higher loadings [195], while nano-sized particles provide large interfacial surface areas that can enhance phonon transport and interfacial bonding [196]. However, nanoparticles also tend to agglomerate due to high surface energy [197], potentially hindering thermal transport if not properly dispersed. A hybrid approach combining micro- and nano-sized particles may offer synergistic effects by improving particle packing density, reducing interfacial thermal resistance, and promoting the formation of continuous thermal conduction networks within the epoxy matrix.

Although numerous studies have reported the enhancement of thermal conductivity in polymer composites using ceramic fillers, limited work has systematically compared the effects of micron- and nano-sized SiC and Al_2O_3 particles within the same epoxy system, particularly in the context of abrasive applications. Understanding the influence of particle size, morphology, loading fraction, and dispersion quality on heat transfer mechanisms is essential for optimising composite performance.

This study investigates the enhancement of thermal conductivity in epoxy resin composites incorporating micron- and nano-sized SiC and Al_2O_3 particles for abrasive applications. The goal of this work was to (i) evaluate the influence of particle type and size on thermal conductivity, (ii) analyse the microstructural characteristics that govern heat transfer pathways, and (iii) assess the potential of hybrid filler systems to improve thermal management without compromising structural integrity. To the authors' knowledge, this study is the first to systematically investigate the combined influence of micron- and nano-sized SiC and Al_2O_3 fillers, hybrid filler ratios, and particle loading on the thermal conductivity of epoxy-based abrasive composites using integrated experimental, analytical, and finite element approaches. The findings herein contribute significantly to the development of high-performance, thermally stable epoxy-based abrasive composites suitable for demanding industrial environments.

5.2 Materials and Methods

5.2.1 Materials

Micron-sized ceramic particles were procured from Kemet International. Two types of abrasive materials were used: silicon carbide and aluminium oxide. For both materials, four different particle mean sizes were selected: 4.5, 58, 129, and 185 μm.

The polymer matrix used in this study was Gurit AMPRO Epoxy Resin, which was supplied together with AMPRO Fast Hardener by Gurit. The epoxy resin and hardener were mixed at a ratio of 3:1 by weight, following the manufacturer's recommended formulation to ensure proper polymerisation and curing of the epoxy system.

5.2.2 Preparation of Epoxy–Particle Composites Coated Substrate

A design of experiments was prepared in which three variables and 4 factors were used to determine the most suitable process. The experimental design is shown in Table 5.1 for the SiC and Al_2O_3 was investigated. Table 5.2 shows the mixing ratio parameters, in which the particles were mixed together in different ratios.

Table 5.1 Particle mean size and loading for SiC and Al_2O_3 particles used in the fabrication of tested samples

Mean particle size μm	**Particle loading wt%**
4.5	5
4.5	15

4.5	30
4.5	45
58	5
58	15
58	30
58	45
129	5
129	15
129	30
129	45
185	5
185	15
185	30
185	45

Table 5.2The mixing ratio of the SiC and Al_2O_3 particles used for fabrication of tested samples.

Parameter	Mixing ratio
SiC:Al_2O_3	9:1
SiC:Al_2O_3	7:3
SiC:Al_2O_3	3:7
SiC:Al_2O_3	1:9

The nano-sized particles were also examined to compare the thermal conductivity of the materials in different size scales, including micron-sized and nano-sized. The particles were purchased from Merck with a mean size of 100 nm for both materials, and four different particle loadings were prepared and examined.

The particle loading used was 5, 15, 30 and 45 w%.

Initially, the epoxy resin was poured into a 100 mL beaker and stirred continuously for 5 minutes to minimise the presence of entrapped air bubbles and to ensure uniform consistency. Subsequently, the SiC or Al_2O_3 micron-sized particles were gradually added to the epoxy resin. The mixture was stirred for approximately 20 minutes to obtain a homogeneous suspension, ensuring that the particles were uniformly dispersed throughout the epoxy matrix.

After achieving uniform dispersion of the ceramic particles, the AMPRO fast hardener was added to the mixture at the predetermined 3:1 resin-to-hardener ratio. The mixture was then stirred for an additional 5 minutes to ensure complete blending and initiation of the curing reaction. Finally, the

fluid composite epoxy was coateded onto a 1 mm-thick cotton backing sheet which was used as the substrate for depositing the composite layer. The prepared epoxy–particle mixture was applied onto the backing sheet using a manual hand-brushing technique. Care was taken to ensure that the composite layer was evenly distributed across the entire surface, maintaining a uniform thickness. Following the coating process, the composite-coated sheets were placed in an oven at 50 °C for 20 minutes to facilitate the curing and polymerisation of the epoxy matrix. After the curing process was completed and the sheets were fully dried, the samples were cut into appropriate dimensions for subsequent characterisation and testing.

5.3 Materials Characterisation

5.3.1 Thermal conductivity

Thermal conductivity measurements were conducted using a C-Therm Trident Thermal Conductivity Analyser equipped with a Transient Plane Source (TPS) Flex sensor. The TPS technique employs a double-sided hot-disc sensor capable of simultaneously determining the thermal conductivity, thermal diffusivity, and specific heat capacity of materials from a single measurement. The measurements were performed in

accordance with ISO 22007-2 and ASTM E3088-25 standards.

During testing, electrical power was applied to the spiral heating element of the TPS sensor, generating a controlled heat pulse. This induced a temperature rise at the interface between the sensor and the sample surface, resulting in a corresponding voltage variation across the sensor element. Initial trial runs were first conducted to estimate the appropriate testing parameters, including power level, test duration, and sensor size. These parameters were subsequently refined iteratively until stable and reliable measurement conditions were achieved, following the guidance outlined in ISO 22007-2. The resulting temperature–time response was analysed using an iterative solving procedure to determine the thermal conductivity and thermal diffusivity of the samples. A 6 mm diameter sensor was selected for all measurements, as the prepared test samples possessed a diameter of 20 mm, ensuring sufficient contact area and measurement accuracy. A schematic representation of the sample geometry and sensor configuration is presented in Figure 1 of the supplementary document. The test was conducted 5 times for each sample, and the average was calculated for the thermal conductivity values

5.3.2 SEM Imaging

The Carl Zeiss LS15 scanning electron microscope was used to observe the surface of the sample at high magnification. The SEM was used to investigate the particle distribution on the surface of the sample, as well as feedstock powders, which were used in this study,

5.3.3 Grinding disk test setup

To evaluate the practical applicability of the developed composites under realistic operating conditions, multiple samples were fabricated and tested at the sponsoring company's facility. Both micron-sized and nano-sized filler particles were deposited onto the surface of grinding discs and examined during grinding operations. A Shunner Electrical Grinder was used with a rotation speed of 8000 rpm, a stainless steel 316 substrate was used as the substrate for the grinding, and an operator performed the test with a constant

applied loading of 50 N for each test for 5 minutes. The temperature evolution on the backing side of the grinding disc was monitored using a Fluke RSE300 thermal imaging camera in conjunction with SmartView R&D software. Figure 2 in the appendices document illustrates the thermal imaging setup and a representative prepared sample.

Prior to experimentation, the thermal imaging system was calibrated to minimise systematic measurement errors and improve temperature accuracy. Calibration was performed using a reference sample heated to 300 °C, where the corresponding temperature was recorded using the thermal camera. Subsequently, the emissivity values of SiC and Al_2O_3 powders were incorporated into the measurement system, and the calibration procedure was repeated to obtain more accurate thermal measurements during grinding operations. This approach enabled reliable evaluation of the thermal dissipation behaviour and thermal stability of the coated grinding discs under operational conditions.

5.4 Analytical model of the prepared grinding disk thermal conductivity

The system under consideration is a flat laminate composed of three perfectly bonded together layers stacked in a through-thickness direction. The total thickness is given by the equation 1. A schematic representation of the layers being tested is illustrated in the Figure 5.1 alongside the meshing convergence and the sample being modelled. The corresponding layer thicknesses used in the simulation are presented in Table 5.3.

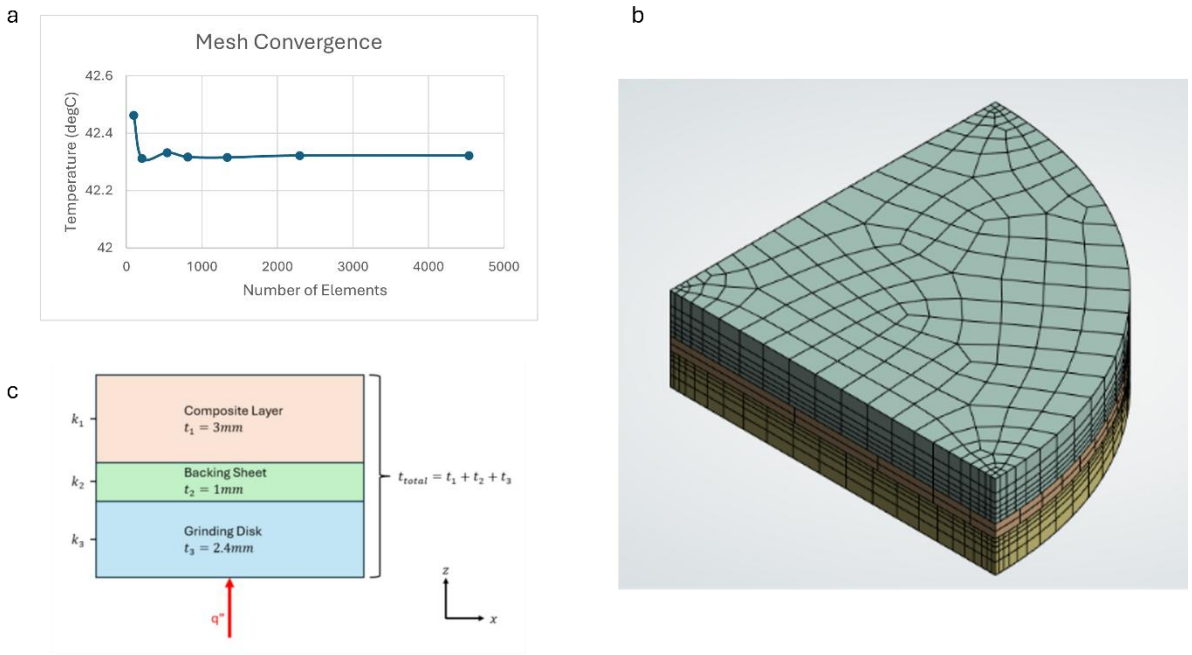


Figure 5.1 a) the meshing convergence of the model, b) schematic representation of the meshing sample, and c) schematic illustration of the three layers being modelled.

Table 5.3 Thickness of the layers used in the FEA analysis

	Composite Material	**Backing Material**	**Grinding Disk**
Thickness	3mm	1mm	2.4mm

$$t_{total} = t_1 + t_2 + t_3$$

Equation 1

where t_1, t_2 and t_3 are the thicknesses of layers 1, 2 and 3, respectively. Hence, k_1, k_2 and k_3 are the corresponding thermal conductivities. Each layer is assumed to occupy the same circular cross-sectional area as shown in equation 2.

$$A = \pi r^2$$

Equation 2

where $r = 37.5\text{mm}$, (based on the given geometry of the disks, 75mm diameter).

A consistent Cartesian coordinate system is adopted such that x and y represent in-plane directions and z represents the through-thickness direction. To obtain a closed-form analytical solution, the following assumptions are applied: Steady-state heat conduction as in equation 3.

$$\frac{\partial T}{\partial t} = 0$$

Equation 3

Temperature is time-independent. The solution represents the steady-state limit of the transient FE simulation. Secondly, no internal heat is generated, as shown in equation 4.

$$\dot{q}_{gen} = 0$$

Equation 4

Thirdly, homogeneous and Isotropic layers, meaning each layer has a constant thermal conductivity (equation 5).

$$k = k_i$$

Equation 5

Within each individual layer, where material properties don't vary with temperature. Additionally, Perfect

thermal contact between layers equation 6.

$$T^- = T^+$$

Equation 6

And normal heat flux is continuous across interfaces as in equation 7.

$$-k\frac{-\partial T}{\partial z} = -k\frac{+\partial T}{\partial z}$$

Equation 7

and one-dimensional dominant heat flow (equation 8).

$$\frac{\partial^2 T}{\partial x^2} = 0, \quad \frac{\partial^2 T}{\partial y^2} = 0$$

Equation 8

Heat transfer is primarily assumed to occur in the z-direction (through the thickness direction), which simplifies the governing equation to: $\frac{\partial^2 T}{\partial z^2} = 0$ within each layer.

Background Calculations

The calculations for the X and z directions are used for inputting into the Ansys Workbench engineering data, and these calculations are done for both the grinding disk and backing sheets.

X Direction

Starting with Fourier's law, with 1D conduction in the x-direction, this gives equation 9

$$q''_x = -k_x \frac{dT}{dx}$$

Equation 9

Where q''_x is the heat flux $[\frac{W}{m^2}]$; k is the thermal heat conductivity (W/m.K); dT/dx is the temperature gradient. If the temperature varies approximately linearly across a distance Δx, Then equations 10, 11, 12

and 13 give

$$\frac{dT}{dx} \approx \frac{\Delta T}{\Delta x}$$

Equation 10

$$q''_x = -k_x \frac{\Delta T}{\Delta x}$$

Equation 11

It can also be assumed that:

$$\dot{Q}_x = q''_x A$$

Equation 12

Where Q_x is the Heat transfer rate [W]. This means:

$$\dot{Q}_x = \left(= -k_x \frac{\Delta T}{\Delta x}\right) A$$

Equation 13

In equation 13, A can be written as the area as in equation 14.

$$A = \pi r^2$$

Equation 14

This gives the solution to equation 15.

$$\dot{Q}_x = -k_x \pi r^2 \frac{\Delta T}{\Delta x}$$

Equation 15

In the case of this study, the magnitude of the value is all that is required, simplifying equation 15 to equation 16.

$$\dot{Q}_x = k_x \pi r^2 \frac{\Delta T}{\Delta x}$$

Equation 16

This can be rearranged to find k_x as in equation 17.

$$k_x = \frac{\dot{Q}_x \Delta x}{\pi r^2 \Delta T}$$

Equation 17

Equation 17 can be used for all three layers independently, giving in-plane conductivity in the x-direction but not through thickness.

Z Direction

For 1D conduction in the z-direction, Fourier's Law can again be used as shown in equation 18

$$q''_z = -k_z \frac{dT}{dz} \approx -k_z \frac{\Delta T}{\Delta z}$$

Equation 18

The difference in the Z direction comes in the next step when the heat flux is converted to the heat transfer rate, as in the Z direction, the area is given by equation 19

$$A = L \times W$$

Equation 19

Where L is the full diameter[m] of one of the disks (which is uniform for each layer); W is the thickness of one layer [m]. The formula $\dot{Q}_z = q''_z A$ is also to be used in this case, and using this gives a final formula as in equation 20.

$$\dot{Q}_z = -k_z LW \frac{\Delta T}{\Delta z}$$

Equation 20

Where the Heat transfer rate Q_z and the temperature change ΔT are also taken to be constant through the layers. The thickness value, W in this case, must be taken for each individual layer, not the total thickness. Ignoring the negative sign, due to the magnitude of the value only being used. The formulas are rearranged to find k_z, L and Δz cancel each other out then to give equation 21.

$$k_z = \frac{\dot{Q}_z \Delta z}{LW\Delta T} = \frac{\dot{Q}_z}{W\Delta T}$$

Equation 21

And equation 21 can be used for each of the layers.

5.5 Finite Element Analysis (FEA) setup

5.5.1 Geometry and Boundary Conditions

The geometry of the finite element model was developed based on the assumptions used in the analytical calculations. The system consisted of three perfectly bonded layers stacked sequentially in the through-thickness direction, comprising the composite coating layer, backing material, and grinding disc. To simplify the computational analysis while maintaining representative thermal behaviour, all layers were modelled as cylindrical structures with a uniform diameter of 75 mm.

The geometries were generated in SolidWorks, where each layer was initially modelled independently and subsequently assembled into a multilayer structure. To reduce computational cost and improve simulation efficiency, a quarter-symmetry model was employed. The cylindrical geometry was sectioned into four equal parts, and symmetry boundary conditions were applied to the two cut faces to represent the full geometry while suppressing lateral heat loss. This approach significantly reduced computational time without compromising the accuracy of the simulation.

Perfect thermal contact was assumed between all adjacent layers. Specifically, the top surface of the grinding disc was assumed to be in complete contact with the bottom surface of the backing material, while the top surface of the backing layer was in direct contact with the bottom surface of the composite coating layer.

The thermal boundary conditions were selected to represent realistic grinding and ambient operating conditions. An initial temperature of 20 °C was assigned uniformly throughout the model to represent room-temperature conditions prior to operation. A constant heat flux of 1400 W/m² was applied to the bottom surface of the grinding disc to represent the fraction of interfacial frictional heat that is conducted into the

disc/backing assembly during grinding. This value was estimated using a friction-power balance commonly applied in grinding thermal analysis, in which the total heat generation rate at the disc–workpiece interface is given by $q_{total} = \mu F_n V/A$, where μ is the apparent friction coefficient between the abrasive disc and the steel substrate, F_n is the operator-applied normal force, V is the mean sliding velocity at the disc face, and A is the nominal contact area[34]. For the grinding disc used in this study (75 mm diameter, 8000 rpm rotational speed), the mean sliding velocity at the disc face is approximately 21 m/s, and the nominal contact area is $A \approx 4.42 \times 10^{-3}$ m². Using an applied normal force of $F_n = 50$ N, consistent with the constant applied loading condition described in Section 2.4.3, and a representative apparent friction coefficient for an abrasive/steel dry sliding contact of $\mu \approx 0.3$ [35], the total interfacial heat generation rate is estimated as:

$q_{total} = \mu F_n V/A = (0.3)(50\ N)(21\ m/s) / (4.42 \times 10^{-3}\ m^2) \approx 7.1 \times 10^4\ W/m^2$

Grinding heat-partition studies have consistently shown that the fraction of this heat conducted into the abrasive tool side of the contact is small relative to that carried into the workpiece, chips, and surrounding air, because the low thermal conductivity of the resin/epoxy-based disc limits its ability to draw heat away from the interface relative to the higher-conductivity steel substrate. Assuming a disc-side partition fraction of approximately 2–5%, consistent with reported partition ratios for low-conductivity abrasive tooling, gives an estimated flux entering the disc assembly of approximately:

$(7.1 \times 10^4 – 1.19 \times 10^5\ W/m^2) \times (0.02–0.05) \approx 1{,}400\ W/m^2$. Free convection boundary conditions were imposed on the top surface of the composite layer to account for heat dissipation to the surrounding environment, using a convective heat transfer coefficient of 12 W/m²K and an ambient temperature of 20 °C. The selected convection coefficient lies within the typical engineering range reported for natural convection in air (5–25 W/m²K). Furthermore, adiabatic boundary conditions (zero heat flux) were applied to the symmetry planes to eliminate lateral heat losses.

5.5.2 Meshing Strategy and Simulation Cases

A multizone meshing strategy was adopted as the baseline mesh configuration. Mesh convergence analysis

was performed using the maximum temperature on the top surface as the convergence criterion. The convergence study was conducted for the initial configuration consisting of 5 wt.% SiC filler with a SiC_2O_3 ratio of 10:0 and a particle size of 4.5 μm. The relationship between mesh density and maximum temperature is presented in Figure 1a, where it illustrates the mesh convergence behaviour, meshing configuration, and schematic representation of the composite layer. To reduce computational time while maintaining acceptable accuracy, the mesh containing 2296 elements was selected instead of the finer 4534-element model.

Three primary simulation case groups were developed based on the experimental configurations. The first group investigated epoxy composites reinforced solely with SiC particles using four particle sizes (4.5 μm, 58 μm, 129 μm, and 185 μm) at four filler loadings (5 wt.%, 15 wt.%, 30 wt.%, and 45 wt.%), resulting in 16 simulation cases. The second group repeated the same configurations using Al_2O_3 particles, producing an additional 16 simulations. The third group investigated hybrid SiC–Al_2O_3 systems using particle mixing ratios of 9:1, 7:3, 3:7, and 1:9 while maintaining the same particle sizes and filler loadings, resulting in a further 64 simulation cases. In total, 96 simulation conditions were initially considered.

To reduce computational requirements, selected representative cases were analysed. For the first two groups, only the minimum and maximum particle sizes were simulated, resulting in eight simulations per material system. For the hybrid systems, one particle size with two selected filler loadings was investigated for all mixing ratios, resulting in eight additional simulations. Consequently, a total of 24 simulations were completed.

5.5.3 Material Properties

The material properties used in the ANSYS Workbench simulations were determined using the constituent weight fractions within the composite layer. For example, in the case of a 5 wt.% filler loading with a SiC_2O_3 ratio of 10:0, the composite consisted of 95 wt.% epoxy resin and 5 wt.% SiC, with no Al_2O_3 content present. The densities of epoxy resin, silicon carbide, and aluminium oxide were assumed to be 1150 kg/m³,

3200 kg/m³, and 3950 kg/m³, respectively, based on values reported in the literature. The effective composite density was subsequently calculated using the rule of mixtures according to the corresponding constituent weight fractions.

Using the weight fractions, the following calculation was done to find the density of the composite layer, using the inverse rule of mixtures as shown in equation 22.

$$\rho_{composite} = \frac{1}{\left(\frac{\omega_{epoxy}}{\rho_{epoxy}} + \frac{\omega_{SiC}}{\rho_{SiC}} + \frac{\omega_{Al_2O_3}}{\rho_{Al_2O_3}}\right)}$$

Equation 22

Where ω_i is the weight fraction of each material and ρ_i is the density of each material.

To calculate the specific heat constant pressure, the specific heat capacity C_p Values were assumed for each material to be 1150, 750, and 880 °C for epoxy, SiC and Al_2O_3 , respectively.

These were put into the equation 23 to calculate the C_p for the composite layer, using the mass-weighted rule of mixtures:

$$C_{p,Composite} = \omega_{epoxy}C_{p,epoxy} + \omega_{SiC}C_{p,SiC} + \omega_{Al_2O_3}C_{p,Al_2O_3}$$

Equation 23

The thermal conductivity calculation has a few more steps. Firstly, the calculation involves volume fractions instead of weight fractions. To achieve this, a conversion formula, as shown in equation 24, is used to go from weight fractions to volume fractions

$$V_i = \frac{\frac{\omega_i}{\rho_i}}{\frac{\omega_{epoxy}}{\rho_{epoxy}} + \frac{\omega_{SiC}}{\rho_{SiC}} + \frac{\omega_{Al_2O_3}}{\rho_{Al_2O_3}}}$$

Equation 24

Where V_i is the volume fraction for each material. Next, the filler conductivity was calculated for the particle sizes, using equation 25.

$$k_{size} = \frac{k}{1 + \frac{4kR_{int}}{d}}$$

Equation 25

Where k is the bulk filler conductivity, R_{int} is the interfacial thermal resistance and d was the particle diameter. R_{int} was assumed to be $1e^{-8}$as used in previous studies [198], [199]. This was done to correct the thermal conductivity values for SiC and Al_2O_3. Next the Volume Fraction Filler Conductivity is calculated using equation 26.

$$k_f = \left(\frac{V_{SiC}}{V_f}\right) k_{SiC} + \left(\frac{V_{Al_2O_3}}{V_f}\right) k_{Al_2O_3}$$

Equation 26

Where $V_f = V_{SiC} + V_{Al_2O_3}$. With this k_f value in mind, the $k_{composite}$ value can be calculated using the Maxwell-Eucken model formula in which the k value for epoxy, SiC, and Al_2O_3 were used as 0.2, 120, and 30 W/mK, respectively, as in equation 27.

$$\boxed{k_{ME,composite} = k_{epoxy}\left(\frac{k_f + 2k_m + 2V_f(k_f - k_m)}{k_f + 2k_m - V_f(k_f - k_m)}\right)}$$

Equation 27

The Maxwell-Eucken model was used due to the composite layer being treated as a continuous epoxy matrix, which contains dispersed ceramic (SiC and Al_2O_3) particles [200]. This calculation is suitable for first-order analytical estimates for particle-filled composites where the filler is assumed to be evenly distributed throughout the composite layer. This allows for effective thermal conductivity values to be estimated using the previously calculated filler volume fractions and filler conductivity.

5.6 Results and discussion

5.6.1 Calculating the thermal conductivity using experimental data

To investigate the influence of material properties on thermal conductivity, two ceramic fillers, silicon carbide (SiC) and aluminium oxide (Al_2O_3), were evaluated. Figure 2a presents the thermal conductivity values of the composites containing these fillers at different particle sizes. As shown in Figure 5.2a, SiC exhibited consistently higher thermal conductivity than Al_2O_3 across all investigated particle sizes. In addition, an increase in particle size resulted in enhanced thermal conductivity for both materials. Specifically, as the particle size increased from 4.5 to 185 μm, the thermal conductivity of the Al_2O_3-filled samples increased from 0.229 to 0.654 W/mK, while the SiC-filled samples showed an increase from 0.302 to 0.954 W/mK.

Figure 5.2b illustrates the infrared (IR) camera temperature measurements for the Al_2O_3-filled samples with varying particle sizes. As observed, the sample containing 185 μm particles maintained its temperature for approximately 300 s, which was nearly twice as long as the sample containing 4.5 μm particles and 5 times longer than samples containing nanoparticles. Furthermore, Figure 5.2c presents the IR camera measurements for the SiC-filled samples with different particle sizes. A similar trend was observed, where samples containing larger particles retained heat for a longer duration compared to those containing smaller particles, where a sample including a 185 μm particle could last almost 7 times longer than the samples including nanoparticles. In addition, Figure 5.2d represents the material removal during the grinding process. The material removal was measured based on the weight difference of the substrate after each grinding test, and was plotted as shown in Figure 2d. Based on the results, the backing material containing higher particle sizes removed more material from the substrate surface, where for Al2O3, the material removal increased from 0.012 to 0.07 g for 4.5 to 185 μm, respectively. This value for SiC was higher, starting at 0.047 to 0.095 g for 4.5 and 185 μm particles, respectively. The black circle in graphs 2b and c indicates the failure point of the disc during the process, whereas no failure was detected for the samples with higher particle sizes, which could be attributed to the higher lifetime of the samples. Moreover, the

samples containing nanoparticles removed the material no more than 0.008 and 0.0094 g for Al2O3 and SiC, respectively, and they failed roughly after 50 seconds in the process.

The inherently higher thermal conductivity of SiC compared to Al_2O_3 can be attributed to its stronger covalent bonding, higher phonon velocities, reduced phonon scattering, and relatively simpler crystal structure [201]. In ceramic materials, thermal conductivity is strongly dependent on the crystal structure and the phonon mean free path. An increased number of structural defects leads to enhanced phonon scattering, thereby reducing thermal conductivity [202]In contrast, aluminium oxide is a typical dielectric material in which heat transport occurs predominantly via phonon–phonon interactions. Its crystal structure consists of a distorted hexagonal close-packed (HCP) arrangement of oxygen ions, with aluminium ions occupying two-thirds of the octahedral interstitial sites. This structural complexity introduces lattice distortion and asymmetry, resulting in enhanced phonon scattering due to the distorted lattice geometry, partial occupancy of interstitial sites, and the mixed ionic–covalent bonding nature [203]. Consequently, these factors reduce the phonon mean free path and limit heat transfer efficiency. Conversely, silicon carbide possesses a more ordered and strongly covalent crystal structure with high bond stiffness, facilitating phonon propagation with higher velocities and fewer scattering events. As a result, thermal transport in SiC is significantly more efficient. Therefore, the lower thermal conductivity of Al_2O_3 compared to SiC can be attributed to its structural distortion, complex lattice arrangement, and increased phonon scattering, all of which hinder effective heat conduction.

In addition, increasing particle size contributes to enhanced thermal conductivity in both materials. Larger particle sizes improve the contact between adjacent particles [204], thereby facilitating heat transfer pathways. Thermal conductivity is also influenced by interfacial thermal resistance at grain boundaries. As particle size increases, the number of grain boundaries per unit volume decreases, leading to reduced phonon scattering and an increased phonon mean free path.

Figure 5.3 illustrates SEM images of 185 μm Al_2O_3 particles dispersed in an epoxy matrix at 45 wt%. As shown, the particles are randomly distributed across the surface and exhibit significant agglomeration. Such agglomeration reduces thermal conductivity by decreasing the effective phonon mean free path. In contrast,

Figure 5.4 presents SiC particles under identical conditions. The particles appear more uniformly distributed, with minimal aggregation, which facilitates more effective heat transfer pathways. The SEM analysis indicates that SiC particles are well-dispersed and exhibit angular, faceted morphologies, whereas Al_2O_3 particles show pronounced agglomeration and clustering. The absence of large agglomerates in SiC promotes the formation of continuous heat conduction pathways and reduces interfacial thermal resistance. In contrast, the agglomerated structure of Al_2O_3 introduces numerous grain boundaries and voids, which enhance phonon scattering and impede heat transfer. Therefore, the higher thermal conductivity observed in SiC is primarily attributed to its improved dispersion and reduced interfacial resistance, rather than particle alignment.

In addition, Figure 5.5 illustrates the powder flowability test result of the SiC and Al_2O_3 particles. Powder flowability plays a critical role in determining the effective thermal conductivity of particle-filled composites. Improved flowability enhances particle packing, dispersion uniformity, and interparticle contact, thereby reducing interfacial thermal resistance and phonon scattering. Conversely, poor flowability promotes agglomeration and porosity, which disrupts heat conduction pathways and lowers thermal conductivity. Firstly, by decreasing the particle size, the basic flowability energy (BFE) decreases, in which the average BFE decreases from 374.19 mJ for aluminium oxide to 303.82 mJ for silicon carbide. The results indicate that SiC particles exhibit a greater tendency to distribute uniformly along the surface compared to Al_2O_3. This observation is consistent with the powder flowability test results, which demonstrated superior flow characteristics for the SiC powders. Improved flowability promotes more uniform spreading during processing, resulting in a more homogeneous particle distribution across the surface.

Such uniformity is critical for thermal transport, as it facilitates the formation of continuous and well-connected pathways for phonon propagation. In contrast, poorer flowability, as observed for Al_2O_3, can lead to particle agglomeration and non-uniform coverage, thereby introducing additional phonon scattering sites and thermal resistance. Consequently, the enhanced distribution of SiC particles contributes to more efficient heat transfer, leading to higher thermal conductivity, as evidenced in Figure 5.2.

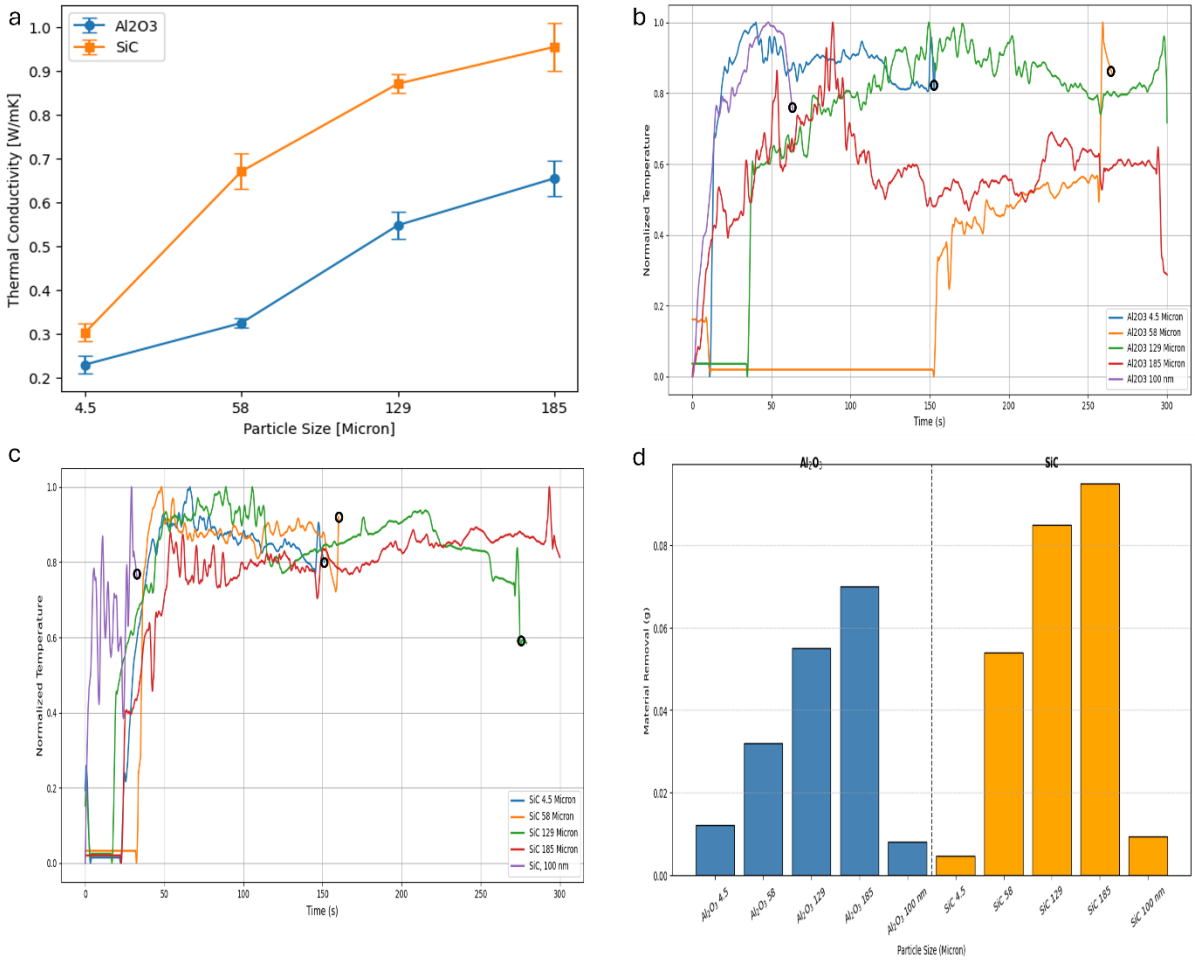


Figure 5.2 Thermal conductivity measurement of the SiC and Al_2O_3 5 wt% in various particle sizes. b) IR camera normalised temperature vs time for various sizes of Al_2O_3, c) IR camera normalised temperature vs time for various sizes of SiC, and d) material removal for SiC and Al2O3 in different particle sizes

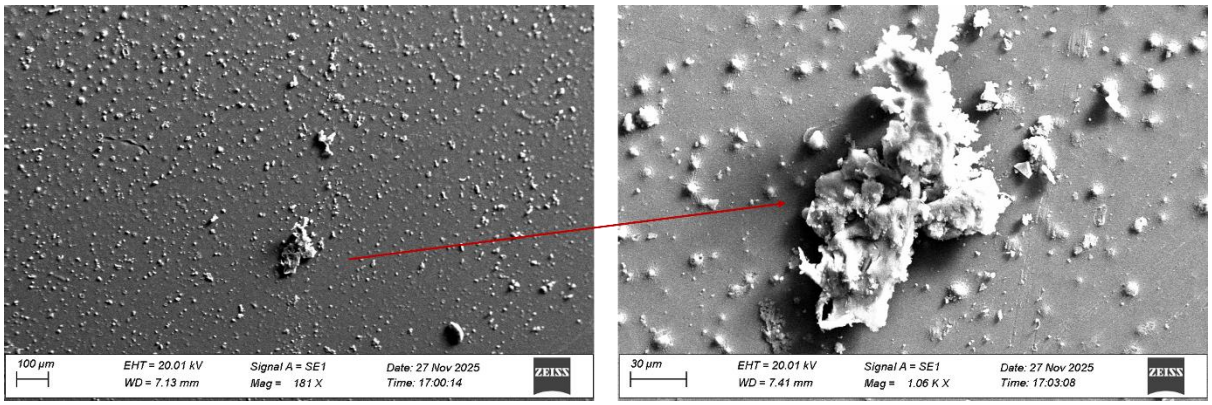


Figure 5.3 . SEM images of 185µm Al_2O_3 particles at 45w% into epoxy resin a) wider surface, and b) high magnification of the pointed area

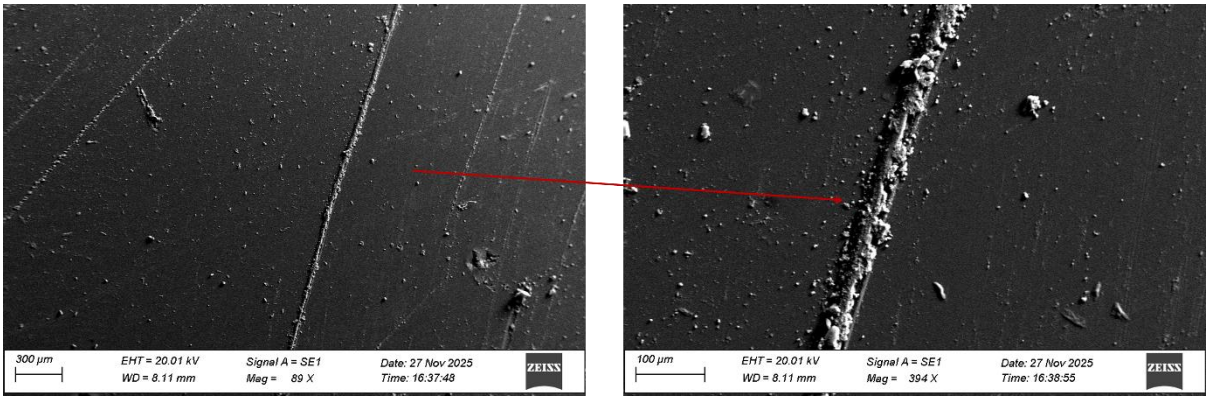


Figure 5.4 SEM images of 185µm SiC particles at 45w% into epoxy resin a) wider surface, and b) high magnification of the pointed area

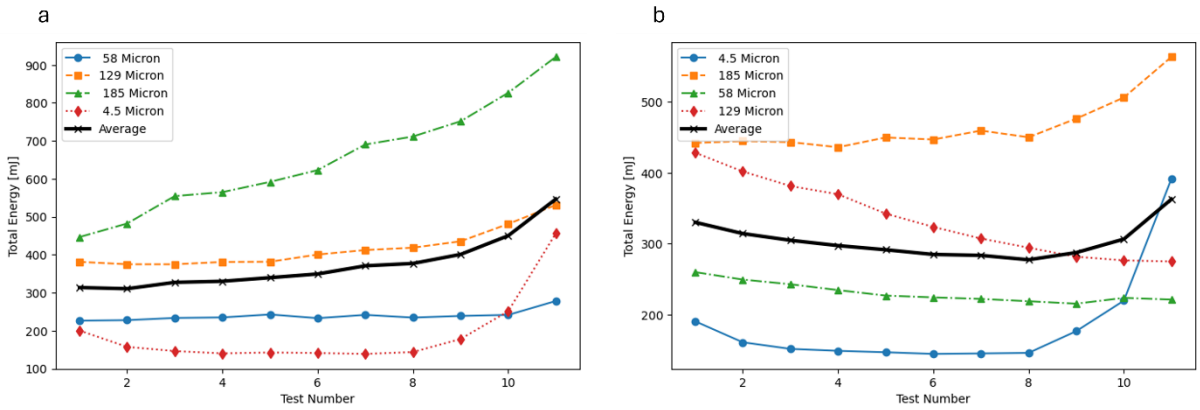


Figure 5.5 Powder flowability test result for a) Aluminium oxide and b) silicon carbide in different particle sizes

In addition, four different particle loadings (5, 15, 30, and 45 wt.% of the total system) were investigated to evaluate the effect of particle loading on the thermal conductivity of the resulting coatings. Figures 5.6a and b present the thermal conductivity measurements of samples containing different particle loadings for both SiC and Al_2O_3 particles. For both materials, the thermal conductivity increased with increasing micron-sized particle loading, while larger particle sizes at the same loading also resulted in higher thermal conductivity values. For Al_2O_3, as shown in Figure 6a and b, increasing the particle loading from 5 to 45 wt.% increased the thermal conductivity from 0.229 to 0.68 W/mK for the 4.5 µm particles, whereas for the 185 µm particles, the thermal conductivity increased from 0.654 to 1.08 W/mK. These results indicate that increasing the micron-sized particle loading enhanced the thermal conductivity by approximately 1.65 times. In contrast, SiC exhibited a greater enhancement in thermal conductivity with increasing micron-sized particle loading, where the thermal conductivity increased from 0.3 to 1.12 W/mK for the 4.5 µm particles and from 0.954 to 2.0 W/mK for the 185 µm particles. On the other hand, however, increasing the particle loading for nano-sized particles decreased the thermal conductivity. The higher effective thermal conductivity observed in systems containing micron-sized particles, compared with their nano-sized counterparts at equivalent loadings, can be attributed to differences in heat transport mechanisms governed

by interfacial effects, particle connectivity, and phonon scattering. Although nanoparticles offer a significantly higher surface-area-to-volume ratio, this advantage is offset by the corresponding increase in interfacial thermal boundary resistance, which becomes the dominant limiting factor for heat transfer. In such systems, heat must traverse a large number of particle–matrix and particle–particle interfaces, where phonon scattering is significantly enhanced, thereby reducing the overall thermal transport efficiency. In addition, IR camera results in Figure 6c and d further proved this behaviour, where the samples containing 45 wt% loading for both materials lasted nearly 300 seconds, whereas the samples with lower particle loadings, 5 wt%, failed after around 180 and 165 seconds for Al_2O_3 and SiC, respectively.

In contrast, micron-sized particles facilitate more effective formation of thermally conductive networks due to improved particle–particle contact and reduced interfacial density along the heat transfer pathways. This promotes the establishment of more continuous percolation structures, which enhance bulk thermal conductivity at higher loadings. Furthermore, nanoparticles are more prone to agglomeration driven by their high surface energy, leading to non-uniform dispersion, increased porosity, and the formation of thermally resistive voids within the matrix. Such structural heterogeneities further impede heat conduction. Additionally, phonon mean free path limitations and boundary scattering effects are more pronounced at the nanoscale, further reducing intrinsic thermal transport efficiency.

Overall, the improved performance of micron-sized SiC and Al_2O_3 particles can be attributed to their ability to form more stable conductive pathways with reduced interfacial resistance and improved packing efficiency, thereby outweighing the potential benefits associated with increased surface area in nanoparticulate systems. Overall, the thermal conductivity increased by approximately 2.1 times when the particle loading was increased to 45 wt.%.

SEM images were obtained to further investigate the morphological changes in the samples with increasing particle loading. As shown in Figure 5.6, increasing the particle loading increased the surface area covered by micron-sized particles for both materials, resulting in the formation of more continuous thermally conductive networks within the coating matrix. In addition, a more uniform particle distribution was observed at higher particle loadings, which facilitated phonon transport pathways and consequently

enhanced the thermal conductivity. This behaviour can be attributed to the reduced interparticle distance at higher loadings, allowing heat to transfer more efficiently through particle-to-particle contact. However, some particle agglomeration was also observed at higher particle loadings, which may have restricted homogeneous heat transfer and limited the thermal conductivity from reaching even higher values. In contrast, increasing the loading of nano-sized particles results in more pronounced agglomeration and the formation of localised clusters, which hinder effective heat transfer pathways and consequently lead to a reduction in the thermal conductivity of the samples.

Furthermore, the effect of combining Al_2O_3 and SiC particles on the thermal conductivity was investigated using four different mixing ratios of 1:9, 3:7, 7:3, and 9:1. The corresponding results are presented in Figure 8, together with the SEM images obtained for the 9:1 SiC-to-Al_2O_3 sample. The results demonstrate that increasing the SiC content in the composite coating led to a progressive increase in thermal conductivity, reaching a maximum value of 2.78 W/mK for the 9:1 SiC-to-Al_2O_3 ratio. This value was approximately 1.39 times higher than that obtained for the coating containing only SiC particles. In contrast, samples with lower SiC content exhibited comparatively lower thermal conductivity values.

The enhanced thermal conductivity observed in the mixed-particle systems can be attributed to a synergistic interaction between SiC and Al_2O_3 particles. The incorporation of particles with differing sizes and intrinsic thermal properties appears to improve packing efficiency and to promote the formation of more continuous thermally conductive pathways within the coating matrix. In particular, the high intrinsic thermal conductivity of SiC contributes substantially to heat transfer, while the presence of Al_2O_3 particles may assist in reducing interfacial voids and enhancing particle-to-particle connectivity. The SEM micrographs further support these observations, revealing a relatively uniform particle distribution, which is favourable for phonon transport throughout the coating. In addition, the Al_2O_3 particles are observed to be evenly distributed across the surface, while the SiC particles exhibit a preferential alignment, consistent with the behaviour reported previously in Figures 5.3 and 5.4. Overall, these results indicate that particle hybridisation is an effective strategy for improving the thermal conductivity of the developed coatings. The temperature of the backing material of the abrasive disc was also recorded as a function of time for different

particle mixing ratios, as shown in Figure 5.8d. As can be seen, the disc with a backing layer containing a SiC:Al_2O_3 ratio of 9:1 exhibited the longest operational lifetime compared with the other configurations. This improved performance can be directly linked to the enhanced thermal conductivity observed for this composition. Improved heat dissipation leads to lower temperatures at the backing sheet during operation, thereby reducing thermal degradation and resulting in extended disc service life.

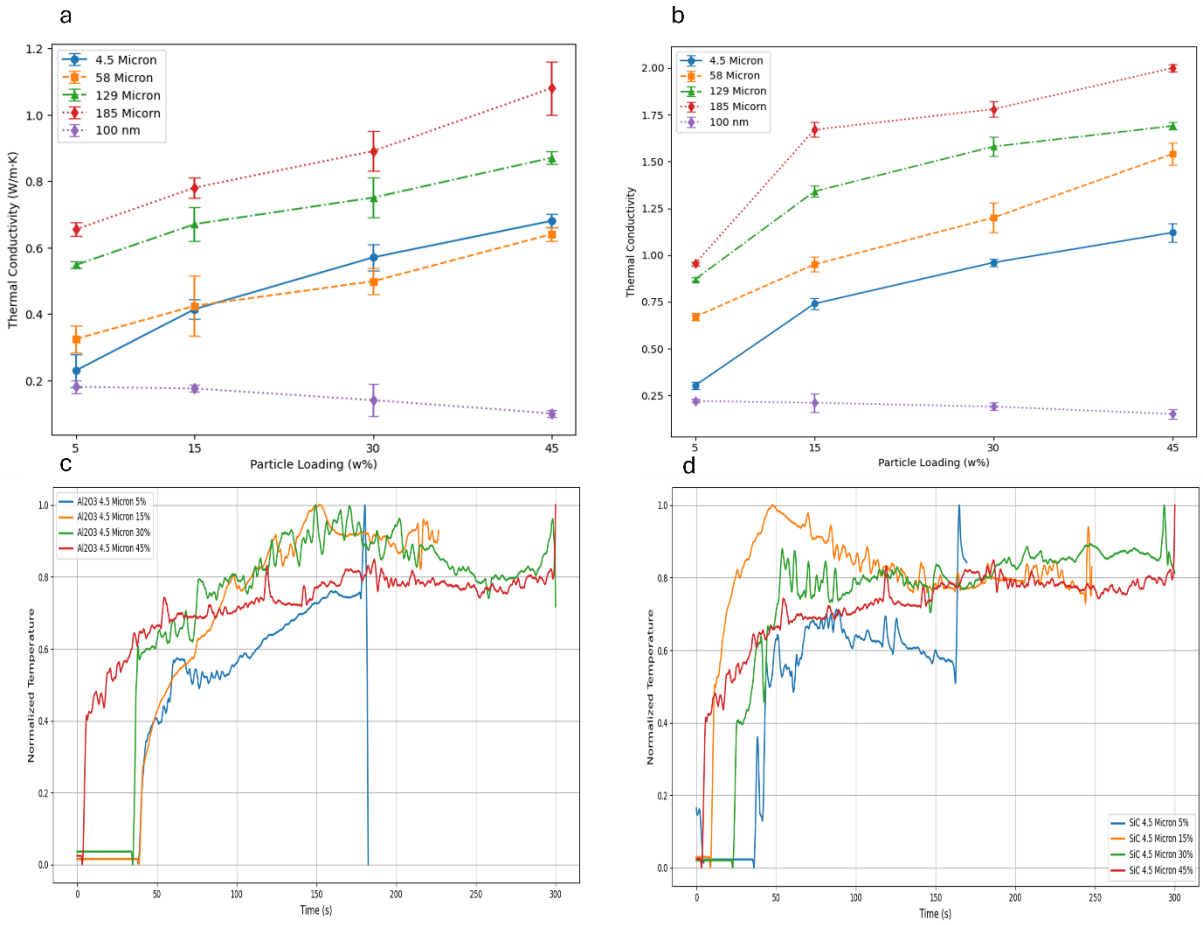


Figure 5.6 Thermal conductivity as a function of particle loading for a) Al_2O_3 and b) SiC and IR-camera normalised temperature recording for c)Al_2O_3 4.5 Micron at different particle loadings, and d)SiC 4.5 Micron at different particle loadings

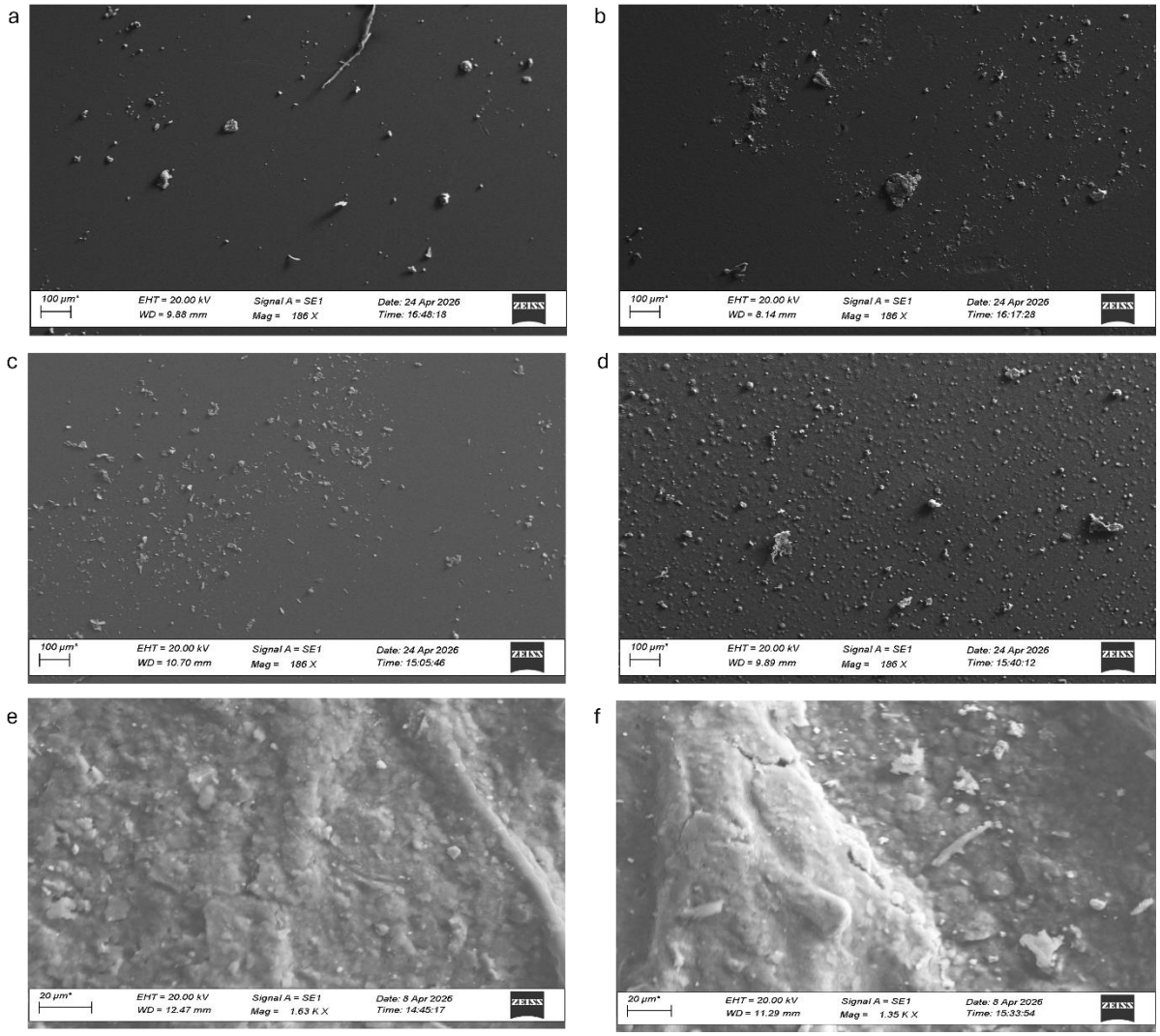


Figure 5.7 SEM images of different particle loading alongside the surface of the deposited coating of a, b) Al_2O_3 5%, Al_2O_3 45%, c, d)SiC 5%, SiC 45% and e, f) 100 nm SiC 5%, SiC 45%.

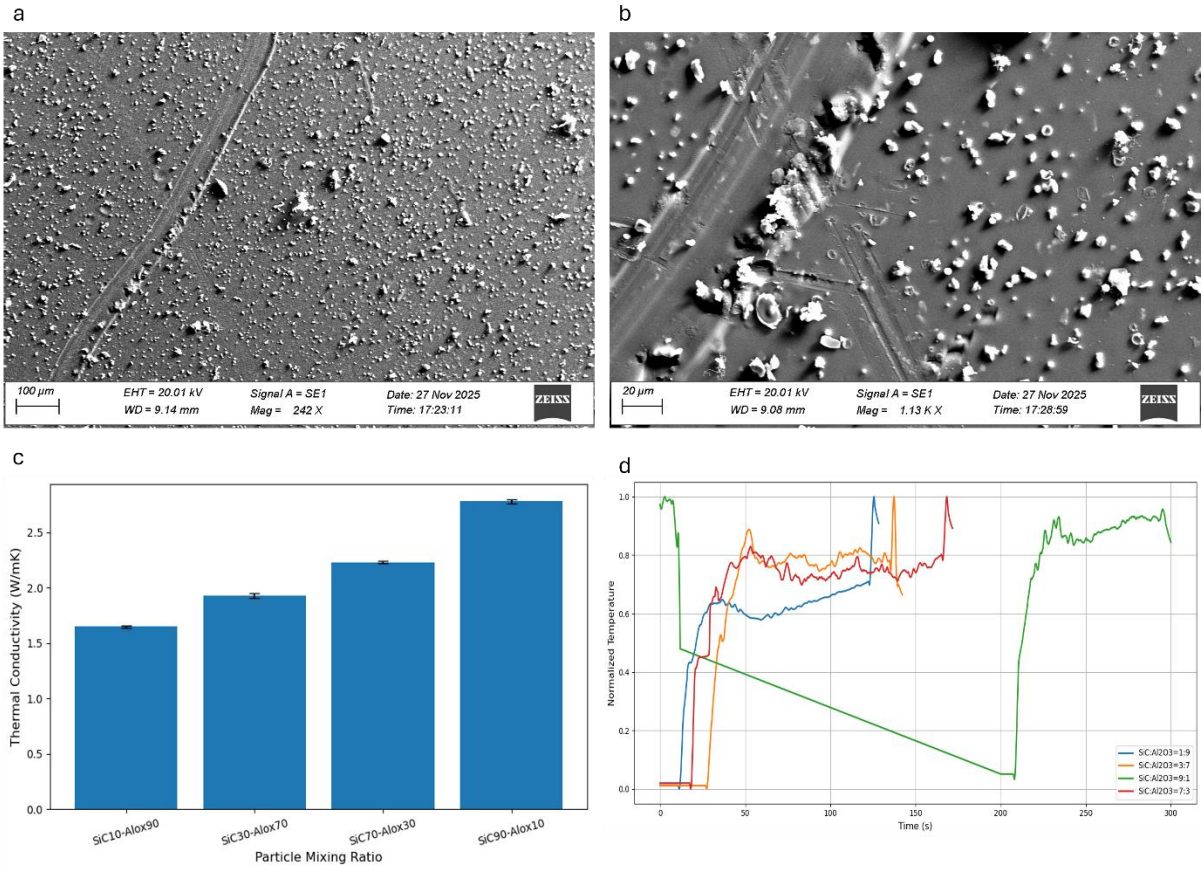


Figure 5.8 SEM images of the sample prepared by the mixing ratio of 9:1 for a) SiC:Al_2O_3 , b) higher magnification, and c) related thermal conductivity measurement for the various mixing ratios, and d) Normalised IR-camera temperature recording

5.6.2 Calculating the thermal conductivity using Analytical and FEA models

Using Equation 27, the analytical thermal conductivity values of the composite materials were calculated, and the corresponding results are presented in Table 5.4. To reduce computational effort while still capturing the overall behaviour of the system, only the minimum and maximum particle sizes were considered in the analytical calculations. As shown in Table 5.4, increasing the particle size of both SiC and Al_2O_3 fillers resulted in an increase in the predicted thermal conductivity of the composite material.

For SiC-filled composites, the thermal conductivity increased from 0.209 to 0.376 W/mK, while for Al_2O_3 -filled composites, the thermal conductivity increased from 0.207 to 0.339 W/mK. This behaviour is consistent with the experimental observations, where larger particle sizes also led to improved thermal conductivity. The increase in thermal conductivity with particle size can be attributed to the reduction in interfacial area between the filler particles and polymer matrix, thereby decreasing phonon scattering and interfacial thermal resistance within the composite. Furthermore, the analytical results demonstrated that SiC-filled composites exhibited higher thermal conductivity values compared to Al_2O_3 -filled composites under similar conditions. This trend also agrees with the experimental findings and is primarily due to the intrinsically higher thermal conductivity of SiC relative to Al_2O_3 . In addition, increasing the filler loading resulted in a corresponding enhancement in thermal conductivity. For SiC composites, the thermal conductivity increased from 0.211 to 0.376 W/mK, whereas Al_2O_3 -based composites increased from 0.209 to 0.339 W/mK as the filler content increased. This behaviour is attributed to the formation of more continuous thermally conductive pathways within the epoxy matrix as the concentration of ceramic particles increased. Similarly, increasing the SiC:Al_2O_3 ratio led to higher thermal conductivity values, further confirming the dominant contribution of SiC to heat transfer within the composite system.

Although the analytical model successfully predicted the same overall trends observed experimentally, some discrepancies were identified between the analytical and measured thermal conductivity values. These differences may be attributed to several simplifying assumptions inherent in the analytical model. The Maxwell–Eucken approach assumes ideal particle dispersion, uniform particle geometry, and perfect interfacial bonding between the filler and epoxy matrix. In practice, however, experimental samples may contain particle agglomeration, voids, non-uniform particle distribution, and imperfect filler–matrix interfaces as was obsrved in the experimental results, all of which can significantly influence heat transfer behaviour. Additionally, the analytical model assumes constant material properties and simplified interfacial thermal resistance values, whereas the actual composite microstructure is considerably more complex. Experimental uncertainties associated with sample fabrication, curing conditions, and thermal conductivity measurements may also contribute to the observed deviations between analytical predictions

and experimental results[205].

Table 5.4 Analytical calculation of the thermal conductivity for different sample size, loading and ratio

Run	Particle Size (µm)	Percentage wt%	Ratio (SiC)	Thermal Conductivity (W/mK)
1	4.5	5	10	0.209
2	4.5	15	10	0.230
3	4.5	30	10	0.273
4	4.5	45	10	0.339
5	185	5	10	0.211
6	185	15	10	0.237
7	185	30	10	0.292
8	185	45	10	0.376
9	4.5	5	0	0.207
10	4.5	15	0	0.224
11	4.5	30	0	0.258
12	4.5	45	0	0.310
13	185	5	0	0.209
14	185	15	0	0.230
15	185	30	0	0.273
16	185	45	0	0.339
17	4.5	5	9	0.208
18	4.5	5	7	0.208

19	4.5	5	3	0.207
20	4.5	5	1	0.207
21	4.5	45	9	0.337
22	4.5	45	7	0.331
23	4.5	45	3	0.320
24	4.5	45	1	0.314

Moreover, for FEA analysis, equation 28 was used and the total runtime of 300 seconds was investigated.

$$k_{total} = \frac{q'' * t_{total}}{\Delta T}$$

Equation 28

Where k_{total} is the thermal conductivity (W/mK) of the three-layered model; t_{total} is the total thickness (m); q" is the average directional heat flux ($\frac{W}{m^2}$) in the y direction after 300s; ΔT is the difference in temperature between the top of the composite layer and the bottom of the grinding disk after 300s and the results are presented in Table 5. As shown in Table 5.5, increasing both the particle size and particle loading resulted in an increase in the thermal conductivity of the composite material. For silicon carbide (SiC)-filled composites, the thermal conductivity increased from 0.596 to 0.988 W/mK, while Al_2O_3 -filled composites exhibited an increase from 0.594 to 0.915 W/mK. These FEA predictions showed good agreement with the experimentally measured thermal conductivity values while maintaining the same overall trends observed experimentally.

In addition, increasing the SiC content within the hybrid filler system further enhanced the thermal conductivity of the composite. The highest thermal conductivity value of 0.905 W/mK was achieved for the SiC:Al_2O_3 ratio of 9:1, indicating the superior contribution of SiC towards heat transfer within the epoxy matrix due to its inherently higher thermal conductivity compared to Al_2O_3 .

Compared to the analytical model, the FEA results demonstrated a smaller deviation from the experimental measurements. This improved agreement can be attributed to the ability of the finite element model to more accurately represent the composite geometry, heat transfer pathways, and boundary conditions within the material system. Unlike simplified analytical models such as the Maxwell–Eucken approach, the FEA model accounts for spatial heat conduction through the composite structure and can better capture the influence of filler distribution and interaction on thermal transport behaviour. Furthermore, the numerical simulation incorporates realistic thermal boundary conditions and effective material properties, thereby reducing the level of idealisation present in the analytical calculations. As a result, the FEA approach provides a more representative approximation of the actual thermal behaviour of the composite materials, leading to closer agreement with the experimental results.

Nevertheless, minor discrepancies between the FEA and experimental results still remain. These differences may arise from factors not fully captured in the numerical model, including particle agglomeration, void formation, imperfect interfacial bonding, non-uniform filler dispersion, and variations introduced during composite fabrication and experimental thermal conductivity measurements. Figure 5.9 further illustrates the variation between the three different approaches used to determine the thermal conductivity of the composite material, namely the FEA, analytical model, and experimental measurements. It can be observed that the thermal conductivity values predicted by the FEA model show closer agreement with the experimental results when compared to the analytical model. The reduced variance between the FEA and experimental results indicates that the numerical simulation is capable of more accurately capturing the heat transfer behaviour within the composite system. In contrast, the analytical model demonstrates comparatively larger deviations from the experimental data. This discrepancy is primarily due to the assumptions and idealised conditions employed in analytical calculations, including uniform particle dispersion and simplified thermal transport mechanisms. Although the analytical approach provides a rapid estimation of thermal conductivity trends, the FEA model offers a more realistic representation of the composite microstructure and thermal behaviour.

Table 5.5 Thermal Conductivity measurement of the composite material using FEA

Run	Particle Size (µm)	Percentage (wt%)	Ratio (SiC)	Thermal Conductivity (W/mK)
1	4.5	5	10	0.596
2	4.5	15	10	0.651
3	4.5	30	10	0.756
4	4.5	45	10	0.911
5	185	5	10	0.604
6	185	15	10	0.669
7	185	30	10	0.799
8	185	45	10	0.988
9	4.5	5	0	0.594
10	4.5	15	0	0.637
11	4.5	30	0	0.723
12	4.5	45	0	0.850
13	185	5	0	0.598
14	185	15	0	0.652
15	185	30	0	0.758
16	185	45	0	0.915
17	4.5	5	9	0.598
18	4.5	5	7	0.597

19	4.5	5	3	0.595
20	4.5	5	1	0.594
21	4.5	45	9	0.905
22	4.5	45	7	0.894
23	4.5	45	3	0.870
24	4.5	45	1	0.857

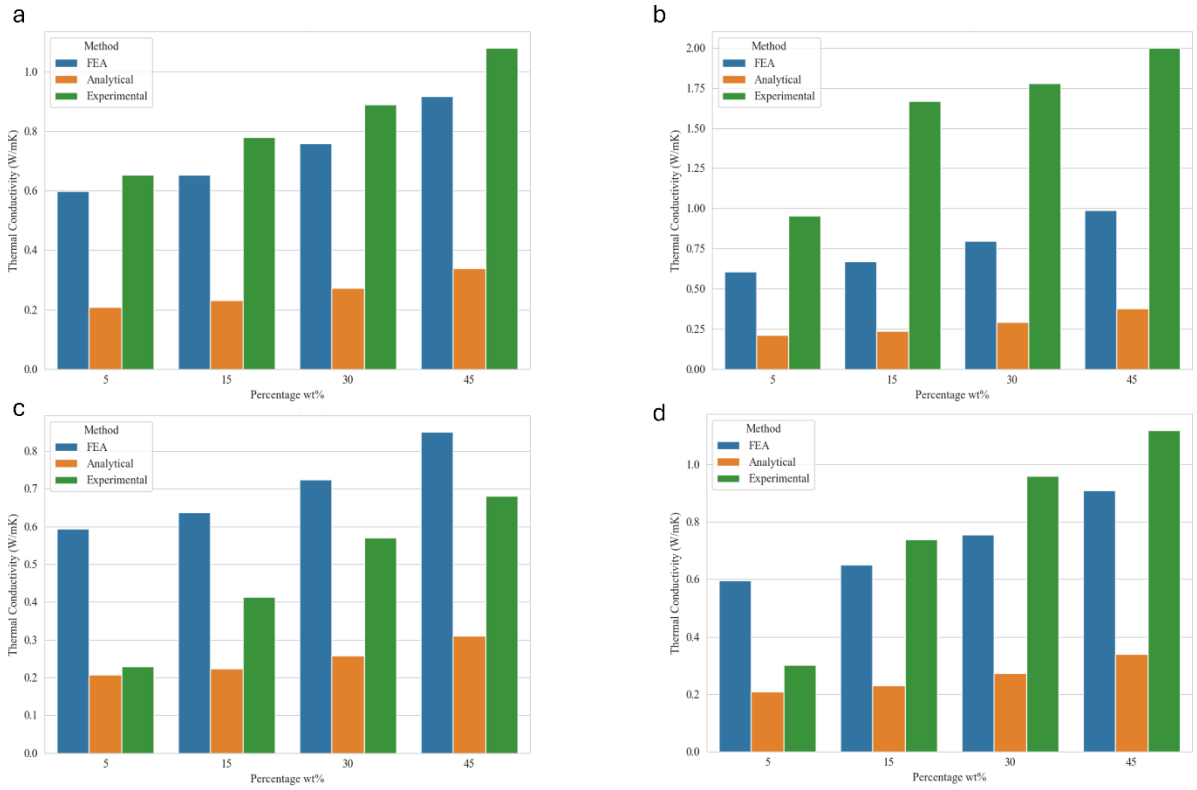


Figure 5.9 a comparison between different approaches for thermal conductivity measurements with different particle loadings, where a) Aluminium oxide particle size 185, b) Silicon carbide particle size 185, c) Aluminium oxide particle size 4.5, and d) Silicon carbide particle size 4.5 µm

5.7 Conclusion

In conclusion, based on the findings presented in this study, the incorporation of ceramic fillers significantly enhanced the thermal conductivity of epoxy-based abrasive composites. Among the investigated materials, silicon carbide (SiC) consistently demonstrated superior thermal performance compared with aluminium oxide (Al_2O_3), owing to its higher intrinsic thermal conductivity, improved phonon transport characteristics, and more uniform particle dispersion within the epoxy matrix. Increasing both the particle size and filler loading led to substantial improvements in thermal conductivity, with the highest value of approximately 2.78 W/mK achieved for the hybrid composite containing a 9:1 SiC-to-Al_2O_3 ratio at high filler loading. In contrast, nano-sized particles exhibited reduced thermal performance at higher loadings due to severe agglomeration, increased interfacial thermal resistance, and enhanced phonon scattering. SEM observations and powder flowability analyses further confirmed that micron-sized SiC particles promoted the formation of continuous thermally conductive pathways and reduced interparticle resistance, resulting in more efficient heat dissipation during abrasive operations.

The infrared thermal imaging experiments demonstrated that composites with higher thermal conductivity exhibited improved thermal stability and prolonged operational lifetime during grinding applications. Samples containing larger micron-sized SiC particles retained heat for significantly longer durations and reduced thermal accumulation at the backing layer, thereby minimising thermal degradation and extending service life. Furthermore, hybridisation of SiC and Al_2O_3 particles produced a synergistic effect by improving particle packing density and filler connectivity within the epoxy matrix. The enhanced thermal behaviour of the hybrid systems indicates that combining fillers with different morphologies and intrinsic properties is an effective strategy for optimising thermal management in abrasive coatings and grinding disc backings. The combined results and conclusion are presented in Table 5.6.

Table 5.6 Conclusion of the results in three different aspects including thermal conductivity, temperature response, and integrated conclusion.

Parameter	**Thermal Conductivity Analysis**	**Temperature Response Analysis**	**Integrated Conclusion**
Effect of Filler Loading	Thermal conductivity increases progressively with increasing filler content, from approximately 1.65 W/m·K for SiC:Al2O3 1:9 to 2.78 W/m·K for SiC:Al2O3 9:1	Higher filler loading and adding more SiC content to the mixing ratio, results in a faster temperature rise and improved heat transfer efficiency.	Increasing filler content enhances thermal transport by forming more continuous heat-conduction pathways within the epoxy matrix.
Effect of Particle Mixing Ratio	Increasing the SiC fraction significantly improves thermal conductivity. The highest conductivity is observed for SiC:Al2O3 9:1.	Compositions with higher SiC content reach higher normalised temperatures more rapidly and maintain stable thermal behaviour.	Increasing the proportion of SiC and optimizing the SiC:Al_2O_3 mixing ratio significantly improves thermal conductivity and heat propagation efficiency.
Thermal Conductivity Trend	A clear monotonic increase in thermal conductivity is observed across all compositions as the SiC content increases.	Temperature profiles stabilise at higher normalised temperatures for SiC-rich samples.	The increase in thermal conductivity directly correlates with enhanced thermal response and heat-transfer capability, in which the higher thermal conductivity resulted in

			improving the disc durability.
Heating Response	Higher thermal conductivity suggests more efficient heat transport through the composite.	SiC:Al2O3 with the ratio of 1:9 exhibits the highest normalised temperature (~0.95), whereas SiC:Al2O3 with the ratio 9:1 shows the slowest heating rate and lowest final temperature.	Compositions with higher thermal conductivity exhibit faster heating rates and long durability.
Best Performing Composition	SiC:Al2O3 9:1 demonstrates the highest thermal conductivity (~2.78 W/m·K).	SiC:Al2O3 9:1 exhibits the fastest and most stable thermal response.	High SiC content maximises thermal conductivity, while optimised SiC/Al_2O_3 hybrid compositions provide excellent transient heat-transfer performance.

Analytical modelling and FEA successfully predicted the overall experimental trends, confirming that increasing particle size, filler loading, and SiC content enhances thermal conductivity. Although the analytical Maxwell–Eucken model provided useful first-order estimations, the FEA simulations showed closer agreement with the experimental results because they more accurately represented realistic heat transfer pathways and thermal boundary conditions within the composite structure. Minor discrepancies between simulations and experiments were primarily attributed to particle agglomeration, void formation, and imperfect interfacial bonding that were not fully captured in the models. This study demonstrates that carefully engineered hybrid ceramic-filled epoxy composites can be designed to provide high thermally

conductive long lifetime abrasive materials with improved durability, thermal stability, and operational efficiency for demanding industrial applications.

6 Chapter 6

Conclusion

This PhD research has demonstrated a comprehensive approach to the synthesis, characterisation, optimisation, and application of silicon carbide (SiC)-based materials, spanning the production of SiC nanoparticles through pulsed laser ablation in liquid (PLAL), the tailoring of nanoparticle colloids for additive manufacturing applications, and the development of thermally conductive ceramic-filled epoxy composites for abrasive and thermal management systems. By integrating advanced nanoparticle fabrication techniques with composite material engineering, this work establishes a coherent pathway from nanomaterial synthesis to functional engineering applications.

The first major contribution of this research was the successful synthesis of silicon carbide nanoparticles (SiC NPs) using nanosecond pulsed laser ablation in liquid (PLAL) in deionised water. A systematic investigation of laser processing parameters, including laser fluence, scanning speed, and ablation time, demonstrated their significant influence on ablation efficiency, nanoparticle yield, particle size distribution, and colloidal stability. Under optimised processing conditions comprising a laser fluence of 7.5 J/cm², scanning speed of 0.5 m/s, and ablation time of 15 minutes, a maximum ablated mass of 1.8 mg and a mass productivity of 1.196 mg h^{-1} W^{-1} were achieved. The study revealed clear relationships between processing parameters and nanoparticle properties, with increasing laser fluence and processing duration resulting in higher nanoparticle concentrations, larger average particle sizes, and enhanced optical absorbance.

Comprehensive characterisation confirmed the successful fabrication of high-quality SiC nanoparticles. X-ray diffraction analysis verified the preservation of the cubic 3C-SiC crystal structure following laser ablation, while EDX measurements confirmed the elemental composition of silicon and carbon. FESEM and STEM observations revealed predominantly spherical nanoparticles with relatively uniform morphology, while DLS and image analysis provided complementary insights into particle size distributions. Optical characterisation further demonstrated that increasing nanoparticle size reduced the optical band gap, indicating size-dependent electronic properties. UV-Visible spectroscopy identified enhanced absorbance with increasing nanoparticle concentration and revealed a characteristic absorption peak near 195 nm associated with polyyne formation. FTIR analysis confirmed the dominant presence of SiC bonds while also indicating limited surface oxidation resulting from interactions with the aqueous environment during laser processing.

A further significant outcome of this work was the successful tailoring of SiC nanoparticle colloids for inkjet printing applications. Through systematic viscosity optimisation using glycerol-water mixtures, colloidal suspensions with viscosities up to 10.95 mPa·s were achieved, falling within the operational range required for commercial inkjet printing systems. This demonstrated the potential of PLAL-produced SiC nanoparticles as printable functional inks for advanced manufacturing applications. The ability to directly synthesise stable, surfactant-free nanoparticle colloids suitable for printing represents a promising route toward environmentally friendly and scalable fabrication of functional ceramic coatings and printed electronic devices.

Building upon the synthesis and characterisation of SiC materials, the second major component of this research focused on the development of thermally conductive ceramic-filled epoxy composites for abrasive applications. The incorporation of ceramic fillers was shown to significantly enhance thermal conductivity compared with unfilled epoxy systems. Among the investigated fillers, SiC consistently outperformed aluminium oxide (Al_2O_3), owing to its intrinsically higher thermal conductivity, superior phonon transport capability, and more favourable dispersion characteristics within the epoxy matrix. The experimental results demonstrated that increasing both filler loading and particle size substantially improved thermal conductivity, with the highest measured value of approximately 2.78 W/mK achieved for a hybrid composite containing a 9:1 SiC-to-Al_2O_3 ratio at high filler loading.

The thermal conductivity enhancements observed in the composite systems were strongly influenced by particle morphology, size, and filler distribution. Micron-sized SiC particles promoted the formation of continuous thermally conductive pathways throughout the epoxy matrix, reducing interparticle thermal resistance and facilitating more efficient heat transfer. In contrast, nano-sized particles exhibited increased agglomeration at higher loadings, resulting in elevated interfacial thermal resistance and enhanced phonon scattering that limited thermal conductivity improvements. SEM observations and powder flowability analyses provided direct evidence that larger particles enabled improved packing efficiency and connectivity between conductive filler networks, thereby maximising thermal transport performance.

Thermal imaging experiments further demonstrated the practical implications of improved thermal conductivity for abrasive applications. Composite systems containing larger SiC particles exhibited superior heat retention

and dissipation characteristics, resulting in reduced thermal accumulation within grinding disc backing materials. This enhanced thermal stability translated into reduced thermal degradation and potentially longer operational lifetimes under demanding grinding conditions. Furthermore, hybridisation of SiC and Al_2O_3 fillers generated a synergistic effect by improving packing density and connectivity within the composite microstructure, thereby further enhancing thermal performance. These findings demonstrate that strategic filler selection and hybridisation provide effective approaches for optimising thermal management in abrasive systems and other high-temperature engineering applications.

The research also successfully integrated experimental investigations with predictive modelling approaches. Analytical thermal conductivity predictions based on the Maxwell-Eucken model and finite element analysis (FEA) simulations both captured the overall trends observed experimentally. While the analytical model provided valuable first-order estimates, FEA simulations showed closer agreement with measured values due to their improved representation of realistic particle distributions, thermal boundary conditions, and heat transfer pathways within the composite structure. Remaining discrepancies between experimental and simulated results were primarily attributed to particle agglomeration, void formation, and imperfect interfacial bonding effects that were not fully represented within the computational models. These modelling efforts provide important validation of the underlying heat transfer mechanisms governing thermal conductivity enhancement in ceramic-filled polymer composites.

Taken together, the outcomes of this PhD research demonstrate the versatility and technological potential of silicon carbide across multiple length scales, from nanoscale particles to macroscale composite systems. The successful production of concentrated SiC nanoparticle colloids through PLAL, combined with the optimisation of colloidal properties for inkjet printing, establishes a foundation for advanced manufacturing and printed functional materials. Simultaneously, the development of thermally conductive SiC-based composite systems demonstrates the capability of engineered ceramic fillers to address critical thermal management challenges in abrasive and industrial applications.

The research contributes fundamental understanding of the relationships between processing parameters, material structure, and functional performance in SiC-based systems. Specifically, it establishes how laser

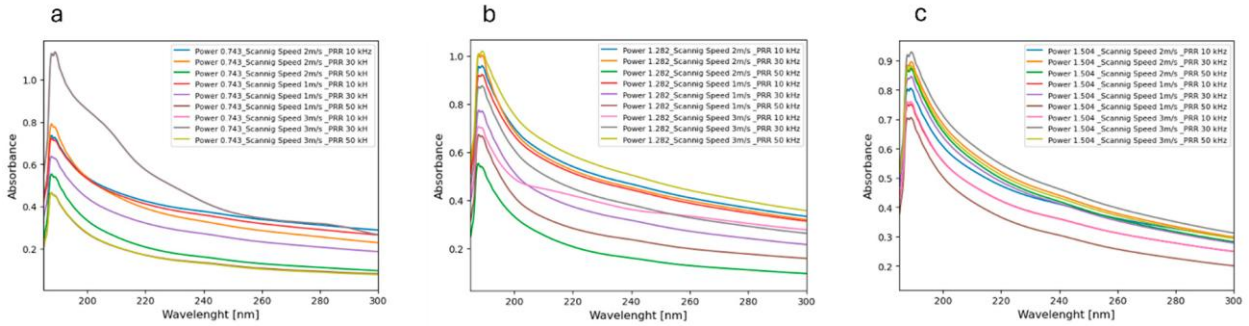
processing conditions govern nanoparticle formation and properties, how particle size and morphology influence thermal transport behaviour, and how hybrid filler architectures can be exploited to maximise composite thermal conductivity. These insights provide valuable guidance for the design and optimisation of future SiC-based materials and manufacturing technologies.

Future work should focus on extending the application of the developed SiC nanoparticle colloids through direct inkjet printing studies and evaluation of the resulting printed structures. Further investigation of thermal conductivity, electrical conductivity, mechanical performance, and heat resistance of printed SiC-based layers would provide a more comprehensive understanding of their practical capabilities. Additionally, optimisation of particle surface chemistry and dispersion strategies may further enhance colloidal stability and printability. For composite systems, future studies could explore alternative hybrid filler combinations, surface functionalisation approaches, and three-dimensional filler architectures to further improve thermal transport performance. The integration of advanced multiscale modelling techniques capable of capturing particle interactions, interfacial resistance, and agglomeration effects would also contribute to more accurate prediction and optimisation of composite properties.

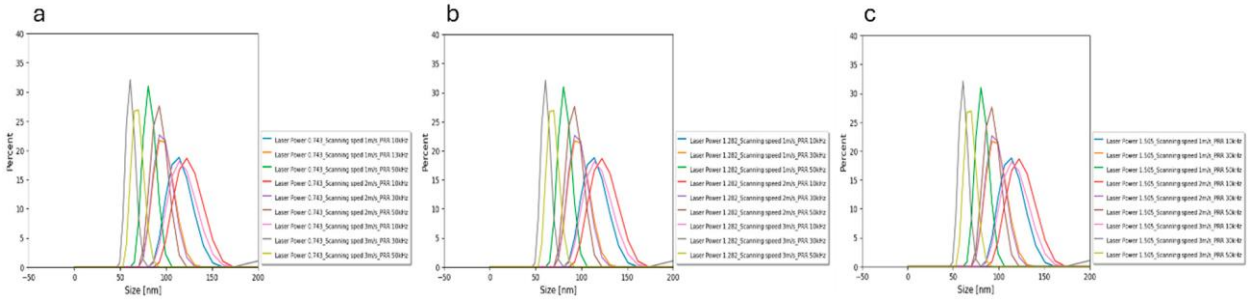
In conclusion, this PhD research successfully demonstrates a complete materials development pathway encompassing the synthesis, characterisation, optimisation, modelling, and application of silicon carbide-based materials. The findings advance both the scientific understanding and practical implementation of SiC nanoparticles and thermally conductive composites, providing a strong foundation for future developments in additive manufacturing, thermal management technologies, abrasive engineering, and advanced functional materials.

7 Appendices

A)

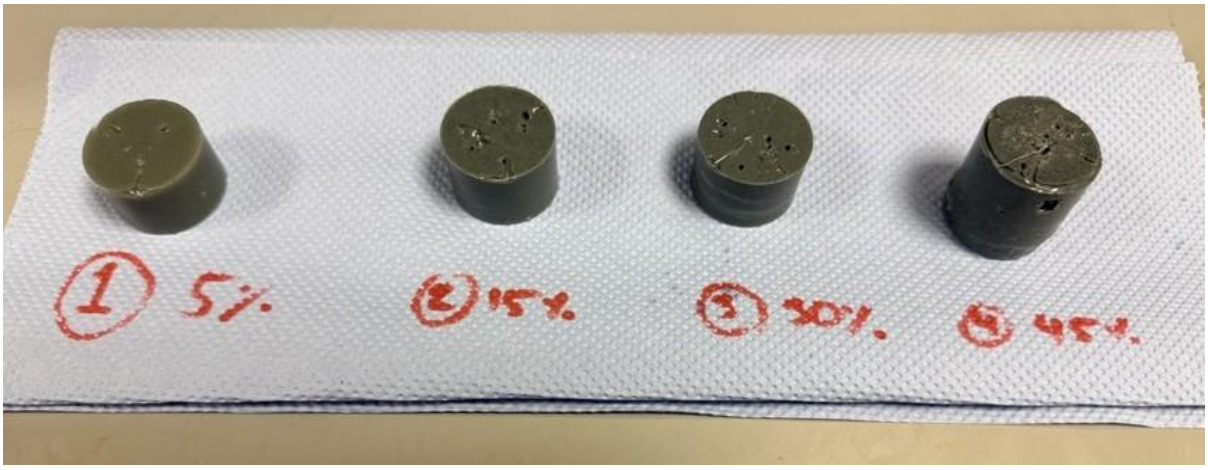


Appendix A1.UV-Vis measurement for the all provided samples categorised based on a constant laser power of a)0.743, b)1.82, and c)1.504 W

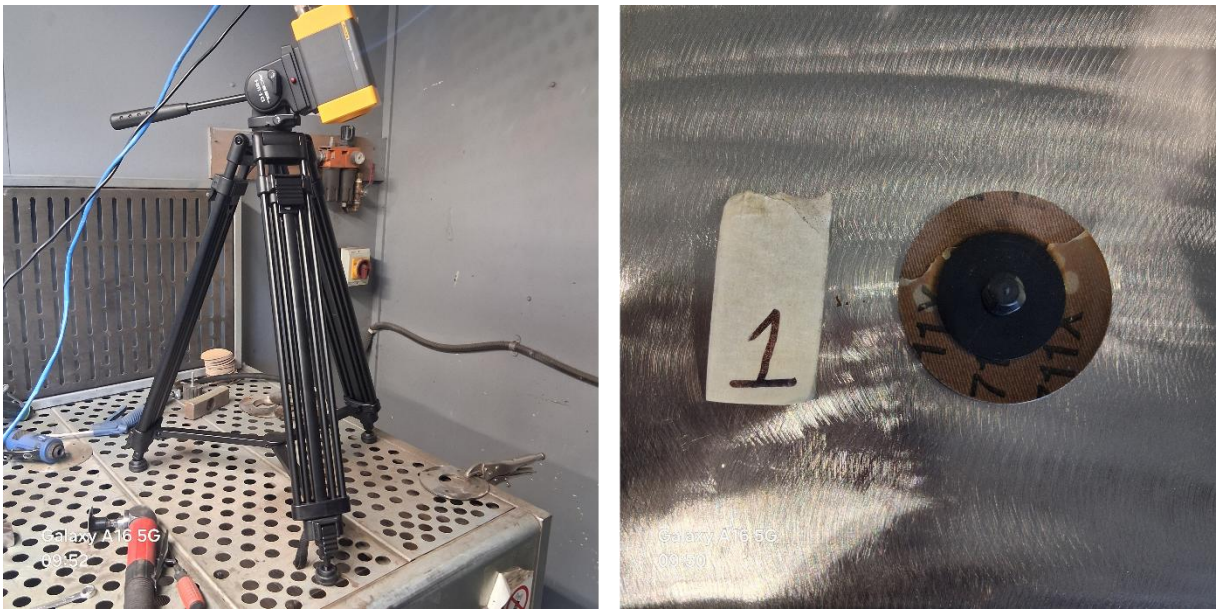


Apemdix A2. DLS measurement of all the produced samples categorised based on a constant laser power of a)0.743, b)1.282, and c)1.504 W

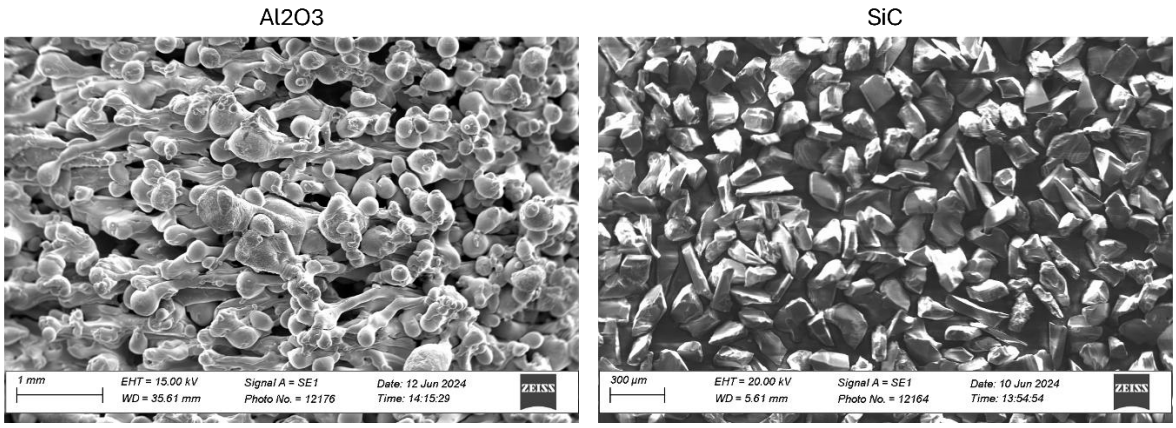
B)



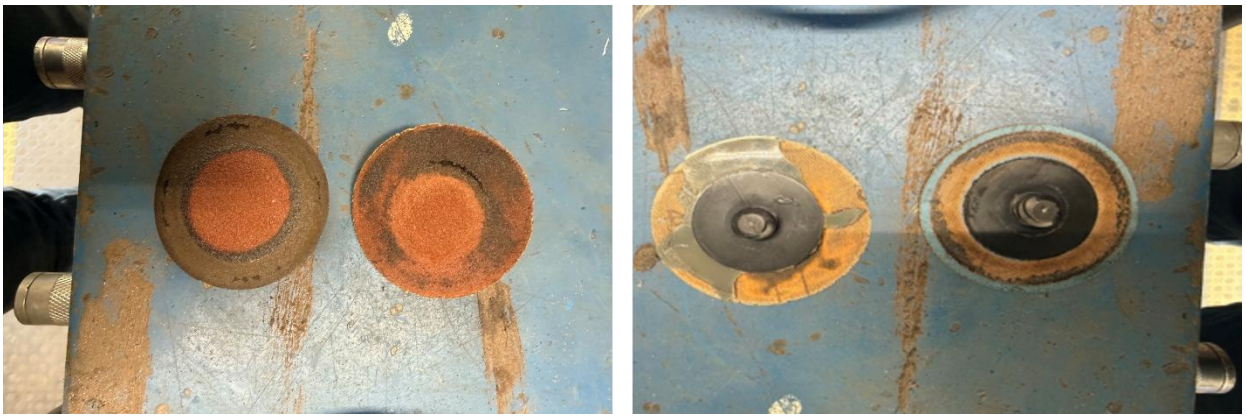
Appendix B1. Prepared samples for Thermal conductivity measurement



Appendix B2. IR camera setup for the measurement and a sample used for the temperature recording data

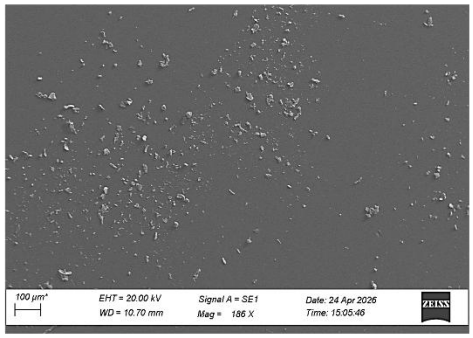


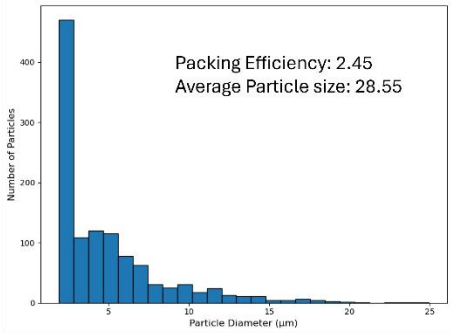
Appendix B3. SEM images of the raw powders used for the composite sample preparation



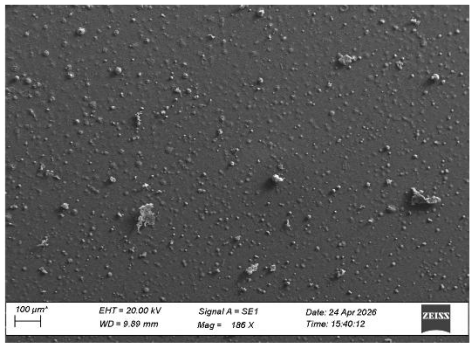
Appendix B4. The samples after the grinding test, left side samples with and right side samples without particle-filled coating

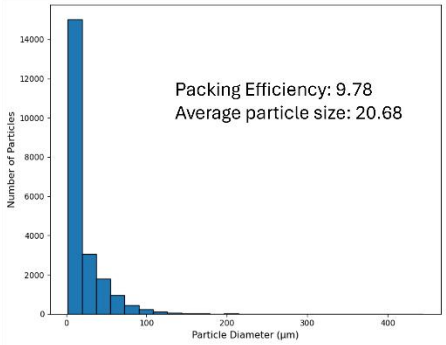
a


100 µm
EHT = 20.00 kV
WD = 10.70 mm
Signal A = SE1
Mag = 186 X
Date: 24 Apr 2026
Time: 15:05:46
ZEISS

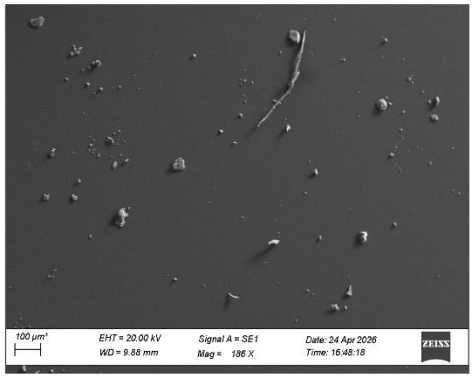

Packing Efficiency: 2.45
Average Particle size: 28.55
Number of Particles
Particle Diameter (µm)

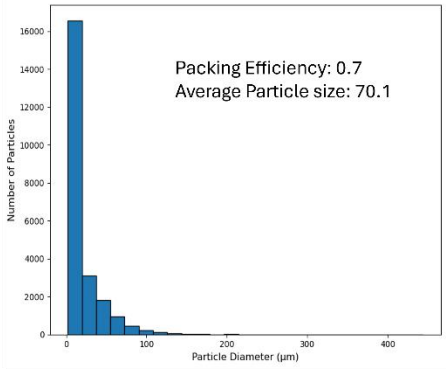
b


100 µm
EHT = 20.00 kV
WD = 9.89 mm
Signal A = SE1
Mag = 186 X
Date: 24 Apr 2026
Time: 15:40:12
ZEISS

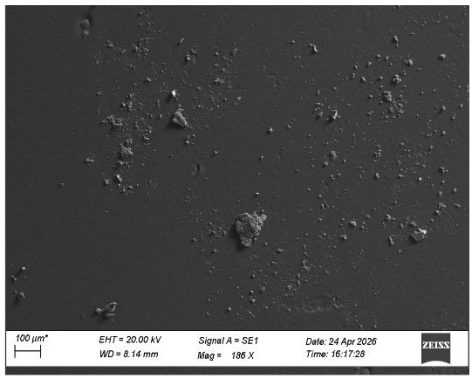

Packing Efficiency: 9.78
Average particle size: 20.68
Number of Particles
Particle Diameter (µm)

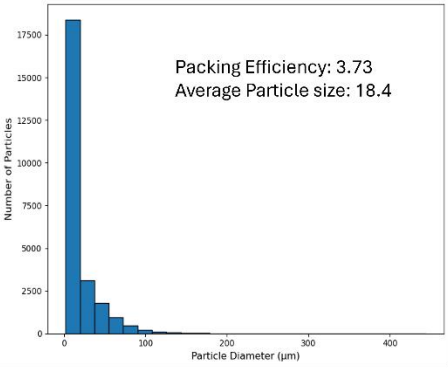
c


100 µm
EHT = 20.00 kV
WD = 9.88 mm
Signal A = SE1
Mag = 186 X
Date: 24 Apr 2026
Time: 16:48:18
ZEISS

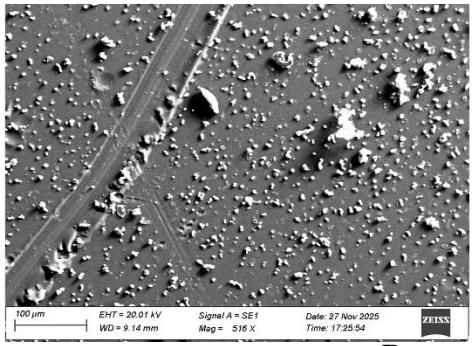

Packing Efficiency: 0.7
Average Particle size: 70.1
Number of Particles
Particle Diameter (µm)

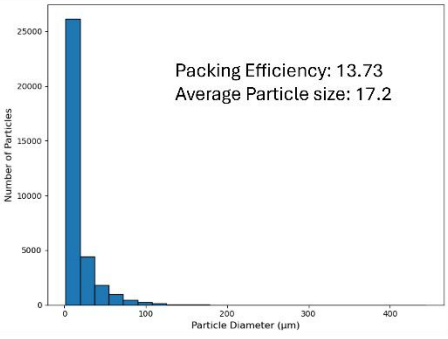
d


100 µm
EHT = 20.00 kV
WD = 8.14 mm
Signal A = SE1
Mag = 186 X
Date: 24 Apr 2026
Time: 16:17:28
ZEISS

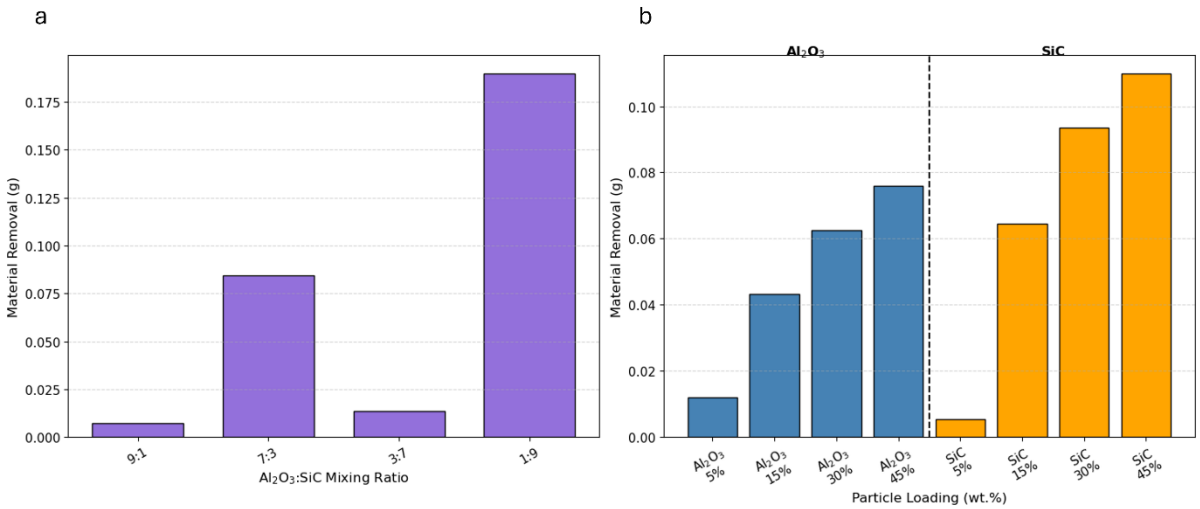

Packing Efficiency: 3.73
Average Particle size: 18.4
Number of Particles
Particle Diameter (µm)

e


100 µm
EHT = 20.01 kV
WD = 9.14 mm
Signal A = SE1
Mag = 516 X
Date: 27 Nov 2025
Time: 17:25:54
ZEISS


Packing Efficiency: 13.73
Average Particle size: 17.2
Number of Particles
Particle Diameter (µm)

Appendix B5. particle size distribution and surface coverage area (packing efficiency) of samples a)SiC 5% loading, b)SiC 45% loading, c)Al2O3 5% loading, d)Al2O3 45% loading, and e) Mixing ratio SiC:Al2O3 9:1



Appendix B6. Material removal of the samples during the grinding process for a) different particle mixing ratios, and b) various particle loadings.



Appendix B7. Grinding process of the sample in the sponsoring company

8 References

[1] M. Dell'Aglio, R. Gaudiuso, O. De Pascale, and A. De Giacomo, "Mechanisms and processes of pulsed laser ablation in liquids during nanoparticle production," Appl. Surf. Sci., vol. 348, pp. 4–9, Sep. 2015, doi: 10.1016/j.apsusc.2015.01.082.

[2] G. K. Yogesh, S. Shukla, D. Sastikumar, and P. Koinkar, "Progress in pulsed laser ablation in liquid (PLAL) technique for the synthesis of carbon nanomaterials: a review," Appl. Phys. A, vol. 127, no. 11, p. 810, Nov. 2021, doi: 10.1007/s00339-021-04951-6.

[3] A. Nyabadza, M. Vázquez, and D. Brabazon, "Magnesium nanoparticle synthesis from powders via LASIS – Effects of liquid medium, laser pulse width and ageing on nanoparticle size, concentration, stability and electrical properties," Colloids Surf. Physicochem. Eng. Asp., vol. 651, p. 129651, Oct. 2022, doi: 10.1016/j.colsurfa.2022.129651.

[4] H. Pereira, C. G. Moura, G. Miranda, and F. S. Silva, "Influence of liquid media and laser energy on the production of MgO nanoparticles by laser ablation," Opt. Laser Technol., vol. 142, p. 107181, Oct. 2021, doi: 10.1016/j.optlastec.2021.107181.

[5] A. Nyabadza, M. Vázquez, B. Fitzpatrick, and D. Brabazon, "Effect of liquid medium and laser processing parameters on the fabrication of carbon nanoparticles via pulsed laser ablation in liquid towards paper electronics," Colloids Surf. Physicochem. Eng. Asp., vol. 636, p. 128151, Mar. 2022, doi: 10.1016/j.colsurfa.2021.128151.

[6] A. E. Urusov et al., "Application of gold nanoparticles produced by laser ablation for immunochromatographic assay labeling," Anal. Biochem., vol. 491, pp. 65–71, Dec. 2015, doi: 10.1016/j.ab.2015.08.031.

[7] É. McCarthy et al., "Silver nanocolloid generation using dynamic Laser Ablation Synthesis in Solution system and drop-casting," Nano-Struct. Nano-Objects, vol. 29, p. 100841, Feb. 2022, doi: 10.1016/j.nanoso.2022.100841.

[8] A. V. Shabalina, T. I. Izaak, T. S. Kharlamova, D. O. Martynova, I. N. Lapin, and V. A. Svetlichnyi, “Ag/SiOx nanocomposite powders synthesized from colloids obtained by pulsed laser ablation,” Colloids Surf. Physicochem. Eng. Asp., vol. 553, pp. 80–88, Sep. 2018, doi: 10.1016/j.colsurfa.2018.05.047.

[9] N. Tarasenka et al., “Fabrication of luminescent silicon carbide nanoparticles by pulsed laser synthesis in liquid,” Appl. Phys. A, vol. 128, no. 9, p. 749, Sep. 2022, doi: 10.1007/s00339-022-05894-2.

[10] C. H. Liang, Y. Shimizu, T. Sasaki, and N. Koshizaki, “Preparation of ultrafine TiO2 nanocrystals via pulsed-laser ablation of titanium metal in surfactant solution,” Appl. Phys. A, vol. 80, no. 4, pp. 819–822, Feb. 2005, doi: 10.1007/s00339-003-2489-6.

[11] B. J. Alwan, L. G. Subhi, and A. N. Abd, “Preparation of colloidal silver oxide nanoparticles by pulsed laser ablation in methanol,” IOP Conf. Ser. Mater. Sci. Eng., vol. 454, p. 012101, Dec. 2018, doi: 10.1088/1757-899X/454/1/012101.

[12] K. S. Khashan, R. A. Ismail, and R. O. Mahdi, “Synthesis of SiC nanoparticles by SHG 532 nm Nd:YAG laser ablation of silicon in ethanol,” Appl. Phys. A, vol. 124, no. 6, p. 443, Jun. 2018, doi: 10.1007/s00339-018-1835-7.

[13] K. S. Khashan, A. Hadi, M. Mahdi, and M. K. Hamid, “Nanosecond pulse laser preparation of InZnO (IZO) nanoparticles NPs for high-performance photodetector,” Appl. Phys. A, vol. 125, no. 1, p. 51, Jan. 2019, doi: 10.1007/s00339-018-2356-0.

[14] V. Presser and K. G. Nickel, “Silica on Silicon Carbide,” Crit. Rev. Solid State Mater. Sci., vol. 33, no. 1, pp. 1–99, Feb. 2008, doi: 10.1080/10408430701718914.

[15] C. T. Yang, S. L. Song, B. H. Yan, and F. Y. Huang, “Improving machining performance of wire electrochemical discharge machining by adding SiC abrasive to electrolyte,” Int. J. Mach. Tools Manuf., vol. 46, no. 15, pp. 2044–2050, Dec. 2006, doi: 10.1016/j.ijmachtools.2006.01.006.

[16] S. Castelletto et al., “Fluorescent color centers in laser ablated 4H-SiC nanoparticles,” Opt. Lett., vol. 42, no. 7, pp. 1297–1300, 2017.

[17] T. Yamada, F. Araki, J. Ishihara, and K. Miyajima, “Fabrication of silicon carbide nanoparticles

using picosecond pulsed laser ablation in acetone with characterizations from TEM and XRD," AIP Adv., vol. 9, no. 10, 2019.

[18] S. Yang, W. Cai, H. Zhang, H. Zeng, and Y. Lei, "A General Strategy for Fabricating Unique Carbide Nanostructures with Excitation Wavelength-Dependent Light Emissions," J. Phys. Chem. C, vol. 115, no. 15, pp. 7279–7284, Apr. 2011, doi: 10.1021/jp111873k.

[19] R. A. Ismail, K. S. Khashan, and R. O. Mahdi, "Characterization of high photosensitivity nanostructured 4H-SiC/p-Si heterostructure prepared by laser ablation of silicon in ethanol," Mater. Sci. Semicond. Process., vol. 68, pp. 252–261, Sep. 2017, doi: 10.1016/j.mssp.2017.06.035.

[20] D. Wu and C. Huang, "Thermal conductivity study of SiC nanoparticle beds for thermal insulation applications," Phys. E Low-Dimens. Syst. Nanostructures, vol. 118, p. 113970, Apr. 2020, doi: 10.1016/j.physe.2020.113970.

[21] A. Sánchez Egea, V. Martynenko, D. Martínez Krahmer, L. López De Lacalle, A. Benítez, and G. Genovese, "On the Cutting Performance of Segmented Diamond Blades when Dry-Cutting Concrete," Materials, vol. 11, no. 2, p. 264, Feb. 2018, doi: 10.3390/ma11020264.

[22] J. Rieu and P. Gœuriot, "Ceramic composites for biomedical applications," Clin. Mater., vol. 12, no. 4, pp. 211–217, Jan. 1993, doi: 10.1016/0267-6605(93)90075-I.

[23] M. K. Egbo, "A fundamental review on composite materials and some of their applications in biomedical engineering," J. King Saud Univ. - Eng. Sci., vol. 33, no. 8, pp. 557–568, Dec. 2021, doi: 10.1016/j.jksues.2020.07.007.

[24] A. Katz-Demyanetz, V. V. Popov, A. Kovalevsky, D. Safranchik, and A. Koptyug, "Powder-bed additive manufacturing for aerospace application: Techniques, metallic and metal/ceramic composite materials and trends," Manuf. Rev., vol. 6, p. 5, 2019, doi: 10.1051/mfreview/2019003.

[25] Bhasha, S. Gautam, P. Malik, and P. Jain, "Ceramic Composites for Aerospace Applications," Diffus. Found., vol. 23, pp. 31–39, Aug. 2019, doi: 10.4028/www.scientific.net/DF.23.31.

[26] B. Stojanovic and J. Glisovic, "Application of Ceramic Matrix Composite in Automotive Industry," in Encyclopedia of Materials: Composites, Elsevier, 2021, pp. 275–292. doi: 10.1016/B978-0-

12-819724-0.00018-5.

[27] R. Gadow and M. Speicher, “Manufacturing of Ceramic Matrix Composites for Automotive Applications,” in Ceramic Transactions Series, 1st ed., vol. 128, N. P. Bansal, J. P. Singh, and H. -T. Lin, Eds., Wiley, 2006, pp. 25–41. doi: 10.1002/9781118380925.ch3.

[28] S. Tang and C. Hu, “Design, Preparation and Properties of Carbon Fiber Reinforced Ultra-High Temperature Ceramic Composites for Aerospace Applications: A Review,” J. Mater. Sci. Technol., vol. 33, no. 2, pp. 117–130, Feb. 2017, doi: 10.1016/j.jmst.2016.08.004.

[29] E. P. Shuaib, G. K. Yogesh, and D. Sastikumar, “Amorphous and photoluminescent crystalline silicon carbide nanoparticles synthesized by laser ablation in liquids,” Mater. Today Proc., vol. 50, pp. 2745–2750, 2022, doi: 10.1016/j.matpr.2020.08.453.

[30] P. Mélinon et al., “Nanostructured silicon films obtained by neutral cluster depositions,” J. Chem. Phys., vol. 107, no. 23, pp. 10278–10287, Dec. 1997, doi: 10.1063/1.474168.

[31] J. B. Varley, B. Shen, and M. Higashiwaki, “Wide bandgap semiconductor materials and devices,” J. Appl. Phys., vol. 131, no. 23, p. 230401, Jun. 2022, doi: 10.1063/5.0100601.

[32] T. Kimoto and J. A. Cooper, Fundamentals of silicon carbide technology: growth, characterization, devices and applications. Singapore: Wiley, 2014. doi: 10.1002/9781118313534.

[33] A. R. Verma, P. Krishna, and H. M. Otte, “Polymorphism and Polytypism in Crystals,” Phys. Today, vol. 20, no. 3, pp. 111–115, Mar. 1967, doi: 10.1063/1.3034193.

[34] A. L. Ortiz, F. Sánchez-Bajo, F. L. Cumbrera, and F. Guiberteau, “The prolific polytypism of silicon carbide,” J. Appl. Crystallogr., vol. 46, no. 1, pp. 242–247, Feb. 2013, doi: 10.1107/S0021889812049151.

[35] G. R. Fisher and P. Barnes, “Towards a unified view of polytypism in silicon carbide,” Philos. Mag. B, vol. 61, no. 2, pp. 217–236, Feb. 1990, doi: 10.1080/13642819008205522.

[36] A. Arefpour, A. Shafieirad, E. Karamian, F. Shahmohammadian, and A. Chami, “Characterization of Nano-SiC Powder Prepared by High-Energy Ball Milling as a Mechanochemical Process with Subsequent Annealing Process,” Glass Phys. Chem., vol. 45, no. 5, pp. 384–387, Sep. 2019,

doi: 10.1134/S108765961905002X.

[37] M. Sherif El-Eskandarany, K. Sumiyama, and K. Suzuki, “Mechanical solid state reaction for synthesis of β–SiC powders,” J. Mater. Res., vol. 10, no. 3, pp. 659–667, Mar. 1995, doi: 10.1557/JMR.1995.0659.

[38] Z.-G. Yang and L. L. Shaw, “Synthesis of nanocrystalline SiC at ambient temperature through high energy reaction milling,” Nanostructured Mater., vol. 7, no. 8, pp. 873–886, Nov. 1996, doi: 10.1016/S0965-9773(96)00058-X.

[39] D. Beke et al., “Characterization of luminescent silicon carbide nanocrystals prepared by reactive bonding and subsequent wet chemical etching,” Appl. Phys. Lett., vol. 99, no. 21, p. 213108, Nov. 2011, doi: 10.1063/1.3663220.

[40] G. Károlyházy et al., “Novel Method for Electroless Etching of 6H–SiC,” Nanomaterials, vol. 10, no. 3, p. 538, Mar. 2020, doi: 10.3390/nano10030538.

[41] D. Beke et al., “Room-Temperature Defect Qubits in Ultrasmall Nanocrystals,” J. Phys. Chem. Lett., vol. 11, no. 5, pp. 1675–1681, Mar. 2020, doi: 10.1021/acs.jpclett.0c00052.

[42] Y. M. Wang, X. R. Hou, W. Xu, and M. Tian, “Effects of reaction temperature on the synthesis of high purity silicon carbide powder,” Mater. Res. Innov., vol. 19, no. sup5, pp. S5-1338-S5-1343, May 2015, doi: 10.1179/1432891714Z.0000000001306.

[43] R. Ma, J. Shi, W. Lin, and J. Chen, “Synthesis and sintering of nanocrystalline SiC ceramic powders,” Mater. Chem. Phys., vol. 253, p. 123445, Oct. 2020, doi: 10.1016/j.matchemphys.2020.123445.

[44] B. Matovic, A. Saponjic, A. Devecerski, and M. Miljkovic, “Fabrication of SiC by carbothermal-reduction reactions of diatomaceous earth,” J. Mater. Sci., vol. 42, no. 14, pp. 5448–5451, Jul. 2007, doi: 10.1007/s10853-006-0780-6.

[45] G. C. Wei, “Beta Sic Powders Produced by Carbothermic Reduction of Silica in a High-Temperature Rotary Furnace,” J. Am. Ceram. Soc., vol. 66, no. 7, Jul. 1983, doi: 10.1111/j.1151-2916.1983.tb10602.x.

[46] S. Ohsaki, D. H. Cho, H. Sano, Y. Uchiyama, and K. Kobayashi, “Synthesis of β-SiC by the Reaction of Gaseous SiO with Activated Carbon,” Key Eng. Mater., vol. 159–160, pp. 89–94, May 1998, doi: 10.4028/www.scientific.net/KEM.159-160.89.

[47] A. Najafi, F. Golestani-Fard, H. R. Rezaie, and N. Ehsani, “A study on sol–gel synthesis and characterization of SiC nano powder,” J. Sol-Gel Sci. Technol., vol. 59, no. 2, pp. 205–214, Aug. 2011, doi: 10.1007/s10971-011-2482-z.

[48] A. Najafi, F. Golestani-Fard, and H. R. Rezaie, “Improvement of SiC nanopowder synthesis by sol–gel method via TEOS/resin phenolic precursors,” J. Sol-Gel Sci. Technol., vol. 75, no. 2, pp. 255–263, Aug. 2015, doi: 10.1007/s10971-015-3695-3.

[49] J. Xu, Y.-M. Liu, B. Xue, Y.-X. Li, Y. Cao, and K.-N. Fan, “A hybrid sol–gel synthesis of mesostructured SiC with tunable porosity and its application as a support for propane oxidative dehydrogenation,” Phys. Chem. Chem. Phys., vol. 13, no. 21, p. 10111, 2011, doi: 10.1039/c0cp02895a.

[50] S. Castelletto et al., “Fluorescent color centers in laser ablated 4H-SiC nanoparticles,” Opt. Lett., vol. 42, no. 7, p. 1297, Apr. 2017, doi: 10.1364/OL.42.001297.

[51] S. Yang, W. Cai, H. Zeng, and X. Xu, “Ultra-fine β-SiC quantum dots fabricated by laser ablation in reactive liquid at room temperature and their violet emission,” J. Mater. Chem., vol. 19, no. 38, p. 7119, 2009, doi: 10.1039/b909800c.

[52] X. Yu et al., “Carbonization of Silicon Nanoparticles via Ablation Induced by Femtosecond Laser Pulses in Hexane,” Arab. J. Sci. Eng., vol. 42, no. 10, pp. 4221–4226, Oct. 2017, doi: 10.1007/s13369-017-2619-7.

[53] A. Gupta, T. Ghosh, and C. Jacob, “The influence of diluent gas composition and temperature on SiC nanopowder formation by CVD,” J. Mater. Sci., vol. 42, no. 13, pp. 5142–5146, Jul. 2007, doi: 10.1007/s10853-006-1267-1.

[54] Q.-G. Fu, H.-J. Li, X.-H. Shi, K.-Z. Li, J. Wei, and Z.-B. Hu, “Synthesis of silicon carbide nanowires by CVD without using a metallic catalyst,” Mater. Chem. Phys., vol. 100, no. 1, pp. 108–111, Nov. 2006, doi: 10.1016/j.matchemphys.2005.12.014.

[55] Y. Kamlag, A. Goossens, I. Colbeck, and J. Schoonman, “Formation of Nano SiC Particles by Laser-Assisted CVD,” Chem. Vap. Depos., vol. 9, no. 3, pp. 125–129, Jun. 2003, doi: 10.1002/cvde.200306239.

[56] T. D. Shen, C. C. Koch, T. L. McCormick, R. J. Nemanich, J. Y. Huang, and J. G. Huang, “The structure and property characteristics of amorphous/nanocrystalline silicon produced by ball milling,” J. Mater. Res., vol. 10, no. 1, pp. 139–148, Jan. 1995, doi: 10.1557/JMR.1995.0139.

[57] J. Zhu, Z. Liu, X. L. Wu, L. L. Xu, W. C. Zhang, and P. K. Chu, “Luminescent small-diameter 3C-SiC nanocrystals fabricated via a simple chemical etching method,” Nanotechnology, vol. 18, no. 36, p. 365603, Sep. 2007, doi: 10.1088/0957-4484/18/36/365603.

[58] X. L. Wu, J. Y. Fan, T. Qiu, X. Yang, G. G. Siu, and P. K. Chu, “Experimental Evidence for the Quantum Confinement Effect in 3 C -SiC Nanocrystallites,” Phys. Rev. Lett., vol. 94, no. 2, p. 026102, Jan. 2005, doi: 10.1103/PhysRevLett.94.026102.

[59] A. M. Rossi, T. E. Murphy, and V. Reipa, “Ultraviolet photoluminescence from 6H silicon carbide nanoparticles,” Appl. Phys. Lett., vol. 92, no. 25, p. 253112, Jun. 2008, doi: 10.1063/1.2950084.

[60] J. Fan, H. Li, J. Wang, and M. Xiao, “Fabrication and photoluminescence of SiC quantum dots stemming from 3C, 6H, and 4H polytypes of bulk SiC,” Appl. Phys. Lett., vol. 101, no. 13, p. 131906, Sep. 2012, doi: 10.1063/1.4755778.

[61] S. Larpkiattaworn, P. Ngernchuklin, W. Khongwong, N. Pankurddee, and S. Wada, “The influence of reaction parameters on the free Si and C contents in the synthesis of nano-sized SiC,” Ceram. Int., vol. 32, no. 8, pp. 899–904, Dec. 2006, doi: 10.1016/j.ceramint.2005.06.011.

[62] Y. Zhong, L. L. Shaw, M. Manjarres, and M. F. Zawrah, “Synthesis of Silicon Carbide Nanopowder Using Silica Fume,” J. Am. Ceram. Soc., vol. 93, no. 10, pp. 3159–3167, Oct. 2010, doi: 10.1111/j.1551-2916.2010.03867.x.

[63] J. Li, J. Tian, and L. Dong, “Synthesis of SiC precursors by a two-step sol–gel process and their conversion to SiC powders,” J. Eur. Ceram. Soc., vol. 20, no. 11, pp. 1853–1857, Oct. 2000, doi: 10.1016/S0955-2219(00)00055-8.

[64] E. P. Shuaib, G. K. Yogesh, and D. Sastikumar, “Amorphous and photoluminescent crystalline silicon carbide nanoparticles synthesized by laser ablation in liquids,” Mater. Today Proc., vol. 50, pp. 2745–2750, 2022, doi: 10.1016/j.matpr.2020.08.453.

[65] Z. R. Huang, B. Liang, D. L. Jiang, and S. H. Tan, “Preparation of nanocrystal SiC powder by chemical vapour deposition,” J. Mater. Sci., vol. 31, no. 16, pp. 4327–4332, Aug. 1996, doi: 10.1007/BF00356457.

[66] M. Iijima and H. Kamiya, “Surface Modification of Silicon Carbide Nanoparticles by Azo Radical Initiators,” J. Phys. Chem. C, vol. 112, no. 31, pp. 11786–11790, Aug. 2008, doi: 10.1021/jp709608p.

[67] L. Saravanan, S. Subramanian, A. B. V. Kumar, and R. N. Tharanathan, “Surface chemical studies on SiC suspension in the presence of chitosan,” Ceram. Int., vol. 32, no. 6, pp. 637–646, Jan. 2006, doi: 10.1016/j.ceramint.2005.04.023.

[68] E. M. Huseynov and T. G. Naghiyev, “Study of thermal parameters of nanocrystalline silicon carbide (3C-SiC) using DSC spectroscopy,” Appl. Phys. A, vol. 127, no. 4, p. 267, Apr. 2021, doi: 10.1007/s00339-021-04410-2.

[69] E. Huseynov and A. Garibov, “Effects of Neutron Flux on the Temperature Dependency of Permittivity of 3C-SiC Nanoparticles,” Silicon, vol. 9, no. 5, pp. 753–759, Sep. 2017, doi: 10.1007/s12633-016-9486-9.

[70] H. Xie, J. Wang, T. Xi, Y. Liu, and F. Ai, “Thermal conductivity of suspension containing SiC particles,” J. Mater. Sci. Lett., vol. 21, no. 3, pp. 193–195, Feb. 2002, doi: 10.1023/A:1014742722343.

[71] E. V. Timofeeva, D. S. Smith, W. Yu, D. M. France, D. Singh, and J. L. Routbort, “Particle size and interfacial effects on thermo-physical and heat transfer characteristics of water-based α-SiC nanofluids,” Nanotechnology, vol. 21, no. 21, p. 215703, May 2010, doi: 10.1088/0957-4484/21/21/215703.

[72] A. See et al., “Dielectric behavior of β-SiC nanopowders in air between 30 and 400 °C,” J. Mater. Sci. Mater. Electron., vol. 27, no. 7, pp. 6623–6629, Jul. 2016, doi: 10.1007/s10854-016-4608-0.

[73] E. Huseynov, “Neutron irradiation and frequency effects on the electrical conductivity of nanocrystalline silicon carbide (3C-SiC),” Phys. Lett. A, vol. 380, no. 38, pp. 3086–3091, Sep. 2016, doi: 10.1016/j.physleta.2016.07.009.

[74] F. Chen et al., “Cellular toxicity of silicon carbide nanomaterials as a function of morphology,” Biomaterials, vol. 179, pp. 60–70, Oct. 2018, doi: 10.1016/j.biomaterials.2018.06.027.

[75] O. Lozano et al., “Effects of SiC nanoparticles orally administered in a rat model: Biodistribution, toxicity and elemental composition changes in feces and organs,” Toxicol. Appl. Pharmacol., vol. 264, no. 2, pp. 232–245, Oct. 2012, doi: 10.1016/j.taap.2012.08.004.

[76] J. Pourchez et al., “In vitro cellular responses to silicon carbide nanoparticles: impact of physico-chemical features on pro-inflammatory and pro-oxidative effects,” J. Nanoparticle Res., vol. 14, no. 10, p. 1143, Oct. 2012, doi: 10.1007/s11051-012-1143-7.

[77] B. Mognetti et al., “Preferential Killing of Cancer Cells Using Silicon Carbide Quantum Dots,” J. Nanosci. Nanotechnol., vol. 10, no. 12, pp. 7971–7975, Dec. 2010, doi: 10.1166/jnn.2010.3049.

[78] Q. Liu, W. Han, and P. Hu, “Microstructure and mechanical properties of ZrB2–SiC nanocomposite ceramic,” Scr. Mater., vol. 61, no. 7, pp. 690–692, Oct. 2009, doi: 10.1016/j.scriptamat.2009.05.041.

[79] S. N. S. Mohamad, N. Mahmed, D. S. C. Halin, K. A. Razak, M. N. Norizan, and I. S. Mohamad, “Synthesis of alumina nanoparticles by sol-gel method and their applications in the removal of copper ions (Cu^{2+}) from the solution,” IOP Conf. Ser. Mater. Sci. Eng., vol. 701, no. 1, p. 012034, Dec. 2019, doi: 10.1088/1757-899X/701/1/012034.

[80] L. Song, Y. Dong, Q. Shao, and J. Jiang, “Synthesis of monodisperse α-Al_2 O_3 nanoparticles by a salt microemulsion method,” Micro Nano Lett., vol. 13, no. 8, pp. 1071–1074, Aug. 2018, doi: 10.1049/mnl.2018.0078.

[81] P. A. Prashanth et al., “Synthesis, characterizations, antibacterial and photoluminescence studies of solution combustion-derived α-Al_2 O_3 nanoparticles,” J. Asian Ceram. Soc., vol. 3, no. 3, pp. 345–351, Sep. 2015, doi: 10.1016/j.jascer.2015.07.001.

[82] J. Li, M. J. Hurlock, V. G. Goncharov, X. Li, X. Guo, and Q. Zhang, “Solvent-Free and Phase-Selective Synthesis of Aluminum Trimesate Metal–Organic Frameworks,” Inorg. Chem., vol. 60, no. 7, pp. 4623–4632, Apr. 2021, doi: 10.1021/acs.inorgchem.0c03598.

[83] A. Z. Ziva, Y. K. Suryana, Y. S. Kurniadianti, A. B. D. Nandiyanto, and T. Kurniawan, “Recent Progress on the Production of Aluminum Oxide (Al2O3) Nanoparticles: A Review,” Mech. Eng. Soc. Ind., vol. 1, no. 2, pp. 54–77, Sep. 2021, doi: 10.31603/mesi.5493.

[84] M. T. Hernández and M. González, “Synthesis of Resins by Microwave and Infrared Heating as Precursors of Alpha-Alumina. Comparison of the Results,” Key Eng. Mater., vol. 206–213, pp. 71–74, Dec. 2001, doi: 10.4028/www.scientific.net/KEM.206-213.71.

[85] A. Kaboorani and B. Riedl, “Nano-aluminum oxide as a reinforcing material for thermoplastic adhesives,” J. Ind. Eng. Chem., vol. 18, no. 3, pp. 1076–1081, May 2012, doi: 10.1016/j.jiec.2011.12.001.

[86] D. E. Tallman, K. L. Levine, C. Siripirom, V. G. Gelling, G. P. Bierwagen, and S. G. Croll, “Nanocomposite of polypyrrole and alumina nanoparticles as a coating filler for the corrosion protection of aluminium alloy 2024-T3,” Appl. Surf. Sci., vol. 254, no. 17, pp. 5452–5459, Jun. 2008, doi: 10.1016/j.apsusc.2008.02.099.

[87] W. G. Sawyer, K. D. Freudenberg, P. Bhimaraj, and L. S. Schadler, “A study on the friction and wear behavior of PTFE filled with alumina nanoparticles,” Wear, vol. 254, no. 5–6, pp. 573–580, Mar. 2003, doi: 10.1016/S0043-1648(03)00252-7.

[88] A. Omrani and A. A. Rostami, “Understanding the effect of nano-Al2O3 addition upon the properties of epoxy-based hybrid composites,” Mater. Sci. Eng. A, vol. 517, no. 1–2, pp. 185–190, Aug. 2009, doi: 10.1016/j.msea.2009.03.076.

[89] L. Zhai, G. Ling, J. Li, and Y. Wang, “The effect of nanoparticles on the adhesion of epoxy adhesive,” Mater. Lett., vol. 60, no. 25–26, pp. 3031–3033, Nov. 2006, doi: 10.1016/j.matlet.2006.02.038.

[90] S. Zhao, L. Schadler, R. Duncan, H. Hillborg, and T. Auletta, “Mechanisms leading to improved mechanical performance in nanoscale alumina filled epoxy,” Compos. Sci. Technol., vol. 68, no. 14, pp.

2965–2975, Nov. 2008, doi: 10.1016/j.compscitech.2008.01.009.

[91] B. Arnold, “The Inside of the Aluminium Oxide,” in Rubies and Implants, Berlin, Heidelberg: Springer Berlin Heidelberg, 2022, pp. 9–11. doi: 10.1007/978-3-662-66116-1_4.

[92] L. Li, S. Pu, Y. Liu, L. Zhao, J. Ma, and J. Li, “High-purity disperse α-Al2O3 nanoparticles synthesized by high-energy ball milling,” Adv. Powder Technol., vol. 29, no. 9, pp. 2194–2203, Sep. 2018, doi: 10.1016/j.apt.2018.06.003.

[93] H. J. Shin, S. O. Lee, S. J. Kim, T. Tran, and M. J. Kim, “Study on the effect of humate and its removal on the precipitation of aluminium trihydroxide from the Bayer process,” Miner. Eng., vol. 17, no. 3, pp. 387–391, Mar. 2004, doi: 10.1016/j.mineng.2003.11.003.

[94] F. W. Aldbea et al., “Structural and optical properties of α aluminum oxide prepared by sol-gel method,” Curr. Appl. Phys., vol. 71, pp. 85–90, Mar. 2025, doi: 10.1016/j.cap.2024.12.008.

[95] A. Z. Zhuk and M. S. Vlaskin, “Synthesis of high-purity aluminum oxide from hydrothermally produced boehmite by high temperature vacuum treatment,” Mater. Today Proc., vol. 4, no. 11, pp. 11580–11587, 2017, doi: 10.1016/j.matpr.2017.09.069.

[96] M. H. Jasimin, N. Badar, R. Roshidah, and N. Kamarulzaman, “Synthesis and Characterization of Al_2O_3 by Using a Combustion Synthesis Method,” Adv. Mater. Res., vol. 545, pp. 169–171, Jul. 2012, doi: 10.4028/www.scientific.net/AMR.545.169.

[97] Y. L. Wu, J. Hong, D. Peterson, J. Zhou, T. S. Cho, and D. N. Ruzic, “Deposition of aluminum oxide by evaporative coating at atmospheric pressure (ECAP),” Surf. Coat. Technol., vol. 237, pp. 369–378, Dec. 2013, doi: 10.1016/j.surfcoat.2013.06.043.

[98] M. Kusper and G. Guisbiers, “Synthesis of aluminum oxide nanoparticles by laser ablation in liquids,” MRS Adv., vol. 3, no. 64, pp. 3899–3903, Dec. 2018, doi: 10.1557/adv.2018.626.

[99] S. P. Goutam, G. Saxena, D. Roy, A. K. Yadav, and R. N. Bharagava, “Green Synthesis of Nanoparticles and Their Applications in Water and Wastewater Treatment,” in Bioremediation of Industrial Waste for Environmental Safety: Volume I: Industrial Waste and Its Management, G. Saxena and R. N. Bharagava, Eds., Singapore: Springer Singapore, 2020, pp. 349–379. doi: 10.1007/978-981-13-

1891-7_16.

[100] P. Hassanpour et al., “Biomedical applications of aluminium oxide nanoparticles,” Micro Nano Lett., vol. 13, no. 9, pp. 1227–1231, Sep. 2018, doi: 10.1049/mnl.2018.5070.

[101] S. Li et al., “Development and applications of aluminum alloys for aerospace industry,” J. Mater. Res. Technol., vol. 27, pp. 944–983, Nov. 2023, doi: 10.1016/j.jmrt.2023.09.274.

[102] X. Wu and W. Zhang, “A review on aluminum matrix composites’ characteristics and applications for automotive sector,” Heliyon, vol. 10, no. 20, p. e38576, Oct. 2024, doi: 10.1016/j.heliyon.2024.e38576.

[103] A. Eftekhari, “Aluminum oxide as a multi-function agent for improving battery performance of LiMn2O4 cathode,” Solid State Ion., vol. 167, no. 3–4, pp. 237–242, Feb. 2004, doi: 10.1016/j.ssi.2004.01.016.

[104] H. Hasoon Al-Moameri, Z. Majid Nahi, D. Raheem Rzaij, and N. T. Al-Sharify, “A REVIEW ON THE BIOMEDICAL APPLICATIONS OF ALUMINA,” J. Eng. Sustain. Dev., vol. 24, no. 5, pp. 28–36, Feb. 2022, doi: 10.31272/jeasd.24.5.5.

[105] P. N. Silva-Holguín, Á. D. J. Ruíz-Baltazar, N. A. Medellín-Castillo, G. J. Labrada-Delgado, and S. Y. Reyes-López, “Synthesis and Characterization of α-Al2O3/Ba-β-Al2O3 Spheres for Cadmium Ions Removal from Aqueous Solutions,” Materials, vol. 15, no. 19, p. 6809, Sep. 2022, doi: 10.3390/ma15196809.

[106] E. J. Cho, H. Holback, K. C. Liu, S. A. Abouelmagd, J. Park, and Y. Yeo, “Nanoparticle Characterization: State of the Art, Challenges, and Emerging Technologies,” Mol. Pharm., vol. 10, no. 6, pp. 2093–2110, Jun. 2013, doi: 10.1021/mp300697h.

[107] S. V. Rao, G. K. Podagatlapalli, and S. Hamad, “Ultrafast laser ablation in liquids for nanomaterials and applications,” J. Nanosci. Nanotechnol., vol. 14, no. 2, pp. 1364–1388, 2014.

[108] K. Zhou, X. Zhou, J. Liu, and Z. Huang, “Application of magnetic nanoparticles in petroleum industry: A review,” J. Pet. Sci. Eng., vol. 188, p. 106943, May 2020, doi: 10.1016/j.petrol.2020.106943.

[109] A. Beck et al., “The dynamics of overlayer formation on catalyst nanoparticles and strong metal-

support interaction," Nat. Commun., vol. 11, no. 1, p. 3220, Jun. 2020, doi: 10.1038/s41467-020-17070-2.

[110] R. Aliev, J. Gulomov, M. Abduvohidov, S. Aliev, Z. Ziyoitdinov, and N. Yuldasheva, "Stimulation of Photoactive Absorption of Sunlight in Thin Layers of Silicon Structures by Metal Nanoparticles," Appl. Sol. Energy, vol. 56, no. 5, pp. 364–370, Sep. 2020, doi: 10.3103/S0003701X20050035.

[111] R. Krishnapriya, C. Nizamudeen, B. Saini, M. S. Mozumder, R. K. Sharma, and A.-H. I. Mourad, "MOF-derived Co2+-doped TiO2 nanoparticles as photoanodes for dye-sensitized solar cells," Sci. Rep., vol. 11, no. 1, p. 16265, Aug. 2021, doi: 10.1038/s41598-021-95844-4.

[112] M. M. Rahman, M. R. Karim, H. F. Alharbi, B. Aldokhayel, T. Uzzaman, and H. Zahir, "Cadmium Selenide Quantum Dots for Solar Cell Applications: A Review," Chem. – Asian J., vol. 16, no. 8, pp. 902–921, Apr. 2021, doi: 10.1002/asia.202001369.

[113] X. Hu, Y. Zhang, T. Ding, J. Liu, and H. Zhao, "Multifunctional Gold Nanoparticles: A Novel Nanomaterial for Various Medical Applications and Biological Activities," Front. Bioeng. Biotechnol., vol. 8, 2020, [Online]. Available: https://www.frontiersin.org/articles/10.3389/fbioe.2020.00990

[114] I. Ijaz, E. Gilani, A. Nazir, and A. Bukhari, "Detail review on chemical, physical and green synthesis, classification, characterizations and applications of nanoparticles," Green Chem. Lett. Rev., vol. 13, no. 3, pp. 223–245, Jul. 2020, doi: 10.1080/17518253.2020.1802517.

[115] A. Gour and N. K. Jain, "Advances in green synthesis of nanoparticles," Artif. Cells Nanomedicine Biotechnol., vol. 47, no. 1, pp. 844–851, Dec. 2019, doi: 10.1080/21691401.2019.1577878.

[116] M. Dell'Aglio, R. Gaudiuso, O. De Pascale, and A. De Giacomo, "Mechanisms and processes of pulsed laser ablation in liquids during nanoparticle production," Adv. Synth. Funct. Nanoparticles Lasers Liq. – Fundam. Appl. Catal. Energy Sci. Biomed., vol. 348, pp. 4–9, Sep. 2015, doi: 10.1016/j.apsusc.2015.01.082.

[117] A. Nyabadza, M. Vazquez, and D. Brabazon, "A Review of Bimetallic and Monometallic Nanoparticle Synthesis via Laser Ablation in Liquid," Crystals, vol. 13, no. 2, 2023, doi:

10.3390/cryst13020253.

[118] G. K. Yogesh, S. Shukla, D. Sastikumar, and P. Koinkar, “Progress in pulsed laser ablation in liquid (PLAL) technique for the synthesis of carbon nanomaterials: a review,” Appl. Phys. A, vol. 127, no. 11, p. 810, Nov. 2021, doi: 10.1007/s00339-021-04951-6.

[119] A. Nyabadza et al., “A review of physical, chemical and biological synthesis methods of bimetallic nanoparticles and applications in sensing, water treatment, biomedicine, catalysis and hydrogen storage,” Adv. Colloid Interface Sci., vol. 321, p. 103010, Nov. 2023, doi: 10.1016/j.cis.2023.103010.

[120] A. Nyabadza, M. Vázquez, S. Coyle, B. Fitzpatrick, and D. Brabazon, “Magnesium Nanoparticle Synthesis from Powders via Pulsed Laser Ablation in Liquid for Nanocolloid Production,” Appl. Sci., vol. 11, no. 22, 2021, doi: 10.3390/app112210974.

[121] A. Al-Hamaoy et al., “Liquid Phase – Pulsed Laser Ablation: A route to fabricate different carbon nanostructures,” E-MRS 2013 Symp. V “Laser Mater. Interact. Micro- Nano- Appl. 27–31 May 2013 Strasbg. Fr., vol. 302, pp. 141–144, May 2014, doi: 10.1016/j.apsusc.2013.09.102.

[122] A. Nyabadza, M. Vázquez, B. Fitzpatrick, and D. Brabazon, “Effect of liquid medium and laser processing parameters on the fabrication of carbon nanoparticles via pulsed laser ablation in liquid towards paper electronics,” Colloids Surf. Physicochem. Eng. Asp., vol. 636, p. 128151, Mar. 2022, doi: 10.1016/j.colsurfa.2021.128151.

[123] E. P. Shuaib, G. K. Yogesh, and D. Sastikumar, “Amorphous and photoluminescent crystalline silicon carbide nanoparticles synthesized by laser ablation in liquids,” Natl. Conf. Mater. Sci., vol. 50, pp. 2745–2750, Jan. 2022, doi: 10.1016/j.matpr.2020.08.453.

[124] H. Lin, J. A. Gerbec, M. Sushchikh, and E. W. McFarland, “Synthesis of amorphous silicon carbide nanoparticles in a low temperature low pressure plasma reactor,” Nanotechnology, vol. 19, no. 32, p. 325601, 2008.

[125] S. Askari et al., “Ultra-small photoluminescent silicon-carbide nanocrystals by atmospheric-pressure plasmas,” Nanoscale, vol. 8, no. 39, pp. 17141–17149, 2016.

[126] K. S. Khashan, R. A. Ismail, and R. O. Mahdi, “Synthesis of SiC nanoparticles by SHG 532 nm

Nd:YAG laser ablation of silicon in ethanol," Appl. Phys. A, vol. 124, no. 6, p. 443, May 2018, doi: 10.1007/s00339-018-1835-7.

[127] S. Somiya and Y. Inomata, Silicon Carbide Ceramics: Gas phase reactions, fibers and whisker, joining, vol. 2. Springer Science & Business Media, 1991.

[128] R. Rajarao, R. Ferreira, S. H. F. Sadi, R. Khanna, and V. Sahajwalla, "Synthesis of silicon carbide nanoparticles by using electronic waste as a carbon source," Mater. Lett., vol. 120, pp. 65–68, 2014.

[129] X. Guo, H. Song, Y. Li, P. Wang, and S. Liu, "Fabrication of 4H–SiC nanoparticles using femtosecond pulsed laser ablation in deionized water," Opt. Mater., vol. 132, p. 112817, Oct. 2022, doi: 10.1016/j.optmat.2022.112817.

[130] N. Tarasenka et al., "Fabrication of luminescent silicon carbide nanoparticles by pulsed laser synthesis in liquid," Appl. Phys. A, vol. 128, no. 9, p. 749, 2022.

[131] W. Shi, Y. Zheng, H. Peng, N. Wang, C. S. Lee, and S.-T. Lee, "Laser ablation synthesis and optical characterization of silicon carbide nanowires," J. Am. Ceram. Soc., vol. 83, no. 12, pp. 3228–3230, 2000.

[132] P. Molian, B. Pecholt, and S. Gupta, "Picosecond pulsed laser ablation and micromachining of 4H-SiC wafers," Appl. Surf. Sci., vol. 255, no. 8, pp. 4515–4520, Feb. 2009, doi: 10.1016/j.apsusc.2008.11.071.

[133] K. Bagga, R. McCann, M. Wang, A. Stalcup, M. Vázquez, and D. Brabazon, "Laser assisted synthesis of carbon nanoparticles with controlled viscosities for printing applications," J. Colloid Interface Sci., vol. 447, pp. 263–268, Jun. 2015, doi: 10.1016/j.jcis.2014.10.046.

[134] Abubaker Hassan Hamad, "Effects of Different Laser Pulse Regimes (Nanosecond, Picosecond and Femtosecond) on the Ablation of Materials for Production of Nanoparticles in Liquid Solution," in High Energy and Short Pulse Lasers, Richard Viskup, Ed., Rijeka: IntechOpen, 2016, p. Ch. 12. doi: 10.5772/63892.

[135] L. Liang, J. Yuan, and G. Lin, "Effect of the scanning speed on the microgroove formation regime in nanosecond-pulsed laser scanning ablation of cermet," Int. J. Adv. Manuf. Technol., vol. 107,

no. 1, pp. 97–107, Mar. 2020, doi: 10.1007/s00170-020-05017-2.

[136] F. Claverie, B. Fernández, C. Pécheyran, J. Alexis, and O. F. Donard, “Elemental fractionation effects in high repetition rate IR femtosecond laser ablation ICP-MS analysis of glasses,” J. Anal. At. Spectrom., vol. 24, no. 7, pp. 891–902, 2009.

[137] K. Sugioka, M. Meunier, and A. Piqué, Laser Precision Microfabrication. Springer Berlin Heidelberg, 2010. [Online]. Available: https://books.google.ie/books?id=Ho_QDAEACAAJ

[138] L. Torrisi and A. Torrisi, “Laser ablation parameters influencing gold nanoparticle synthesis in water,” Radiat. Eff. Defects Solids, vol. 173, no. 9–10, pp. 729–739, Oct. 2018, doi: 10.1080/10420150.2018.1528598.

[139] R. Streubel, G. Bendt, and B. Gökce, “Pilot-scale synthesis of metal nanoparticles by high-speed pulsed laser ablation in liquids,” Nanotechnology, vol. 27, no. 20, p. 205602, Apr. 2016, doi: 10.1088/0957-4484/27/20/205602.

[140] A. Wazeer, A. Das, A. Sinha, and A. Karmakar, “Nanomaterials Synthesis via Laser Ablation in Liquid: A Review,” J. Inst. Eng. India Ser. D, vol. 104, no. 1, pp. 413–426, Jun. 2023, doi: 10.1007/s40033-022-00370-w.

[141] N. G. Semaltianos, “Nanoparticles by Laser Ablation,” Crit. Rev. Solid State Mater. Sci., vol. 35, no. 2, pp. 105–124, May 2010, doi: 10.1080/10408431003788233.

[142] N. Abid et al., “Synthesis of nanomaterials using various top-down and bottom-up approaches, influencing factors, advantages, and disadvantages: A review,” Adv. Colloid Interface Sci., vol. 300, p. 102597, Feb. 2022, doi: 10.1016/j.cis.2021.102597.

[143] P. Christian, F. Von der Kammer, M. Baalousha, and Th. Hofmann, “Nanoparticles: structure, properties, preparation and behaviour in environmental media,” Ecotoxicology, vol. 17, no. 5, pp. 326–343, Jul. 2008, doi: 10.1007/s10646-008-0213-1.

[144] A. Menéndez-Manjón, B. N. Chichkov, and S. Barcikowski, “Influence of Water Temperature on the Hydrodynamic Diameter of Gold Nanoparticles from Laser Ablation,” J. Phys. Chem. C, vol. 114, no. 6, pp. 2499–2504, Feb. 2010, doi: 10.1021/jp909897v.

[145] G. Fracasso et al., “Nanoaggregates of iron poly-oxo-clusters obtained by laser ablation in aqueous solution of phosphonates,” J. Colloid Interface Sci., vol. 522, pp. 208–216, Jul. 2018, doi: 10.1016/j.jcis.2018.03.065.

[146] G. K. Yogesh, S. Shukla, D. Sastikumar, and P. Koinkar, “Progress in pulsed laser ablation in liquid (PLAL) technique for the synthesis of carbon nanomaterials: a review,” Appl. Phys. A, vol. 127, no. 11, p. 810, Nov. 2021, doi: 10.1007/s00339-021-04951-6.

[147] M. S. Majeed, S. M. Hassan, and S. A. Fadhil, “AgO Nanoparticles Synthesis by Different Nd:YAG Laser Pulse Energies,” Lasers Manuf. Mater. Process., vol. 9, no. 2, pp. 228–240, Jun. 2022, doi: 10.1007/s40516-022-00174-6.

[148] B. Freeland et al., “Real-time monitoring and control for high-efficiency autonomous laser fabrication of silicon nanoparticle colloids,” Int. J. Adv. Manuf. Technol., vol. 114, no. 1–2, pp. 291–304, May 2021, doi: 10.1007/s00170-021-06772-6.

[149] A. Muzha et al., “Room-temperature near-infrared silicon carbide nanocrystalline emitters based on optically aligned spin defects,” Appl. Phys. Lett., vol. 105, no. 24, p. 243112, Dec. 2014, doi: 10.1063/1.4904807.

[150] F. Fuchs et al., “Silicon carbide light-emitting diode as a prospective room temperature source for single photons,” Sci. Rep., vol. 3, no. 1, p. 1637, 2013.

[151] S. Castelletto et al., “A silicon carbide room-temperature single-photon source,” Nat. Mater., vol. 13, no. 2, pp. 151–156, 2014.

[152] H. Wang, Y. Bi, N. Zhou, and H. Zhang, “Preparation and strength of SiC refractories with in situ β-SiC whiskers as bonding phase,” Ceram. Int., vol. 42, no. 1, Part A, pp. 727–733, Jan. 2016, doi: 10.1016/j.ceramint.2015.08.172.

[153] S. E. Saddow, “Silicon Carbide Materials for Biomedical Applications,” in Silicon Carbide Biotechnology, Elsevier, 2016, pp. 1–25. doi: 10.1016/B978-0-12-802993-0.00001-0.

[154] A. E. Arvanitopoulos et al., “On the Suitability of 3C-Silicon Carbide as an Alternative to 4H-Silicon Carbide for Power Diodes,” IEEE Trans. Ind. Appl., vol. 55, no. 4, pp. 4080–4090, Jul. 2019, doi:

10.1109/TIA.2019.2911872.

[155] J. Rao, G. Catherin, I. Murthy, D. Rao, and B. Raju, “Production of nano structured silicon carbide by high energy ball milling,” Int. J. Eng. Sci. Technol., vol. 3, no. 4, Aug. 2011, doi: 10.4314/ijest.v3i4.68544.

[156] T. Matsumoto, J. Takahashi, T. Tamaki, T. Futagi, H. Mimura, and Y. Kanemitsu, “Blue-green luminescence from porous silicon carbide,” Appl. Phys. Lett., vol. 64, no. 2, pp. 226–228, 1994.

[157] J. Lam, J. Lombard, C. Dujardin, G. Ledoux, S. Merabia, and D. Amans, “Dynamical study of bubble expansion following laser ablation in liquids,” Appl. Phys. Lett., vol. 108, no. 7, p. 074104, Feb. 2016, doi: 10.1063/1.4942389.

[158] S. Stauss, K. Urabe, H. Muneoka, and K. Terashima, “Pulsed Laser Ablation in High-Pressure Gases, Pressurized Liquids and Supercritical Fluids: Generation, Fundamental Characteristics and Applications,” in Applications of Laser Ablation - Thin Film Deposition, Nanomaterial Synthesis and Surface Modification, D. Yang, Ed., InTech, 2016. doi: 10.5772/65455.

[159] J. Cao et al., “3D printing and in situ transformation of SiCnw/SiC structures,” Addit. Manuf., vol. 58, p. 103053, Oct. 2022, doi: 10.1016/j.addma.2022.103053.

[160] M. A. Gondal, A. M. Ilyas, and U. Baig, “Facile synthesis of silicon carbide-titanium dioxide semiconducting nanocomposite using pulsed laser ablation technique and its performance in photovoltaic dye sensitized solar cell and photocatalytic water purification,” Appl. Surf. Sci., vol. 378, pp. 8–14, Aug. 2016, doi: 10.1016/j.apsusc.2016.03.135.

[161] T. G. F. Souza, V. S. T. Ciminelli, and N. D. S. Mohallem, “A comparison of TEM and DLS methods to characterize size distribution of ceramic nanoparticles,” J. Phys. Conf. Ser., vol. 733, no. 1, p. 012039, Jul. 2016, doi: 10.1088/1742-6596/733/1/012039.

[162] M. Saito, K. Yasukawa, T. Umeda, and Y. Aoi, “Copper nanoparticles fabricated by laser ablation in polysiloxane,” Sel. Pap. 1st Int. Conf. Phys. Opt. Mater. Devices, vol. 30, no. 7, pp. 1201–1204, Mar. 2008, doi: 10.1016/j.optmat.2007.05.049.

[163] P. V. Kazakevich, A. V. Simakin, and G. A. Shafeev, “Formation of periodic structures by laser

ablation of metals in liquids," Proc. Eur. Mater. Res. Soc. 2005 - Symp.-J Adv. Laser Lamp Process. Funct. Mater., vol. 252, no. 13, pp. 4457–4461, Apr. 2006, doi: 10.1016/j.apsusc.2005.07.165.

[164] R. Mahfouz, F. J. Cadete Santos Aires, A. Brenier, B. Jacquier, and J. C. Bertolini, "Synthesis and physico-chemical characteristics of nanosized particles produced by laser ablation of a nickel target in water," Appl. Surf. Sci., vol. 254, no. 16, pp. 5181–5190, Jun. 2008, doi: 10.1016/j.apsusc.2008.02.022.

[165] I. Horn, M. Guillong, and D. Günther, "Wavelength dependant ablation rates for metals and silicate glasses using homogenized laser beam profiles — implications for LA-ICP-MS," Appl. Surf. Sci., vol. 182, no. 1, pp. 91–102, Oct. 2001, doi: 10.1016/S0169-4332(01)00465-2.

[166] B. Campanella, S. Legnaioli, S. Pagnotta, F. Poggialini, and V. Palleschi, "Shock Waves in Laser-Induced Plasmas," Atoms, vol. 7, no. 2, 2019, doi: 10.3390/atoms7020057.

[167] J. Yuan, L. Liang, G. Lin, X. Li, and M. Jiang, "Experimental study on the laser-matter-plume interaction and its effects on ablation characteristics during nanosecond pulsed laser scanning ablation process," Opt. Express, vol. 27, no. 16, pp. 23204–23216, Aug. 2019, doi: 10.1364/OE.27.023204.

[168] A. Subhan, A.-H. I. Mourad, and Y. Al-Douri, "Influence of Laser Process Parameters, Liquid Medium, and External Field on the Synthesis of Colloidal Metal Nanoparticles Using Pulsed Laser Ablation in Liquid: A Review," Nanomaterials, vol. 12, no. 13, p. 2144, Jun. 2022, doi: 10.3390/nano12132144.

[169] J. Kim, D. Amaranatha Reddy, R. Ma, and T. K. Kim, "The influence of laser wavelength and fluence on palladium nanoparticles produced by pulsed laser ablation in deionized water," Solid State Sci., vol. 37, pp. 96–102, Nov. 2014, doi: 10.1016/j.solidstatesciences.2014.09.005.

[170] J. Theerthagiri et al., "Fundamentals and comprehensive insights on pulsed laser synthesis of advanced materials for diverse photo- and electrocatalytic applications," Light Sci. Appl., vol. 11, no. 1, p. 250, Aug. 2022, doi: 10.1038/s41377-022-00904-7.

[171] B. J. Abdullah, "Size effect of band gap in semiconductor nanocrystals and nanostructures from density functional theory within HSE06," Mater. Sci. Semicond. Process., vol. 137, p. 106214, Jan. 2022, doi: 10.1016/j.mssp.2021.106214.

[172] H. Gu et al., “Epoxy resin nanosuspensions and reinforced nanocomposites from polyaniline stabilized multi-walled carbon nanotubes,” J Mater Chem C, vol. 1, no. 4, pp. 729–743, 2013, doi: 10.1039/C2TC00379A.

[173] A. Alofi and G. P. Srivastava, “Thermal conductivity of graphene and graphite,” Phys. Rev. B, vol. 87, no. 11, p. 115421, Mar. 2013, doi: 10.1103/PhysRevB.87.115421.

[174] H. Eshgarf, R. Kalbasi, A. Maleki, M. S. Shadloo, and A. Karimipour, “A review on the properties, preparation, models and stability of hybrid nanofluids to optimize energy consumption,” J. Therm. Anal. Calorim., vol. 144, no. 5, pp. 1959–1983, Jun. 2021, doi: 10.1007/s10973-020-09998-w.

[175] M.-H. Zhou, G.-Z. Yin, and S. González Prolongo, “Review of thermal conductivity in epoxy thermosets and composites: Mechanisms, parameters, and filler influences,” Adv. Ind. Eng. Polym. Res., vol. 7, no. 3, pp. 295–308, Jul. 2024, doi: 10.1016/j.aiepr.2023.08.003.

[176] X. Chen et al., “Heat transfer in cutting and grinding processes: mechanisms, models, and applications,” Front. Mech. Eng., vol. 20, no. 3, p. 22, Jun. 2025, doi: 10.1007/s11465-025-0838-2.

[177] G.-W. Lee, M. Park, J. Kim, J. I. Lee, and H. G. Yoon, “Enhanced thermal conductivity of polymer composites filled with hybrid filler,” Compos. Part Appl. Sci. Manuf., vol. 37, no. 5, pp. 727–734, May 2006, doi: 10.1016/j.compositesa.2005.07.006.

[178] N. Mumtaz et al., “Fillers and methods to improve the effective (out-plane) thermal conductivity of polymeric thermal interface materials – A review,” Heliyon, vol. 10, no. 3, p. e25381, Feb. 2024, doi: 10.1016/j.heliyon.2024.e25381.

[179] S. J. Jeong and H. S. Lim, “Advanced strategies for thermal conductivity enhancement in polymer composites for application as thermal management materials,” Macromol. Res., vol. 33, no. 5, pp. 553–568, May 2025, doi: 10.1007/s13233-025-00377-8.

[180] K. S. Suhas, V. K. Reddy, Y. T. Reddy, and Y. Pai, “Effects of silicon carbide nanoparticles on mechanical and vibrational characteristics of carbon glass epoxy hybrid composites,” Sci. Rep., vol. 16, no. 1, p. 8009, Feb. 2026, doi: 10.1038/s41598-026-39559-4.

[181] H. Liu et al., “Enhancing interfacial properties of epoxy coatings via hyperbranched modification

of SiC fillers: Experimental and simulation insights," Chem. Eng. J., vol. 511, p. 161841, May 2025, doi: 10.1016/j.cej.2025.161841.

[182] A. Behera, J. Dehury, and B. P. Rayaguru, "The Consequence of SiC Filler Content on the Mechanical, Thermal, and Structural Properties of a Jute/Kevlar Reinforced Epoxy Hybrid Composite," Silicon, vol. 15, no. 15, pp. 6509–6519, Oct. 2023, doi: 10.1007/s12633-023-02543-y.

[183] M. Naeimirad, A. Zadhoush, and R. E. Neisiany, "Fabrication and characterization of silicon carbide/epoxy nanocomposite using silicon carbide nanowhisker and nanoparticle reinforcements," J. Compos. Mater., vol. 50, no. 4, pp. 435–446, Feb. 2016, doi: 10.1177/0021998315576378.

[184] T. Ding, W. Ma, and Z. Zhao, "Review of Alumina-Based Filler/Epoxy Resin Composites for Thermally Conductive Materials," Polym. Eng. Sci., vol. 66, no. 2, pp. 648–661, Feb. 2026, doi: 10.1002/pen.70251.

[185] A. Agrawal and A. Satapathy, "Experimental Investigation of Micro-sized Aluminium Oxide Reinforced Epoxy Composites for Microelectronic Applications," Procedia Mater. Sci., vol. 5, pp. 517–526, 2014, doi: 10.1016/j.mspro.2014.07.295.

[186] S. K. Ola, I. Chopra, T. Ola, and V. Dhayal, "Enhancing corrosion resistance of Epoxy-Based composite coatings on mild steel using functionalized aluminium oxide (Al_2O_3) nanoparticles," Sci. Rep., vol. 16, no. 1, p. 5514, Feb. 2026, doi: 10.1038/s41598-026-35180-7.

[187] S. M. Shahabaz et al., "Effect of Al2O3 and SiC Nano-Fillers on the Mechanical Properties of Carbon Fiber-Reinforced Epoxy Hybrid Composites," J. Compos. Sci., vol. 7, no. 4, p. 133, Mar. 2023, doi: 10.3390/jcs7040133.

[188] B. S et al., "Development and characterization of an epoxy matrix composite reinforced with Al2O3 embedded banyan fibers for secondary structural applications," Results Eng., vol. 26, p. 105587, Jun. 2025, doi: 10.1016/j.rineng.2025.105587.

[189] A. Permal, M. Devarajan, H. L. Hung, T. Zahner, D. Lacey, and K. Ibrahim, "Improved thermal and mechanical properties of aluminium oxide filled epoxy composites by reinforcing milled carbon fiber by partial replacement method," J. Mater. Sci. Mater. Electron., vol. 28, no. 18, pp. 13487–13495, Sep.

2017, doi: 10.1007/s10854-017-7188-8.

[190] N. Jamaludin, P. Anithambigai, S. Shanmugan, and D. Mutharasu, “Performance and Thermal Analysis of Aluminium Oxide Filled Epoxy Composite as TIM for LEDs,” Mater. Sci. Res. India, vol. 11, no. 1, pp. 35–41, Aug. 2014, doi: 10.13005/msri/110105.

[191] A. J. O., T. S. I., H. S. B., A. I. O., B. S. A., and A. E., “The Development and Characterisation of Aluminium Dross-Epoxy Resin Composite Materials,” J. Mater. Sci. Res., vol. 3, no. 2, p. p23, Feb. 2014, doi: 10.5539/jmsr.v3n2p23.

[192] M. Liang and K. L. Wong, “Electrical Performance of Epoxy Resin Filled with Micro Particles and Nanoparticles,” Energy Procedia, vol. 110, pp. 162–167, Mar. 2017, doi: 10.1016/j.egypro.2017.03.122.

[193] R. Kitey and H. V. Tippur, “Role of particle size and filler–matrix adhesion on dynamic fracture of glass-filled epoxy. I. Macromeasurements,” Acta Mater., vol. 53, no. 4, pp. 1153–1165, Feb. 2005, doi: 10.1016/j.actamat.2004.11.012.

[194] X. S. Xing and R. K. Y. Li, “Wear behavior of epoxy matrix composites filled with uniform sized sub-micron spherical silica particles,” Wear, vol. 256, no. 1–2, pp. 21–26, Jan. 2004, doi: 10.1016/S0043-1648(03)00220-5.

[195] P. Dittanet and R. A. Pearson, “Effect of bimodal particle size distributions on the toughening mechanisms in silica nanoparticle filled epoxy resin,” Polymer, vol. 54, no. 7, pp. 1832–1845, Mar. 2013, doi: 10.1016/j.polymer.2012.12.059.

[196] H. A. Al-Turaif, “Effect of nano TiO2 particle size on mechanical properties of cured epoxy resin,” Prog. Org. Coat., vol. 69, no. 3, pp. 241–246, Nov. 2010, doi: 10.1016/j.porgcoat.2010.05.011.

[197] A. Bruinink, J. Wang, and P. Wick, “Effect of particle agglomeration in nanotoxicology,” Arch. Toxicol., vol. 89, no. 5, pp. 659–675, May 2015, doi: 10.1007/s00204-015-1460-6.

[198] E. T. Swartz and R. O. Pohl, “Thermal resistance at interfaces,” Appl. Phys. Lett., vol. 51, no. 26, pp. 2200–2202, Dec. 1987, doi: 10.1063/1.98939.

[199] K. Pietrak, T. S. Wiśniewski, and M. Kubiś, “Application of flash method in the measurements of

interfacial thermal resistance in layered and particulate composite materials," Thermochim. Acta, vol. 654, pp. 54–64, Aug. 2017, doi: 10.1016/j.tca.2017.05.007.

[200] C.-W. Nan, R. Birringer, D. R. Clarke, and H. Gleiter, "Effective thermal conductivity of particulate composites with interfacial thermal resistance," J. Appl. Phys., vol. 81, no. 10, pp. 6692–6699, May 1997, doi: 10.1063/1.365209.

[201] W. D. Kingery, "Heat-Conductivity Processes in Glass," J. Am. Ceram. Soc., vol. 44, no. 7, pp. 302–304, Jul. 1961, doi: 10.1111/j.1151-2916.1961.tb15913.x.

[202] H. Yoon, P. Matteini, and B. Hwang, "Review on three-dimensional ceramic filler networking composites for thermal conductive applications," J. Non-Cryst. Solids, vol. 576, p. 121272, Jan. 2022, doi: 10.1016/j.jnoncrysol.2021.121272.

[203] D.-M. Liu, W. H. Tuan, and C.-C. Chiu, "Thermal diffusivity, heat capacity and thermal conductivity in Al2O3□Ni composite," Mater. Sci. Eng. B, vol. 31, no. 3, pp. 287–291, May 1995, doi: 10.1016/0921-5107(94)01163-X.

[204] Y. Zhao, Z. Zhai, and D. Drummer, "Thermal Conductivity of Aluminosilicate- and Aluminum Oxide-Filled Thermosets for Injection Molding: Effect of Filler Content, Filler Size and Filler Geometry," Polymers, vol. 10, no. 4, p. 457, Apr. 2018, doi: 10.3390/polym10040457.

[205] R. Nayak, D. P. Tarkes, and A. Satapathy, "A computational and experimental investigation on thermal conductivity of particle reinforced epoxy composites," Comput. Mater. Sci., vol. 48, no. 3, pp. 576–581, May 2010, doi: 10.1016/j.commatsci.2010.02.025.